Universal behaviors of magnetic domain walls in thin ferromagnets

Rebeca Díaz Pardo

université PARIS-SACLAY

NNT : 2018SACLS396

Thèse de doctorat

UNIVERSITÉ PARIS SUD
Comprendre le monde, construire l'avenir

Universal behaviors of magnetic domain walls in thin ferromagnets

Thèse de doctorat de l'Université Paris-Saclay préparé à l'Université Paris-Sud

École doctorale n°572 École Doctorale Ondes et Matière (EDOM)
Spécialité de doctorat: Physique de la matière condensée

Thèse présentée et soutenue à Orsay, le 23 Octobre 2018, par

Rebeca Díaz Pardo

Composition du Jury :

Thibaut Devolder Directeur de recherche CNRS, Centre de Nanosciences et de Nanotechnologies, CNRS/ UMR9001	Président
Stefania Pizzini Directrice de recherche, CNRS, Institut NEEL CNRS/UGA UPR2940, Université Grenoble Alpes	Rapporteur
Francois Montaigne Professeur des universités, Institut Jean Lamour CNRS/UMR 7198, Université de Lorraine	Rapporteur
Sebastián Bustingorry Investigador Independiente CONICET, Grupo de Teoría de la Materia Condensada, Centro Atómico Bariloche, Comisión Nacional de Energía Atómica	Examinateur
Vincent Jeudy Professeur des universités, Laboratoire de Physique des Solides (UMR8502)	Directeur de thèse

Acknowledgments

"Vendrán las iguanas vivas a morder a los hombres
[y las mujeres] que no sueñan "

Federico García Lorca.- Ciudad sin sueño

DURING the last three years in which I carried on my PhD project, and even before, there is a group of people and institutions without whom this work would not have been possible. First of all I want to thank my supervisor Vincent Jeudy for giving me the opportunity of working with him even without knowing much about me. I am very grateful for all his guidance, council and patience, and his very pedagogical way of explaining more than once any issue that was difficult for me to understand.

I want to thank the members of my jury for taking their time to read my manuscript, their constructive comments and corrections, and their interesting questions that helped me rethink and understand better the context of my thesis.

I would like to thank Consejo Nacional de Ciencia y Tecnología for giving me the scholarship (no. 410724) that allowed me to carry on with a PhD and gave me the opportunity to work in another country and learn a different way of thinking and living.

I would like to thank all our collaborators whose contributions were fundamental for the development of the project and for my formation. I will start by thanking Williams Savero who helped me a lot to get familiarized with the topic, experimental set up and life in France. I also want to thank Nicolas Moisan without whom every step of the process would have been so much slower and for his patience every time we changed our mind. I want to thank also A. Lemaître for providing the samples used in the last part of the thesis

and R. Rodmaq for providing us with the Pt/Co/Pt sample.

I want to dedicate a special acknowledgment to our collaborators in Bariloche: Sebastián Bustingorry, Alejandro Kolton and Nirvana Caballero for helping us understand the complex theory behind the nice things we see in the lab. And to the experimental part of the team, Javier Curiale and Lucas Albornoz for sharing all they have learned in the lab in Bariloche and exchanging their knowledge with us. In general, thanks to the whole Paredom team for giving me a very warm welcome during my stay there last year. I had a wonderful time in Patagonia.

Equally, I want to thank all the people in IDMAG for receiving me and immediately make me feel as part of the team, for showing me a constructive, honest, ethical way to do and enjoy science and for forcing me to learn French so that I would not miss the conversations during coffee time. Thanks to André for always pushing us to learn new things, be curious and ask interesting, challenging questions, to Alexandra, Stanislas and João for always giving me their professional opinion, listen to my seminars and having fruitful discussions, Raphaël for helping us solve practical problems. And also, I want to give special thanks to Pierre, Eloi, Ryuhei, Sachin and Aleš for being wonderful colleagues and friends.

I would like to thank also all the friends that I have met in the last three years, who made so much easier the transition of moving from another continent. Specially, I will thank my flat mate Valerio for being la mia piccola famiglia in Massy and feeding me with delicious Italian food. Also, to all my Mexican friends in Paris that bring me a little piece of Mexico with their humor, affection and obsession with food. Likewise, I want to thank all the friends from C2N (magnetic and non magnetic backgrounds) for sharing their experiences and good, fun evenings.

Of course I want to thank my older friends from university and before who have been there for a long time now in my life, and have always been incredibly supportive. Even though we do not meet so often now we have managed to stay friends for quite a while. I want to thank specially to my boyfriend Diego who is a wonderful, loving and supportive companion and makes me want to be a better person every day. Thank you for sharing your life path with me.

Finally I would like to thank my parents who have always believed in me, who always pushed me to pursue my goals, who have given me their unconditional support through all my life and have been amazing guides through my path into this strange world.

Résumé

Cette thèse est une exploration du comportement universel de parois de domaines magnétiques dans des films ferromagnétiques minces à anisotropie perpendiculaire. Elle comporte un état de l'art sur la dynamique des parois puis une description des méthodes expérimentales utilisées pour observer et déplacer les parois. Les résultats expérimentaux sont présentés dans les trois chapitres suivants. Nous résumons ici les principales études présentées dans le manuscrit : transition de dépiégeage, effets de tailles finies sur le régime de déplacement activé thermiquement (reptation) et criticalité de la dynamique des parois sous courant électrique.

Transition de dépiégeage

Nous avons exploré les comportements universels de la transition dépiégeage. La vitesse des parois de domaine dans un film de Pt/Co/Pt a été mesurée sur presque deux ordres de grandeur en température et sur une gamme magnétique couvrant les régimes de reptation (creep), dépiégeage et flow. Nos résultats ont été comparés à des données trouvées de la littérature pour des films de Au/Co/Au et de CoFeB. Nous montrons tout d'abord que la dynamique des parois est compatible avec les variations en loi de puissance attendues pour la vitesse et la rugosité et en bon accord avec les prédictions pour les exposants universels ($\psi = 0.15$ et $\beta = 0.25$). Pour aller au-delà de l'analyse habituelle des exposants critiques, nous proposons un modèle auto-consistant qui décrit les régimes de reptation et de dépiégeage et qui permet de distinguer les comportements universels et non-universels. Grâce à ce modèle, nous avons pu extraire la fonction universelle du régime de dépiégeage reflétant les effets thermiques et les effets du champ magnétique sur la vitesse des parois. Nous avons également mis en évidence une corrélation forte entre les paramètres effectifs

(dépendant de la température et des matériaux) qui contrôlent la dynamique de reptation et de dépiégeage. Ainsi, nous avons montré que la dynamique de parois est essentiellement contrôlée par trois paramètres dépendants du matériau et de la température et des fonctions universelles. De manière plus générale, notre étude montre que le comportement universel de dynamique de parois couvre une grande gamme de champ magnétique appliqués, qui s'étend de la limite à force nulle jusqu'au-dessus du seuil de dépiégeage. Sur toute cette gamme de champ magnétique, la dynamique de paroi en présence d'un désordre figé peut être décrite par l'équation de Edwards Wilkinson qui suppose une compétition en le désordre, l'activation thermique et l'élasticité de paroi.

Effets de taille finie

Nous avons étudié les effets de taille finie sur le mouvement des parois dans des films magnétiques de (Ga, Mn)As et (Ga, Mn)(As,P) d'épaisseurs comprises entre 12 et 80nm. L'exposant de vitesse et l'exposant de rugosité ont été mesurés en fonction du champ magnétique appliqué, pour différentes températures. Les courbes obtenues systématiquement des discontinuités pour les mêmes valeurs de champ magnétiques seuil. Au-dessous du seuil, le mouvement est compatible avec les exposants $\mu = 1/4$ et $\zeta = 2/3$, prédits pour le mouvement d'une ligne élastique dans un milieu à deux dimensions. Au-dessus du seuil, les résultats sont compatibles avec les exposants $\mu = 1/2$ et $\zeta = 2/5$, correspondant au mouvement d'une surface dans un milieu tridimensionnel. Ces résultats sont compatibles avec la variation sous champ magnétique de la longueur de saut thermique optimale qui provoque l'avancée des parois. Au-dessous du champ magnétique seuil, la longueur de saut est supérieure à l'épaisseur. Les sauts de parois sont confinés par l'épaisseur des couches. Au-dessus du seuil, la longueur de saut devient inférieure à l'épaisseur et la paroi se comporte comme une surface se déplaçant dans un milieu à trois dimensions. Nous avons donc mis en évidence le mouvement de reptation en trois dimensions.

Criticalité de la dynamique des parois sous courant électrique

Dans ce chapitre, nous discutons de la criticalité du mouvement de paroi produit par courant électrique. Nous proposons une analyse comparée de la dynamique de paroi dans des films de (Ga, Mn) (As, P) sous champ magnétique et sous courant. Nous montrons que la différence essentielle entre les deux types de forces est la directionnalité de la force associée au courant. Un champ magnétique agit de manière isotrope comme une pression. Au contraire, nous montrons que la force associée au courant est proportionnelle au produit scalaire entre la densité de courant et le vecteur normal à la paroi de domaine. Cette directionnalité est l'origine de la formation de facettes. Pour un angle d'inclinaison différent

de zéro, nous montrons que l'équation de mouvement peut être écrite par le modèle minimal de Kardar-Parisi-Zhang. Pour un angle d'inclinaison égal à zéro, les exposants critiques sont compatibles à ceux qui sont obtenus pour un déplacement sous champ magnétique. Ceci indique que la dynamique de parois sous courant en présence d'ancrage faible suit le modèle minimal d'Edwards-Wilkinson.

Abstract

Understanding magnetic domain walls dynamics (DW) is crucial in order to develop technological applications like high density memories in ferromagnets. From the fundamental point of view, domain walls are described as interfaces moving in a pinning potential and exhibit universal behaviors shared by different physical systems as diverse as propagation of fractures in solids, combustion fronts, ferroelectric domain walls, to name a few.

In the first part of the thesis we address the universal behavior of the depinning transition in domain walls driven by field. For this purpose we measure the DW velocity driven by field in an ultrathin Pt/Co/Pt film and then compare our results with other published in the literature. We reveal a universal scaling function, and obtain a consistent description for both the depinning transition and the thermally activated creep regime.

In a second part of the manuscript, we study the finite size effects on DW dynamics in the thermally activated creep regime. We use ferromagnetic (Ga, Mn)(As,P) films with different thicknesses. We find a discontinuity in the roughness exponent (ζ) and the slope in the field driven DW velocity within the creep regime. This evidences a dimensional crossover and a change in criticality in the quenched Edward-Wilkinson model: from the motion of an elastic line ($d = 1$) moving in a $2D$ medium to the motion of an elastic interface ($d = 2$) moving in a $3D$ medium at low and high drive, respectively.

In the last part we compare the thermally activated creep dynamics on domain walls driven by magnetic field and electric current in a (Ga,Mn)(As,P) thin film. We measure the creep exponent μ and the roughness exponent ζ for field and current driven DW motion. We find that when the angle between the current and the normal to the DW is sufficiently small, the current induced DW motion belongs to the quenched Edward-Wilkinson universality class as field induced DW creep.

Contents

CHAPTER 1

Introduction

"Je me propose de montrer ici que l'on peut fonder une théorie du ferromagnétisme sur une hypothèse extrêmement simple concernant ces actions mutuelles. Je suppose que chaque molécule éprouve de la part de l'ensemble des molécules environnantes une action égale à celle d'un champ uniforme NI proportionnel à l'intensité d'aimantation et de même direction qu'elle. On pourrait donner à NI le nom de champ intérieur pour marquer l'analogie avec la pression intérieure de van der Waals."

Pierre Weiss. -L'hypothèse du champ moléculaire et la propriété ferromagnétique.

The idea of magnetic recording of information has emerged since the last decades of the 19th century. At the 1900 Paris exhibition Valdemar Poulsen showed a recording of the voice of Emperor Franz Joseph in a magnetic wire warped around a drum. Approximately 30 years latter, commercial applications were available. Ever since, magnetic recording has played a crucial role in information storage. There is hardly any aspect of our lives (from work to leisure) where magnetic recording devices are not present [21].

Nowadays, the engineering of magnetic materials and the manipulation of their properties caused a lot of scientific interest and new questions arise on the basic physics of magnetism. For a long time only magnetic field was used to manipulate the magnetization and magnetic domain structure in ferromagnetic materials. However in recent years the development of nanotechnologies has allowed the use of electrical current to manipulate the magnetization, through spin-transfer torque mechanisms [89, 106, 62]. Technological applications based on the manipulation of magnetic structures as magnetic domain walls or Skyrmions were proposed. My thesis falls within this context, and aims at a better understanding of the magnetic domain wall's dynamics.

On the other hand, magnetic domain walls are well known to be strongly sensitive to the pinning caused by local defects or inhomogeneities in the host materials. Even a weak pinning produces stochasticity and a roughening of domain walls (DWs). The understanding on how weak pinning affects DW dynamics is important for applications. This issue is also relevant on a wider context. Pinning dependent dynamics is observed in a vast variety of physical systems: magnetic domain walls [70, 73, 112], ferroelectric domain walls [107], wetting contact lines [78], fractures [87], vortex lattices [7] to name a few. Even though these systems have a priori, completely different physical properties at the microscopic scale, they present common universal behaviors, which are of interest for several areas of physics.

The interplay between the interface elasticity, weak pinning disorder, thermal activation, and a driving force leads to very rich physics. The variation of interface velocity with the magnitude of the driving force f is particularly interesting. At zero temperature, the DWs are pinned until the driving force f reaches the depinning threshold f_d. Just above the threshold, the interface is predicted to present a universal depinning transition with a velocity v varying as a power law with the force ($v \sim (f - f_d)^\beta$). At finite temperature, thermal activation favours the interface motion and a so-called creep motion is observed below the threshold. Close to zero drive ($f \to 0$), the velocity follows an Arrhenius law ($\ln v \sim -\Delta E/k_B T$), where $k_B T$ is the thermal activation energy. The effective pinning barrier height ΔE presents a power law variation with the drive ($\Delta E \sim f^{-\mu}$), where μ is universal exponent. At high drive the motion of interfaces is controlled by dissipation and is expected to vary linearly with the driving force.

For magnetic domain walls driven by magnetic field, the creep motion was first evidenced in Pt/Co/Pt ultrathin films with perpendicular anisotropy by Lemerle *et al.* [70]. In particular, the measured value of the critical exponent μ was found compatible with theoretical predictions $\mu = 1/4$ [14] for an elastic line with short range elasticity moving in a short range pinning disorder. Since this seminal experimental work, significant progress has been made for the understanding of pinning dependent phenomena. To name a few, the depinning transition was observed in ultrathin films [73], finite size effects producing a change of universal behavior was evidenced in nanowires [58], the contribution of long range interactions to universal behaviors [30, 8] were investigated.

However, as this subject has been explored, new questions have arisen. The critical behaviors of current induced domain wall motion are controversial, since different values

of critical exponents are reported in the literature [112, 67, 76, 31]. The contribution of DW chirality on the creep motion also remains an open question [66, 109, 65]. Universal behaviors of the depinning transition, and the links between the depinning and creep motion are not well understood [12].

This thesis explores the universal behaviors of DW dynamics. In particular, we propose an analysis of the depinning transition, the criticality of current driven DW motion, and the contribution of finite thickness effects of magnetic films on the DW criticality. For each study, we try to go beyond the usual power law analysis and access the universal function catching both the thermal and drive effects on the dynamics.

The manuscript is organized as follows: chapter 2 brings a general overview on magnetic domains, domain walls and their micromagnetic description. Next, we present the state of the art on magnetization dynamics, the dissipation and pinning dependent regimes of DW motion. Chapter 3 focuses on the experimental methods and details the measuring protocols used in this work. Our results are presented in chapters 4 to 6. The universal behaviors of the depinning are discussed in chapter 4. In chapter 5 we report experimental evidences of the dimensional crossover of universal behavior due to the finite thickness of ferromagnetic films. In chapter 6, we compare the criticality of current and magnetic field induced DW creep motion. Finally chapter 7 contains the global conclusions and perspectives.

CHAPTER 2

Magnetic domains and domain wall dynamics

"La hipótesis de los dominios de Weiss ha recibido una confirmación evidente mediante una serie de experimentos inaugurados por Bitter y particularmente trabajado por Backer y Elmore... Microfotografías de estos depósitos muestran la existencia de líneas bien definidas sobre la superficie, dibujadas por la acumulación de las partículas en lugares definidos por la intersección de las superficies límites de los dominios. Tales dibujos se producen sólo en los cuerpos ferromagnéticos."

Blas Cabrera.- El magnetismo de la materia

In this chapter we present a state of the art on magnetic field and electric current induced domain wall (DW) motion. We start by giving a general overview on ferromagnetism in Pt/Co/Pt and (Ga,Mn)As, magnetic energies, magnetic domains and domain walls. Then we describe dynamical regimes for field and current induced DW motion without pinning. Finally we illustrate with more detail the dynamical regimes for a DW seen as an elastic interface moving in a weak random pinning potential and summarize a selection of reported experimental results that are relevant for our investigations.

2.1 General concepts on magnetic thin films

In this section we describe briefly the origin of ferromagnetism in the two materials we will discuss throwout this thesis: (Ga,Mn)As and Pt/Co/Pt. Pt/Co/Pt is studied in Chapter 4 where we analyze the depinning transition. The criticality and universal behaviors at the creep regime in this material are well studied and, therefore we will be able to explore universal behaviors at the depinning transition and compare them with the ones already known at the creep regime. We use several samples of (Ga,Mn)As in chapters 5 and 6. In spite of it's low Curie temperature, this material is convenient to study current induced domain wall dynamics since the efficiency of the spin transfer torque is relatively high and therefore we are able to observe the end of the creep regime.

We also present the micromagnetic description of ferromagnetism, which is used to describe magnetic domains and domain walls.

2.1.1 Origin of ferromagnetism

Ferromagnets are materials that exhibit spontaneous magnetization, meaning that have a net magnetic moment in the absence of an external magnetic field. Even in the demagnetized state, a ferromagnet is divided into a number of small regions called domains. Each of this regions is magnetized with a M_s saturation magnetization but cancel each other and therefore the total magnetization is zero. This spontaneous magnetization vanishes at what is known as the Curie temperature, T_C, above which a material is no longer ferromagnetic and becomes paramagnetic [18, 61].

The spin of electrons in atoms is the most basic origin of magnetism. The spins are confined to two states "up" or "down". When the spins are aligned, their tiny magnetic moments add to form a larger magnetic moment. Spins fill the energy levels in an atom following Hund rules [61, 5]. In atoms with filled electron shells the total magnetic moment is zero. So materials with unfilled atomic shells present magnetic response, i.e. they align with external magnetic fields. But this is not enough to explain spontaneous magnetization.

Ferrmomagnets remained puzzling materials until 1906 when Pierre Weiss proposed the existence of a molecular field. This field acts in a ferromagnetic substance below its Curie temperature and it is strong enough to magnetize the material even in the absence of an applied field. This means that the substance is spontaneously magnetized [111].

The physical origin of the molecular field is the exchange forces between atoms. This is a consequence of spins being fermions, and therefore, they obey Pauli's exclusion principle. Two electrons with the same spin cannot approach indefinitely. In consequence, their electric charge in space are farther apart when the spins are parallel than when they are antiparallel. This difference of energy is the origin of exchange energy for which Heisenberg proposed a Hamiltonian for localized spins [46] which will be described in more detail in the magnetic

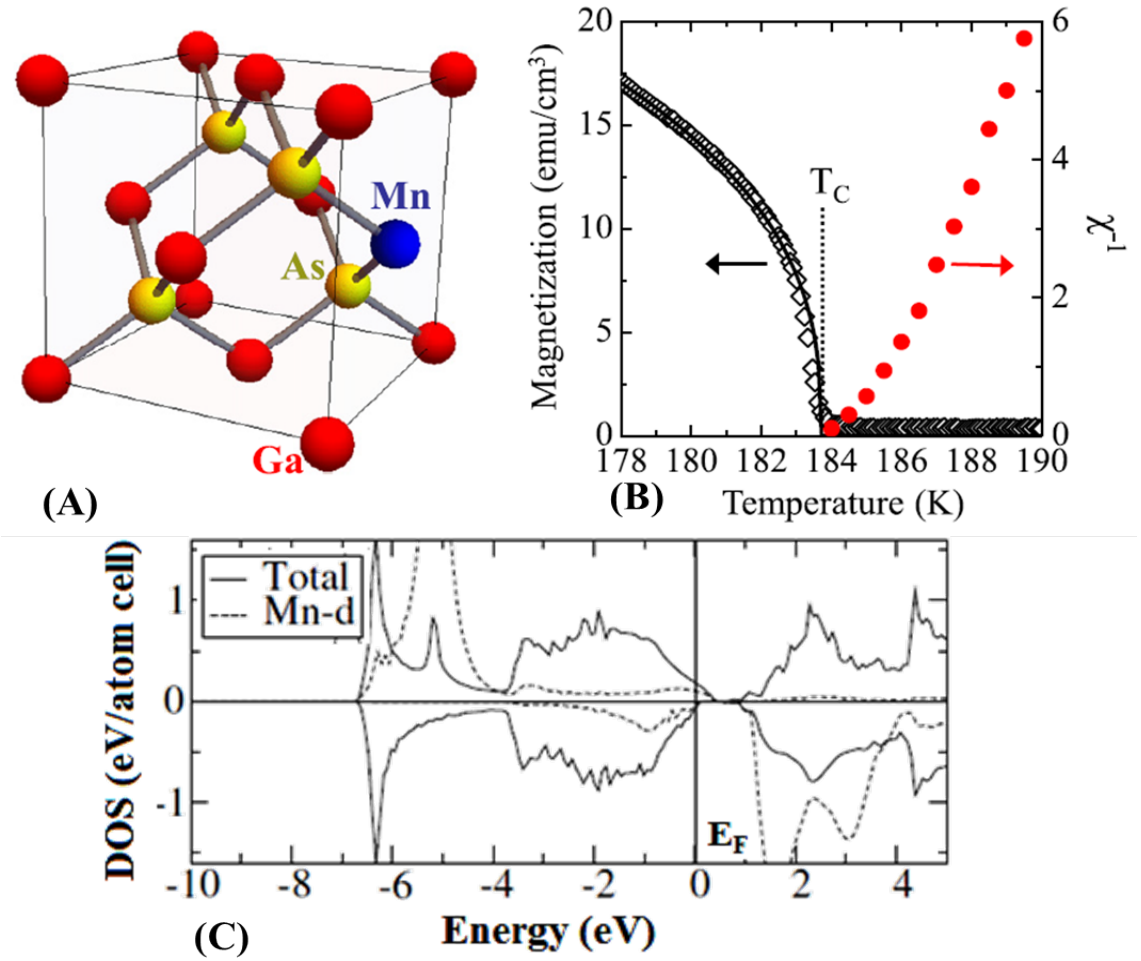

Figure 2.1: **GaMnAs structure and properties.** (A) Mn randomly occupy sites in the zincblende structure of the host semiconductor GaAs. (B) remanent magnetization and inverse magnetic susceptibility *vs* T for (Ga,Mn)As with a nominal Mn concentration of 12 %. (C) Calculated total Density of States (solid line) for (Ga,Mn)As with 5% of Mn and partial DOS for d-type electrons. We observe the spin unbalance in the Fermi energy giving as a result a ferromagnetic character in (Ga,Mn)As. Adapted from [32, 105]

energies section.

Metallic ferromagnets fulfill the Stoner criteria which establishes that the product of the potential energy U between the charges in two electrons in the same site, but with opposite spin, times the density of states at the Fermi energy, should be larger than 1 ($Ug(E_F) > 1$) [101]. For example, the ferromagnetism of Fe, Co, and Ni is due to spin unbalance in the $3d$ band.

There are however, ferromagnetic materials for which the magnetic properties cannot be explained in terms of direct exchange like in the transition metals referred above. In this thesis, one of the materials we use is the magnetic semiconductor $(Ga_{1-x}Mn_x)$As in which

ferromagnetism is related to a long distance exchange.

In this material Mn atoms substitute Ga atoms in a GaAs zincblende structure lattice as illustrated in Fig. 2.1 (A). In this case Mn atoms have an electronic configuration $d^5 + h$ where d are strongly localized and the acceptor nature of the substitutional Mn ensures there are charge carriers and therefore charge mobility [32]. (Ga,Mn)As is one of the most studied ferromagnetic semiconductors due to its relatively high Curie Temperature that has been reported to be as high as $180K$ [32, 110] as it is shown in Fig. 2.1 (B).

The presence of defects in this system, like interstitial Mn, is determinant for the magnetic properties. Since the concentration x of Mn is normally bellow $\approx 10\%$ [24, 23], the distance between Mn atoms is relatively large for there to be direct interaction between them. There are intermediaries between this $3d^5$ localized moments. This intermediaries are both the conduction electrons e^- and the holes h, in the valence band [3, 49]. However this mechanism is dominated by the interaction between the localized $S = 5/2$ Mn spins and the holes h since its exchange integral is almost one order of magnitude larger than the exchange integral of localized Mn spins and conduction electrons [83].

Dietl, *et al.* showed that the exchange mechanism between delocalized charge carriers and localized $3d$ electrons was similar to the exchange proposed by Zener for antiferromagnets [114]. Since the distance between carriers r_h is larger than the distance between localized spins r_m, the interaction between them was equivalent to the long distance Ruderman-Kittel-Kasuya-Yosida (RKKY) coupling mechanism [24, 15, 105].

In a general way, in RKKY coupling, localized nuclear magnetic moments or localized inner $d-$ or $f-$ shell electron spins in a metal, interact with the conduction electrons through hyperfine interactions [108, 113]. The sign of the interaction between localized spins may oscillate with distance [15, 105]. This gives as a result a spin unbalance in the Fermi energy as shown in Fig. 2.1 (C) which, originates the ferromagnetic behavior.

In the case of ultra thin Pt/Co/Pt films like the one we use in this thesis, the electrons in the d^5 configuration have a total angular momentum $L = 0$, so there cannot be spin-orbit coupling. The orbital moment enhancement, and strong $3d - 5d$ hybridization are highly localized at the interface, and this is the main cause of the perpendicular magnetic anisotropy. As the Co layer gets thinner, its orbital moment m_{orb} increases, and magnetic moments are induced on Pt atoms by the strong Pt $5d$-Co $3d$ hybridization across the interface.

2.1.2 Magnetic energies

The structure of magnetic domain walls and magnetic domains is controlled by different energy terms that are described in this section.

Zeeman energy

When a magnetic field $\vec{H}_{app}$ is applied in a magnetic substance, the magnetization $\vec{M}$ is submitted to a torque. The Zeeman energy expresses this interaction and is written as [2]:

$$E_Z = -\mu_0 \int_V \vec{M} \cdot \vec{H}_{app} dV \tag{2.1}$$

where, $\mu_0 = 4\pi \times 10^{-7} H/m$ [42] is the permeability of free space.

Exchange energy

The exchange energy describes the interaction between the magnetic moments. W. Heisenberg showed that for two atoms i and j with spins angular momentum $\hbar\vec{S}_i$ and $\hbar\vec{S}_j$ the exchange energy between them is:

$$\mathcal{H}_{Heisenberg} = -\sum_{i \neq j} 2J_{ij} \vec{S}_i \cdot \vec{S}_j, \tag{2.2}$$

where J_{ij} is the exchange integral which has energy units. $J > 0$ indicates a ferromagnetic interaction leading to the parallel spin alignment and $J < 0$ indicates an antiferromagnetic interaction preferring the anti parallel spin alignment.

The micromagnetic version of the exchange energy is commonly written as:

$$E_{ex} = \int_V A[(\nabla m_x)^2 + (\nabla m_y)^2 + (\nabla m_z)^2] dV, \tag{2.3}$$

where A is the exchange stiffness coefficient, and m_x, m_y, m_z, the components of reduced magnetization. This energy term tends to reduce the magnetization gradient.

Magnetic dipolar energy

The magnetization of a sample creates a magnetic field $\vec{H}_d$. Directly from Maxwell's equations, we find the divergence of this stray field as the divergence of magnetization of the material: $\nabla \vec{H}_d = -\nabla \vec{M}$. The magnetic dipolar energy describing the interaction between the stray field and the magnetization can be written as [2, 72]:

$$E_d = -\frac{\mu_0}{2} \int_V \vec{H}_d \cdot \vec{M} dV. \tag{2.4}$$

The calculation of the stray field can pose certain difficulties in practice depending on the shape and the magnetization distribution. The stray field in a uniformly magnetized ellipsoid for example is $\vec{H}_d = -N \cdot \vec{M}$ where N is the symmetrical demagnetizing tensor.

In order to minimize the demagnetization energy, ferromagnetic materials break the uniform magnetization into domains with different magnetization directions.

Anisotropy energy

Another energy term that has an important role in ferromagnetism is the anisotropy energy, which reflects the energy variation on the relative alignment of magnetization with respect to the sample structural axes. The anisotropy may have different origins such as the crystal structure, the geometry of a specific sample, the presence of an interface...

The simplest example is the case of uniaxial anisotropy, which can be described by [2, 34]:

$$E_K = \int_V K_u \sin^2 \theta dV, \tag{2.5}$$

where θ is the angle between magnetization $\vec{M}$ and the easy axis, and K_u is the first order anisotropy constant.

For the Pt/Co/Pt thin films used in this thesis, the uniaxial anisotropy can be written as $K_u = K_v + 2K_s/t$, where t is the thickness of the ferromagnetic layer, K_v is the volume anisotropy and K_s is the surface anisotropy. For the ferromagnetic semiconductor (Ga,Mn)As, the anisotropy is controlled by the band structure and the strains. Thin films grown along the [001] axis on a GaAs crystal usually present in-plane anisotropy. In contrast, perpendicular anisotropy is obtained by inserting phosphorous in the crystal structure [68]. Other ferromagnetic semiconductors also present a small in-plane anisotropy. However, the uniaxial anisotropy is usually sufficient to describe the domain wall structure and their dynamics.

The ferromagnetic semiconductor films used in this thesis are bilayers of (Ga,Mn)As/(Ga,Mn)(As,P). They present perpendicular anisotropy, which results from competition between the in-plane and out-of-plane anisotropies. A more detailed description of anisotropy can be find in the references Dietl *et al.* [24, 82].

2.1.3 Magnetic domains and domain walls

The main issue of micromagnetism is to minimize the total energy ($E = E_Z + E_{ex} + E_d + E_K$) in order to determine structure of domains and domain walls.

We can define a domain wall (DW) as an interface between two regions where spontaneous magnetization has different directions. Inside the DW, spins rotate progressively from the first to second direction of magnetization. The magnetic structure of a DW results from the competition between anisotropy E_K and exchange energy E_{ex}. The exchange energy is minimized when adjacent spins are parallel, so this term will try to make the domain wall as wide as possible. On the other hand the anisotropy energy is minimized when spins are aligned along the easy anisotropy axis. So the anisotropy term will try to make the DW as narrow as possible. As a result of this competition, the wall finds a finite equilibrium width, and a well defined structure. The simplest description of the DW energy per unit volume can be written as [72]:

$$w_{DW} = w_{ex} + w_K = A\left[\left(\frac{\partial\theta}{\partial y}\right)^2 + \left(\sin\theta\frac{\partial\phi}{\partial y}\right)^2\right] - K_u\sin^2\theta, \tag{2.6}$$

where θ and ϕ are the magnetization's polar and azimuthal angles of (see figure 2.3). A is the exchange stiffness, K_u is the anisotropy constant in uniaxial anisotropy. The equilibrium structure of the domain wall can be deduced from a variational minimization of the energy, which leads to:

$$\theta(y) = \pm 2\arctan(\exp[y/\Delta]), \quad \text{and} \quad \phi = cte \tag{2.7}$$

Here, $\Delta = \sqrt{A/K_u}$ is the DW thickness parameter. The corresponding DW energy per unit surface is $\sigma = 4\sqrt{AK_u}$.

The DWs can be classified into two groups depending on the way the magnetization turns from one domain to another (as shown in figure 2.2). For $\phi = 0$ or $-\pi$, the DW has the so-called Bloch structure. The magnetization rotates in the plane of the domain wall as it is shown in figure 2.2 (A). For $\phi = \pm\pi/2$, the magnetization rotates in the plane of the sample and outside the plane of the DW. This type of DW is known as a Néel wall and it is illustrated in figure 2.2 (B).

Note that there are also topologically non trivial domain wall structures such as vortex domain walls and skyrmions, which are not discussed here [38, 97, 48].

2.2 Domain wall dynamics

So far we have presented the origin and structure of magnetic domain walls when they are static, but we have not discussed their dynamics. In the following section we present a state of the art on magnetic DWs motion driven by magnetic field and electric current. DWs follow different dynamical regimes depending on the strength of driving force. For low drives, below the depinning threshold (a depinning field H_d or a depinning current J_d) the motion is thermally activated and controlled by pinning. Well above the depinning

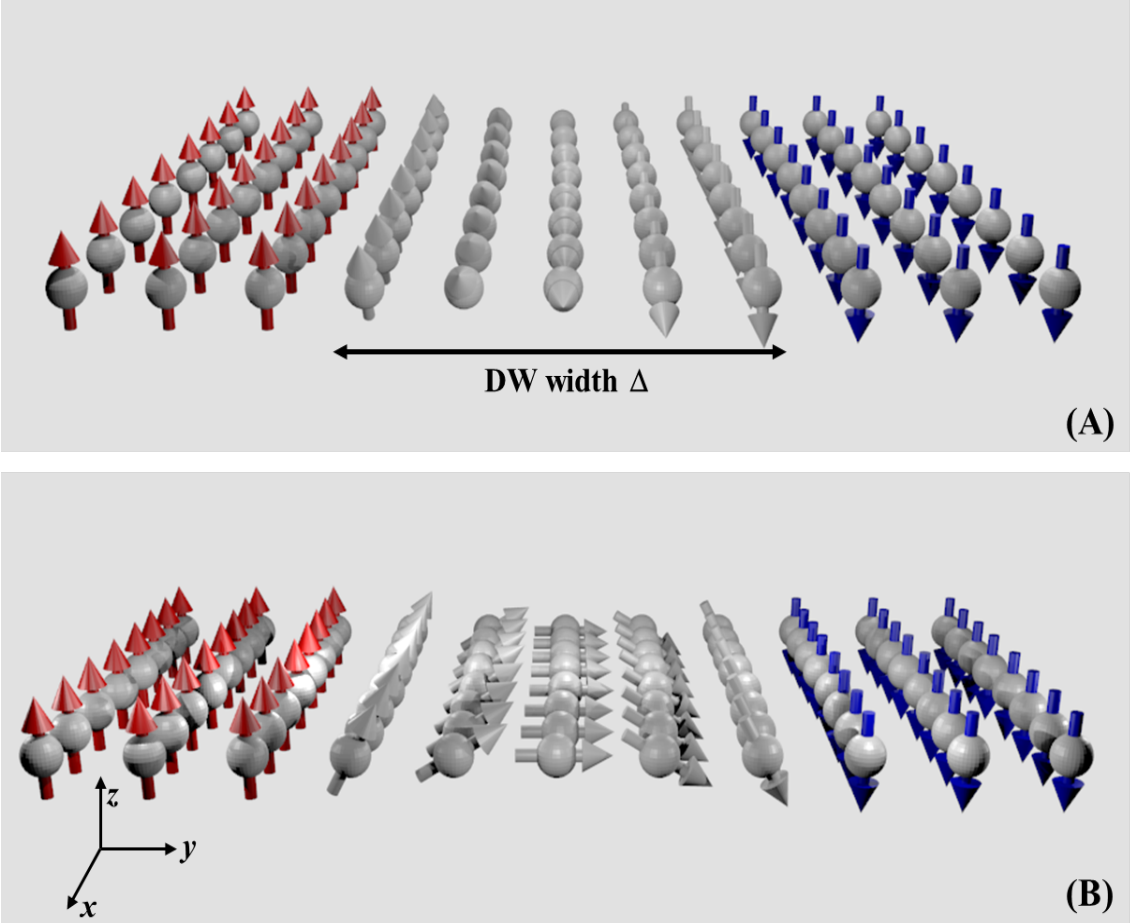

Figure 2.2: **Types of magnetic domain walls.** Schematic representation of Bloch (A) and Néel (B) magnetic domain walls.

threshold DW dynamics is limited by dissipation. We will briefly describe the dynamical flow regimes and then consider the thermally activated regime controlled by pinning, as well as the depinning transition.

2.2.1 Flow dynamic regimes

In the absence of pinning, the motion of magnetic moments inside the DW is caused by the torques exerted by the applied magnetic field. The description of magnetization dynamics is based on the Landau-Lifschitz-Gilbert equation, which establishes that the magnetization time rate is equal to the sum of torques exerted on the magnetization $\vec{M}$ [72].

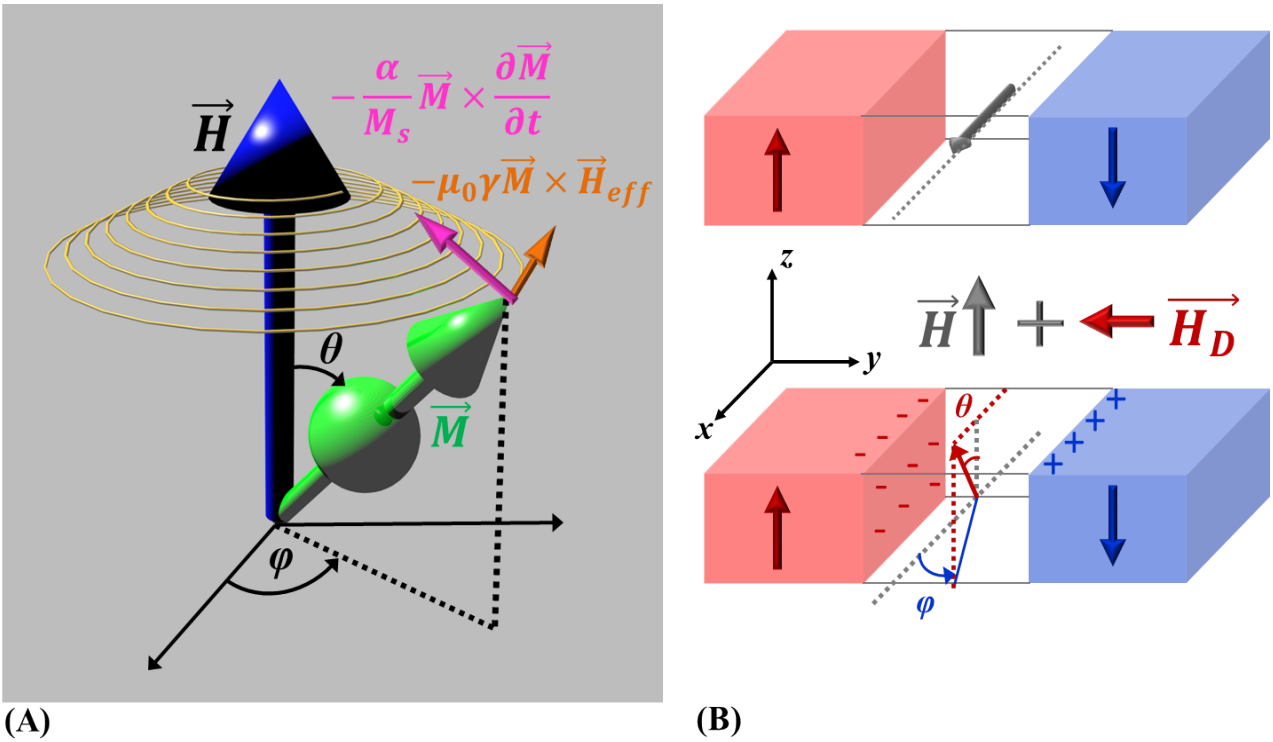

Figure 2.3: **Dynamics of the magnetization $\vec{M}$ when a magnetic field $\vec{H}$ is applied.** (A) $\vec{M}$ precesses around $\vec{H}$ while dissipating energy until both vectors are parallel. The orange arrow indicates the precession of $\vec{M}$ around $\vec{H}$ and the pink arrow indicates the damping term. (B-top) Bloch DW at rest with no external field (B-bottom) After the magnetic field $\vec{H}$ is applied parallel to the easy axis of magnetization (z axis) induces a rotation in the xy plane of $\vec{M}$ which produces a demagnetizing field $\vec{H}_D$. Finally $\vec{H}_D$ induces a rotation of $\vec{M}$ in the xz plane and the motion of the DW.

Field induced flow regime

The Landau-Lifsthitz-Gilbert (LLG) equation can be written [72, 64, 41]:

$$\frac{\partial\vec{M}}{\partial t} = -\mu_0\gamma\vec{M}\times\vec{H}_{eff} + \frac{\alpha}{M_s}\vec{M}\times\frac{\partial\vec{M}}{\partial t}, \tag{2.8}$$

where γ is the gyromagnetic ratio ($\gamma = 1.76\times10^{11}Hz/T$). The parameter α is known as the Gilbert's damping parameter, $\vec{M}$ is the local magnetization, $M_s = |\vec{M}|$ the saturation magnetization, and $\vec{H}_{eff}$ the effective magnetic field. The first term on the right side corresponds to the precession of magnetization $\vec{M}$ around $\vec{H}_{eff}$ (see figure 2.3), and the second term corresponds to the dissipation. The effective field, defined by functional differentiation of the total energy can be written as:

$$\vec{H}_{eff} = -\frac{1}{\mu_0}\frac{\delta w(\vec{M}(\vec{r}))}{\delta \vec{M}} \tag{2.9}$$

where w is the total free energy per unit volume.

In 1974, Walker and Schryer [98] developed a model to describe the motion of domain walls under applied magnetic field. The model considers an infinite medium with uniaxial anisotropy. The magnetization $\vec{M}$ is assumed to depend only on the position y and to remain constant along the x direction, as it is shown in Fig. 2.3 (B). It also assumes that the static structure of DWs (see Eq. 2.7) is conserved during the motion. They rewrote the LLG equations and deduce the time variation of the velocity and angle ϕ (further reference in [72]).

The mechanism by which an applied magnetic field produces the motion can be explained qualitatively. Let us consider a Bloch wall as it is shown in figure 2.3 (B). The rotation of the magnetization vector under a field along the z axis takes place in a "two step" process: the field induces magnetization rotation in the xy plane generating an unbalance of magnetic charges which produces a demagnetizing field $\vec{H}_D$ along the y axis. Then the demagnetizing field $\vec{H}_D$ produces a rotation of magnetization in the xz plane and therefore DW motion.

When the external field increases two different regimes are predicted as shown in figure 2.4: the steady and precessional regime. If the field is smaller than the so-called Walker field ($H < H_W$), the domain wall moves in the steady state regime where the azimuthal angle ϕ is constant, i.e., $\dot{\phi} = 0$. In this regime the average velocity is given by:

$$\bar{v} = \frac{\gamma \Delta H}{\alpha}. \tag{2.10}$$

The Walker limit corresponds to the maximum value of the torque exerted by the demagnetizing field. The Walker field and the associated velocity are given by:

$$H_W = \frac{\alpha M_s}{2} \quad \text{and} \quad v_W = \frac{\gamma \Delta}{2}\mu_0 M_s \tag{2.11}$$

For a thin film we also need to take into account the demagnetizing factors N_x, N_y and N_z along the axis x, y and z respectively. For a thin film with perpendicular anisotropy, we consider the z axis perpendicular to the thin film's plane. In this case the Walker field is approximately expressed as:

$$H_W^{films} = (\alpha/2) M_s |N_y - N_x|. \tag{2.12}$$

For $H > H_W$, the torque exerted by the demagnetizing field H_d cannot compensate the drag term γH, and ϕ continues to precess, and thus no dynamical equilibrium is reached.

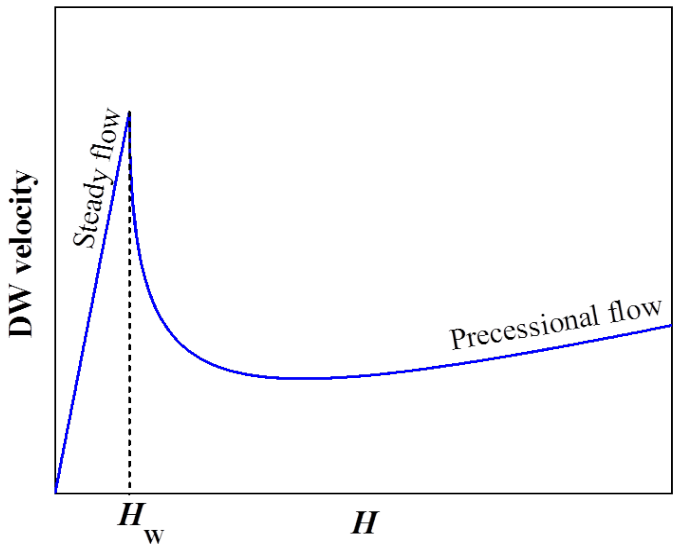

Figure 2.4: **Predicted DW velocity as a function of field for the flow regimes.** For $H < H_W$ the DW moves in a steady regime until a maximum velocity is reached at the Walker field H_W. For $H \gg H_d$ the velocity decreases until the asymptotic precessional flow regime is reached and the velocity recovers a linear behavior. The plot corresponds to Eqs. 2.11 - 2.14.

The DW does not move at constant velocity anymore and there is a periodic oscillation of the azimuthal angle ϕ from 0 to $\pi/2$. This implies that the domain wall oscillates between Néel and Bloch wall configurations. During this precession regime the average velocity is given by:

$$\bar{v} = \frac{\gamma \mu_0 \Delta}{\alpha} \left(H - \frac{\sqrt{H^2 - H_W^2}}{1 + \alpha^2} \right). \tag{2.13}$$

In the limit of large drive ($H \gg H_W$), ϕ precesses as γH, and the periodic torque terms average out. In this regime, the only torque contributing to the net velocity is the damping torque term. The average velocity is expressed as:

$$\bar{v} \approx \gamma \frac{\alpha \Delta}{1 + \alpha^2} \mu_0 H. \tag{2.14}$$

Therefore, the model developed by Walker and Schryer [98] predicts (see figure 2.4 and Eq. 2.13), two linear variations of the velocity separated by an intermediate regime with a negative mobility.

Experimentally, the flow regimes and in particular the steady flow is observed for samples that present sufficiently weak pinning strengths.

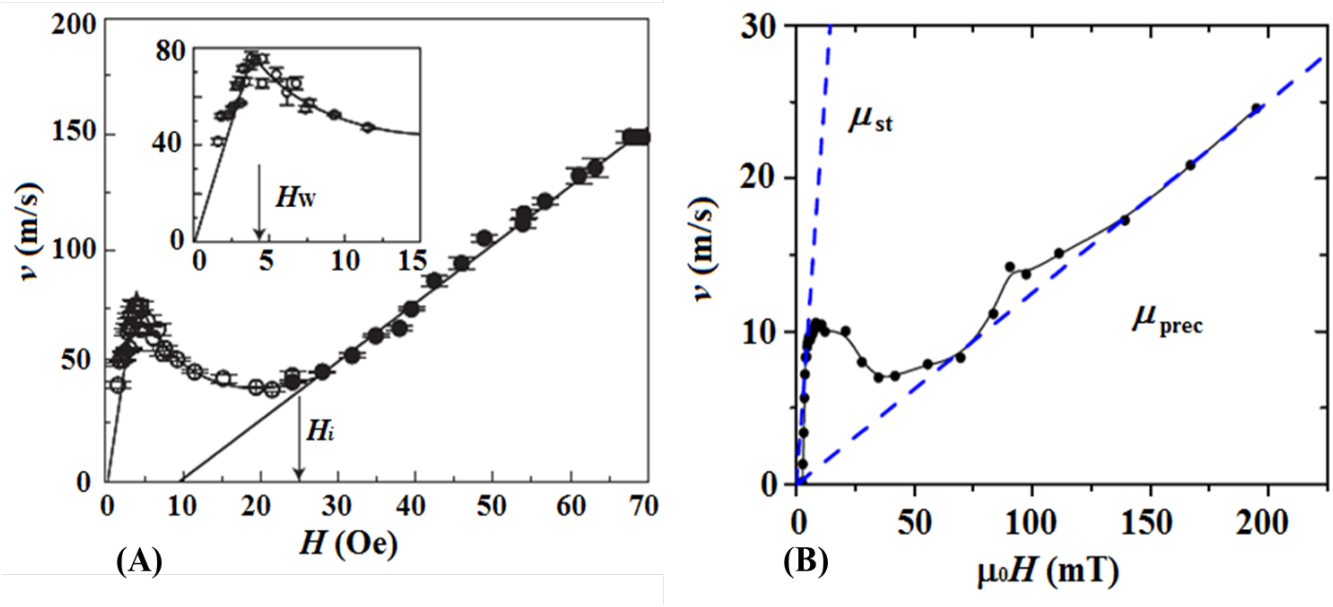

Figure 2.5: **Experimental observations of the flow regimes driven by magnetic field.** (A) Domain wall velocity v *vs* magnetic field H for 600 nm wide Permalloy tracks [6]. (B) DW velocity for a (Ga,Mn)As film at $T = 80K$. The dashed blue lines represent the linear velocity in the steady and precessional regimes with mobility $\mu_{st} = \gamma\Delta/\alpha$ and $\mu_{prec} = \gamma\Delta\alpha/(1+\alpha^2)$, respectively [26].

Beach *et al.* [6] observed the predicted steady and precessional regimes in permalloy (Py) nanowires with in-plane anisotropy (See figure 2.5 (A)). They show that the DW velocity v *vs* field H presents two dynamical regimes separated by a peak followed by a region of negative differential mobility and highly irregular wall motion. At lower fields they identify the steady regime where the velocity is proportional to the field. At higher fields they observe the linear precessional flow regime, shown in figure 2.5 (A).

Also Dourlat *et al.* [27] observed the steady and precessional flow regimes in (Ga,Mn)As films (see figure 2.5 (B)). This paper is the first report on the observation of the Walker breakdown in films with perpendicular anisotropy. The pinning dependent dynamics will be described in detail in the next sections.

Current induced flow regime

In this subsection we provide a brief description of the adiabatic and non-adiabatic terms of the spin transfer torque (STT) and their effects on magnetic domain wall displacement.

The effect of an electrical current on the magnetization is commonly described by the modified LLG equation [103]:

$$\frac{\partial \vec{m}}{\partial t} = -|\gamma|\mu_0 \vec{m} \times \vec{H_{eff}} + \alpha \vec{m} \times \frac{\partial \vec{m}}{\partial t} - (\vec{u} \cdot \vec{\nabla})\vec{m} + \beta \vec{m} \times ((\vec{u} \cdot \vec{\nabla})\vec{m}), \tag{2.15}$$

where $\vec{m} = \vec{M}/M_S$ is the reduced local magnetization, γ is the gyromagnetic constant, $\vec{H}_{eff}$ is the effective field. The parameter u is called the spin drift velocity and is proportional to the current density J and its P polarization:

$$|\vec{u}| = \frac{JPg\mu_B}{2eM_s}, \tag{2.16}$$

where, e is the electron charge.

The first term $(-(\vec{u} \cdot \vec{\nabla})\vec{m})$ was proposed by Slonczewski, in 1996, to describe the interaction between the polarized spins of flowing electric charges and the localized spins of atoms in a ferromagnet [99]. It was renamed the adiabatic STT term since it represents a perfect angular momentum transfer.

The second term $\beta\vec{m} \times ((\vec{u} \cdot \vec{\nabla})\vec{m})$ was proposed by Zhang and Li [115] and Thiaville *et al.* [103], independently. It is known as the β term and acknowledges the non-adiabatic effects due to relaxation of spin carriers. Without this non-adiabatic term, the integrated equation of 2.15 leads to two possible regimes: at low currents the spin transfer torque is balanced by internal restoring torques, the magnetization of the DW is tilted from the easy plane but the wall does not move under current. Above a certain threshold the internal torque cannot balance the STT anymore and thus, the DW motion takes place, as well as the magnetization precession. Without the β term the threshold currents obtained with micromagnetic calculations, is 10 times larger than the threshold deduced from the experiments.

Note that the terms $-(\vec{u} \cdot \vec{\nabla})\vec{m}$ and β are introduced phenomenologically. There is still debate concerning their physical origin but this discussion is beyond the content of this thesis.

Let us now discuss the current induced DW dynamics. There are two linear velocity v *versus* current density J regimes. They are separated by a complex transient regime. The Walker threshold J_W is: [77]:

$$J_W = \frac{4\pi\alpha e M_s^2}{g\mu_B P} \frac{\gamma\Delta}{|\beta - \alpha|}. \tag{2.17}$$

For thin films we need to include the demagnetizing factors and J_W is approximately written as:

$$J_W = \frac{4\pi\alpha e M_s^2}{g\mu_B P} \frac{\gamma\Delta}{|\beta - \alpha|} |N_y - N_x| \tag{2.18}$$

where $|N_y - N_x|$ is a geometrical factor with N_x and N_y being the demagnetization constants along the x and y directions considering that we have a thin sample in the xy plane with anisotropy perpendicular to the plane. For a current density lower than the threshold ($J < J_W$), the DW velocity moves in the steady flow regime and it is given by:

$$\bar{v} = \frac{\beta}{\alpha} u \tag{2.19}$$

This expression is equivalent to the velocity obtained with the Walker theory [98]. If the ratio β/α is smaller than 1, the DW velocity is less than the characteristic velocity of polarized charge carriers.

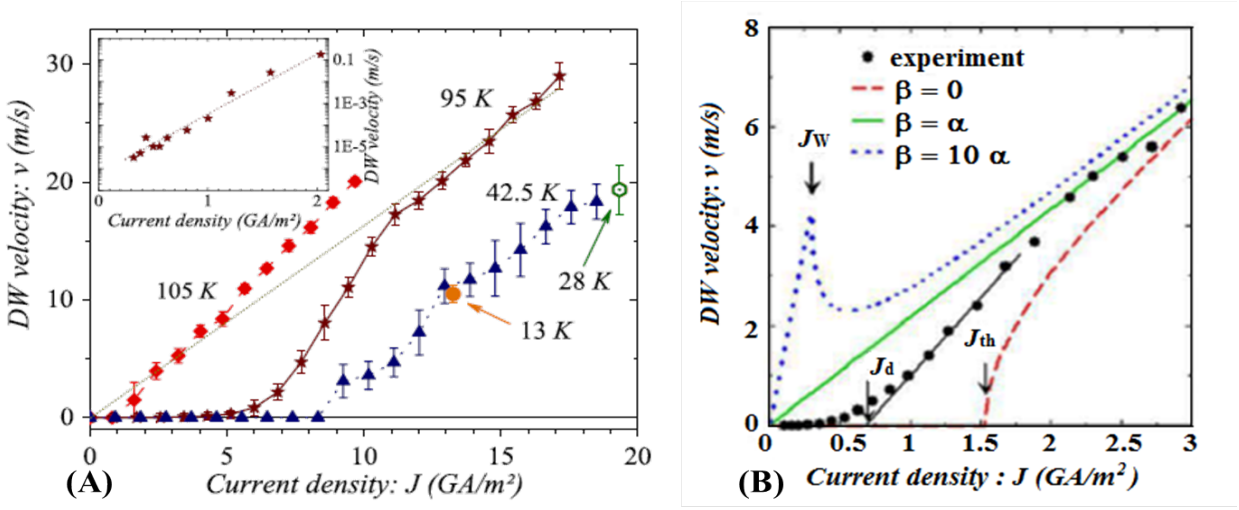

Figure 2.6: **Current driven DW velocity.** (A) Domain wall velocity v *vs* current density J in (Ga,Mn)(As,P) tracks at different T. Inset: Semilogarithmic plot of v measured at 95 K for the lowest current densities (Adapted from [20]). (B) Comparison between measured velocity v *vs* current density J at 104 K for (Ga,Mn)As tracks and prediction of the 1D model for different values of β/α with current polarization P adjusted. Theoretical threshold current (J_{th}) for $\beta = 0$ and the current density correspondent to the Walker breakdown takes place (J_W) are indicated (Adapted from [4].)

Analogous to field induced DW motion, when the current density is larger than J_W the magnetization angle in the domain wall ϕ precesses and the DW alternates between Bloch and Néel DW structures and the mobility is negative. The DW average velocity follows a negative velocity regime and is generally expressed as [103]:

$$\bar{v} = \frac{\beta}{\alpha} u - \frac{\Delta}{\alpha(1+\alpha^2)} \left[\left(\frac{\beta - \alpha}{\Delta} \right)^2 u^2 - \frac{(\alpha \gamma_0 H_K)^2}{4} \right]^{1/2}, \tag{2.20}$$

where $H_K = \frac{2K}{\mu_0 M_s}$. For much larger current ($J \gg J_W$) the velocity recovers a linear behavior

and it is expressed as:

$$v = \frac{\alpha\beta}{1+\alpha^2}u + \frac{u}{1+\alpha^2}. \tag{2.21}$$

Experimentally there has been progress in studying current induced domain wall motion. Adam *et al.* [4] were able to measure the domain wall velocity v as a function of the current density J in (Ga,Mn)As nanotracks close to the Curie temperature (see figure 2.6 (B)). They show that the domain walls move under a steady state regime when driven by low currents. This is only possible if there is a non-adiabatic contribution in the spin transfer torque. Moreover, they are able to estimate the value of the non-adiabatic term β which has a comparable magnitude ($\beta \sim 0.25$) to the adiabatic term α.

Later Curiale *et al.* [20] performed measurements of domain wall velocity driven by current density in (Ga,Mn)As nanotracks close to 0K (see figure 2.6 (A)). They found that the DW velocities are proportional to the spin drift velocity of the current carriers: they observed the steady state regime and found $\beta/\alpha \approx 1$.

2.2.2 Domain wall dynamics in the presence of pinning

At very low drive and in the presence of pinning, magnetic domain walls follow a non-linear dynamical behavior known as the creep regime. Within the creep regime, the magnetic domain wall (DW) can be considered as an elastic line moving in a random pinning potential, as illustrated in figure 2.7. The microscopic details of DW's magnetic structure are usually ignored.

In this section we will explain useful concepts on the theory of magnetic domain wall creep. We will start with a phenomenological approach inspired in type II superconductor vortices as historically occurred. Then we will present necessary concepts from the theory of disordered elastic interfaces moving in random media. We will also define the concept of Universality Class and critical exponents focusing in the quenched Edward-Wilkinson and Kardar-Parisi-Zhang universality classes. Finally we will discuss selected experimental results in DW creep that are relevant for our investigations.

Phenomenological approach to the creep regime.

A useful schematic description of the pinning dependent dynamical regimes is illustrated in figure 2.8. At low drives DW dynamics is controlled by pinning. The physical origin of the pinning sites varies on each material. For example in Pt/Co/Pt ultrathin films, it has been proposed that defects arise from fluctuations on the number of atomic Co layers [70], which produces anisotropy fluctuations. For (Ga,Mn)As the pinning could originate from the density fluctuations of the Mn atoms. When pinning is present the motion is thermally

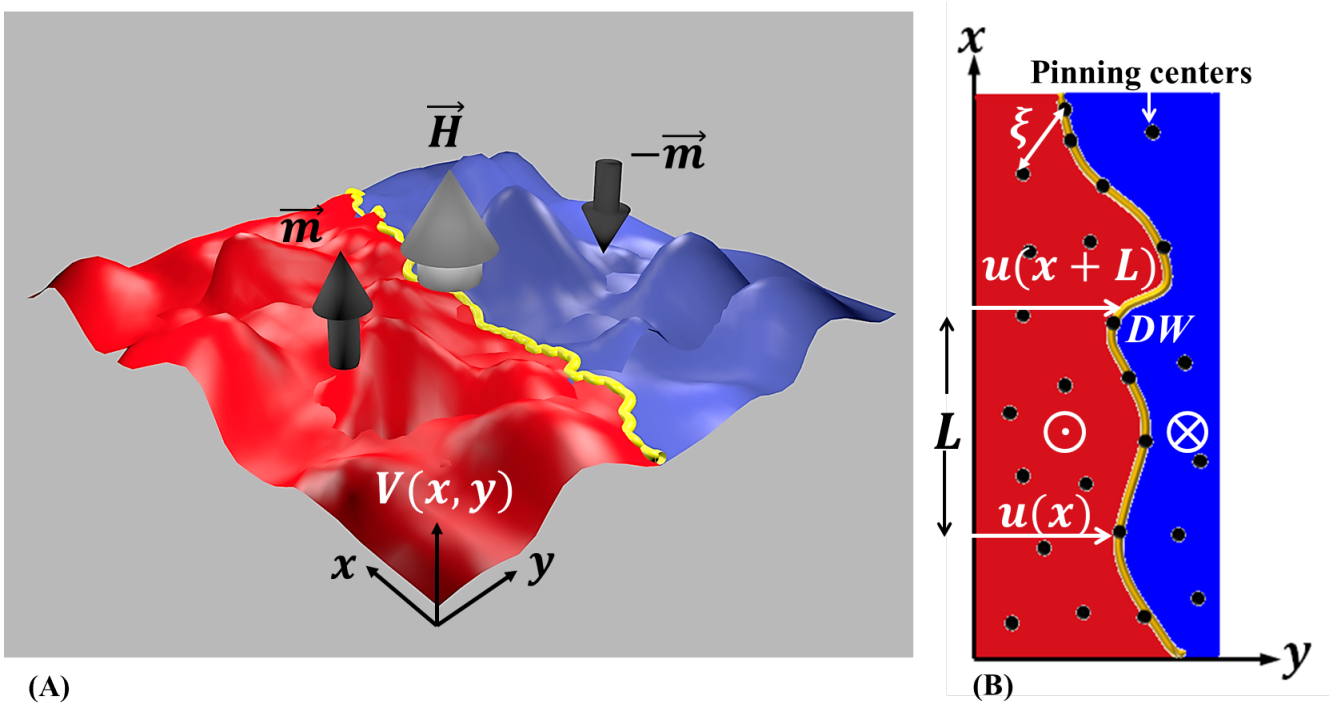

Figure 2.7: **Elastic DW in a pinning potential for a 2D sample.** (A) The out-of-plane magnetic field H favors the growth of up magnetization regions thus driving the domain wall (represented by the yellow string) in the direction y. Theoretically, the creep domain wall dynamics in a thin film can be modeled by the displacement of a one-dimensional elastic line coupled to an effective two-dimensional random pinning. (B) Presents the same surface view from above. The domain wall displacement is $u(x)$ where x is the coordinate of some point along the DW. The length ξ_i is the disorder correlation length and L is the length of a segment of the DW.

activated and increases rapidly with drive following an Arrhenius law $\ln(v) \sim f^{-\mu}$, where μ is the creep exponent (illustrated in Fig. 2.8 in purple), known as the creep law.

At the $T \to 0$ limit, the DW velocity is zero until the driving force reaches a depinning threshold f_d. Above the threshold, the velocity increases as $v(f, T \to 0) \sim (f - f_d)^{\beta}$. This behavior is analogous to an Ising crystal type second order transition called the depinning transition, except that the dependent parameter is the velocity and not the magnetization, and the control parameter is the driving force (magnetic field or current) and not the temperature.

At finite temperatures the depinning transition is rounded [12]: at the depinning threshold, the velocity follows a power law with temperature $v(f_d, T) \sim T^{\psi}$ which is known as thermal rounding. If the driving force is increased even more $f \gg f_d$, the DW velocity reaches the linear fast flow regime, where the velocity depends linearly on the driving force f as discussed previously.

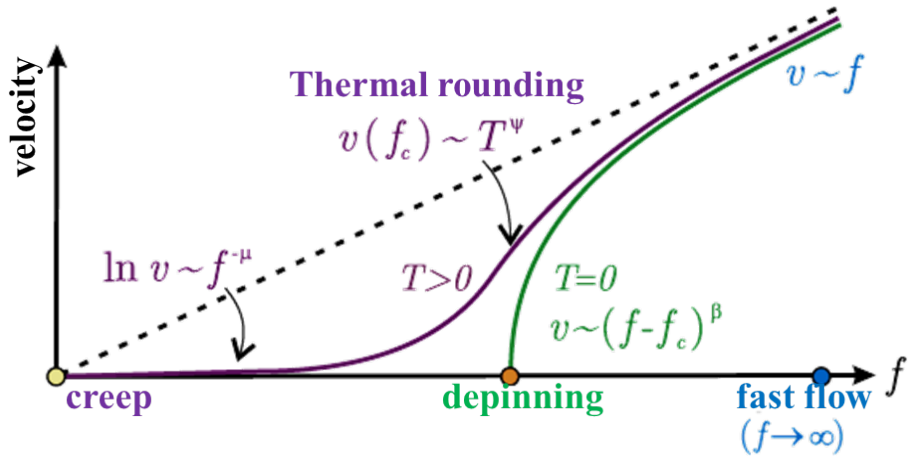

Figure 2.8: **Predicted domain wall dynamics in the presence of pinning.** The velocity v *vs* driving force f curve presents three different regimes: the creep (purple), the depinning transition (green) including the $T \to 0$ limit and thermal rounding, and the fast flow regime (blue). (Adapted from [36]).

Simplified domain wall creep model

The creep law can be derived from a simple model, which considers the total free energy of a DW segment of length L moving under a driving force (in this case magnetic field H) [70]. The elementary displacement covered by the DW at a given coordinate x is defined by $u(x)$ as it is shown in figure 2.7 (B). The total free energy of the DW is written as for :

$$F(u,L) = \underbrace{\epsilon_{el}\frac{u^2}{L}}_{\text{elasticity}} - \underbrace{f_{pin}\xi\sqrt{n_i\xi_i L}}_{\text{pinning}} - \underbrace{fu}_{\text{Zeeman}}. \tag{2.22}$$

Here, $f_{pin}^2 n_i \xi_i$ is the pinning strength of the disorder, $n_i \approx 1/\xi_i^2$ is the pinning center density, f_{pin} is the local pinning force, and ξ_i is the characteristic length of the pinning potential as it is shown in figure 2.7 (B). The first term corresponds to the elastic energy, $E_{el}(L,u)$, the second to the pinning energy, $E_{pin}(L,u)$, and the third to the Zeeman energy, $E_Z(L,u)$, with a driving force, $f = \mu_0 M_s H t L$, where t is the magnetic layer thickness.

Eq. 2.22 allows to define two important parameters related to pinning: the Larkin length L_c and the depinning field H_d. At the depinning transition the elementary displacement is expected to be of the same order as the average distance of the disorder $u \simeq \xi$ since we consider that the driving force at f_d is large enough to move the DW from one stable energetic configuration to the next one which are approximately a distance $\sim \xi$ away from each other. When the elastic energy, $E_{el}(L_c,\xi)$, is equal to the pinning energy, $E_{pin}(L_c,\xi)$, the maximum length for which the wall moves without deformation, is constrained by the DW's elasticity. This maximum length is known as the Larkin-Ovchinikov length:

$$L_c = \xi \left(\frac{\epsilon_{el}}{f_{pin}} \right)^{2/3} \tag{2.23}$$

For a DW, we have $\epsilon_{el} = \sigma t \simeq 4t\sqrt{AK}$, the domain wall energy density per unit of length where σ is the surface energy, K is the anisotropy and t is the film thickness. The Larkin-Ovchiniknov length is also related to the distance at which the DW is correlated, since the DW can be viewed as a succession of segments of length L_c that move independently one from the other.

We have already mentioned the depinning threshold f_d in the previous section. In this case we will refer to it as depinning field H_d, since we are assuming that the driving force is a magnetic field. At $T \to 0$, we obtain this critical field H_d from the Zeeman energy needed to depin a DW. Therefore it can be deduced from the equality: $E_{pin}(L_c, \xi_i) = E_Z(L_c, \xi_i)$ and Eq. 2.23, an expression for the depinning field [69]:

$$H_d = \left(\frac{\epsilon_{el}\xi}{M_s t} \right) \frac{1}{L_c^2} \tag{2.24}$$

This is the value of the depinning threshold below which the DW will not move for $T \to 0$. At finite temperature there is DW motion at fields $H < H_d$.

Now we discuss the concept of geometrical roughness. In the creep regime where the DW motion is sensitive to pinning, a DW segment of length $L > L_C$, the DW is not flat and therefore it becomes rough. This model assumes that there are scaling relations that connect the displacement, u, to the length of the DW segment L. This is known as self affinity, i.e. a segment L of DW presents self affinity when its displacement u can be rescaled as $L' = aL$ and $u' = a^{-\zeta}u$. With this rescaling, we obtain a statistically equivalent DW $u'(L')$ where a and ζ are a scaling constant and exponent such that $u(aL) \sim a^{\zeta}u(L)$ [1, 36].

The geometrical roughness of a self affine interface can be quantified by the root-mean-square fluctuations around its mean value, or the global width of the interface: $W(R) = \langle [u(x) - \langle u \rangle]^2 \rangle^{1/2}$, where R is the total length of the DW. The global width of saturated interfaces scales as $W(R) \sim R^{\zeta}$ [33, 36, 45] where ζ is also known as the roughness exponent, sometimes written α [90] or χ [71]. This is known as the Family-Vicsek ansatz.

Experimentally the scaling of the global width is very difficult to determine. For self-affine surfaces, local measurements of the interface fluctuations over a smaller window $L < R$ (as shown in figure 2.7 (B)) have a power law behavior as a function of L with the same roughness exponent. This quantities are both the local width $w*(L) = \langle [u(x) - \langle u \rangle_L]^2 \rangle_L{}^{1/2} \sim L^{\zeta}$ and the displacement-displacement correlation function:

$$w(L) = \langle [u(x) - u(x+L)]^2 \rangle^{1/2} \sim L^{\zeta} \tag{2.25}$$

In many cases the displacement-displacement correlation function (Eq. 2.25) and the local width are equivalent to the global width $W(R)$, however it is not always true, for example when $\zeta > 1$ [71]. However those cases are not found in the systems we study through this thesis.

We note that the roughness exponent carries information about the way the roughness evolves when increasing the system size R or the length scale L.

In order to relate this formalism with the phenomenological approach of the creep regime, we assume that the DW is self-affine. Subsequently, for segments where the length $L > L_c$, we can rescale the displacement $u(L)$ as $u(L) \propto u_c(\frac{L}{L_c})^{\zeta}$ for $L > L_c$, where u_c is some scaling constant and L_c is the previously defined Larking length. If we substitute this in the free energy equation 2.22 we get:

$$F(u, L) = U_c \left(\frac{L}{L_c}\right)^{2\zeta-1} - \frac{2fL_c}{L}\left(\frac{L}{L_c}\right)^{\zeta+1} \tag{2.26}$$

Minimizing this expression with respect to the segment length L we obtain the optimal length L_{opt} to overcome the energy barriers separating two stable DW configurations. In another way L_{opt} is the optimal DW length that triggers the thermally activated events between energy barriers:

$$L_{opt} = L_c \left(\frac{U_C(2\zeta + d - 2)}{(\zeta - d)}\right)^{-\frac{1}{2-\zeta}} \left(\frac{1}{2M_S L_c u_c H}\right)^{-\frac{1}{2-\zeta}} \tag{2.27}$$

Replacing $L = L_{opt}$ in the expression for the energy, we obtain the smallest possible energy barrier, which can be written as:

$$\Delta E = k_B T_d \left[\left(\frac{f}{f_d}\right)^{-\mu}\right] \tag{2.28}$$

where f_d is the depinning threshold driving force, μ is the creep exponent and T_d is the depinning temperature. If we simplify the DW motion as a one dimensional phenomena or a particle in a pinning potential, ΔE represents an effective height of energy barrier, which should be overcome in order to produce any DW motion. From expressions 2.26 and 2.28 we obtain the scaling relation between ζ and μ that for $1d$ surfaces in $2D$ media is $\mu = (2\zeta - 1)/(2 - \zeta)$ and can be generalized for any dimension d:

$$\mu = \frac{d + 2\zeta - 2}{2 - \zeta} \tag{2.29}$$

As mentioned before the DW velocity in the creep regime ($f \ll f_d$) follows an Arrhenius law. With the energy barrier expression (Eq. 2.28) we can rewrite the DW velocity as [70]:

$$\ln v(f,T) \propto \left(\frac{-\Delta E}{k_B T}\right) \tag{2.30}$$

Numerical simulations: universality classes and critical exponents.

Theoretical models describing the motion of magnetic domain walls when there is pinning present, often treat the domain wall as an independent system and ignore the microscopic details of the sample. Very generally DWs are described by elastic interfaces moving in a disorder media. A very naive way to understand this concept is thinking that the elastic surface moving in the absence of disorder would adopt a straight configuration in order to minimize its energy. However, in the presence of disorder, the interface adopts a configuration that accommodates around the pinning sites, therefore the interface adopts a rough configuration rather than a straight one [40].

The interplay between elasticity and disorder in driven interfaces gives rise to universal dynamical properties. The latter can be contained in relatively simple models which describe a large variety of phenomena such as: propagating interfaces, for example surface growth [1], fractures in solid materials [87], combustion fronts [79] and domain walls in ferromagnetic and ferroelectric materials [70, 85], periodic systems like vortex lattices in type-II superconductors [7] or Wigner crystals [17]...

In order to define what a universality class is, we recall some concepts of phase transition theory. As a system approaches a second order phase transition, the control variable reaches a critical value f_d, some physical quantities of the system present singularities at this critical point. The dependence in the order parameter as a function of the control parameter can be described as a power law. For instance in the Ising model, the magnetization M is the order parameter, and the temperature T is the control parameter when the system approaches the paramagnetic-ferromagnetic transition and it follows a power law $M \sim (T_C - T)^{\beta}$ [84, 86].

Close to the critical value f_d (the driving force for our purposes), the system's degrees of freedom start to couple among them. The size region where these degrees of freedom are coupled is characterized by a given correlation length. As the system approaches the phase transition, this correlation length diverges, and therefore the system becomes scale invariant. For this reason, thermodynamical observables are described as homogeneous functions through the whole physical system, and exhibit power law variations characterized by critical exponents [13].

These critical exponents are shared by groups of different physical systems with very diverse microscopic properties. In that sense, the exponents are universal and the set of physical systems sharing the same critical exponents belong to the same universality class.

These universality classes are determined by general properties of the systems like dimensionality, symmetry of the order parameters, range of interactions and type of disorder [84, 13].

Uniformly driven elastic interfaces as DWs moving in quenched disorder, i.e. when the disorder does not evolve with time, are described by the so-called quenched Edward-Wilkinson (qEW) equation that constitutes itself a universality class. In this case the order parameter is the velocity of the interface and the control parameter is the driving force (the magnetic field). The qEW universality class can be minimally described by the overdamped dynamic equation [36]:

$$\gamma \frac{\partial u(x,t)}{\partial t} = c\frac{\partial^2 u(x,t)}{\partial x^2} + F_p(u,x) + f + \eta(x,t), \tag{2.31}$$

where $u(x,t)$ is the scalar displacement of position x of the interface, as it is shown in figure 2.7. We define the equation term by term. The first term on the right side of the Eq. 2.31 describes the elasticity. It assumes only small deformations and short range interactions with stiffness constant c. This model ignores overhangs, loops and assumes that $u(x,t)$ is single valued.

The second term $F_p(u,x)$ is the pinning force which originates from the inhomogeneities in host materials and it is characterized by its disorder correlator: $\overline{F_p(u,x)F_p(u',x')} = \rho(u-u')\delta(x-x')$, where $\rho(u)$ is a short-ranged function. Let us discuss further this concept. Generally speaking the disorder describes inhomogeneities in a given material, that can be complex in real samples. Analytically we can describe them as a stochastic variable $V(x,y)$ with a statistical distribution $P[V]$. We can distinguish two different types of pinning, a few individual pinning centers or the strong pinning limit and the collective action of many weak inhomogeneities or weak pinning [52].

Further on, depending on the range of spatial correlations, two universality classes can be further defined for weak collective pinning. Random bond disorder (RB), originally describing an Ising model with randomly varying site-site (exchange) interaction, corresponds to short-ranged correlations. This type of disorder corresponds to impurities that directly attract or repel the interface. The corresponding pinning force is $F_p(u,x) = -\partial_u V(u,x)$ where $V(u,x)$ is a random potential, and therefore $\int_u \rho(u) = 0$ [14].

In contrast, random field disorder (RF), associated with an Ising model with randomly varying magnetic field at each site, is long-ranged, i.e. the pinning energy is affected by all the randomness that the interface has encountered in its previous path. The corresponding pinning potential is $V(u(x),x)$, a random walk as a function of u with a diffusion constant $\int_u \rho(u) > 0$ [80].

Even though, for the purposes of this thesis, we are concerned only in the weak pinning random bond qEW universality class with anharmonic corrections in the elasticity , all these different universality classes (with different critical exponents) share the same basic physics of the qEW model discussed in the following sections [36].

The last two terms in Eq. 2.31 are a uniform driving force f and the thermal bath at temperature, T, which is modeled by the Langevin noise $\langle \eta(x,t)\eta(x',t')\rangle = 2k_B T\gamma\delta(x - x')\delta(t - t')$.

The first historical variation of the Edward-Wilkinson equation was proposed by Mehran Kardar, Giorgio Parisi and Yi-Cheng Zhang, and it is known as the KPZ equation [1, 56, 55]. They assumed that a local growth ($v\delta t$) occurs normal to the interface, which generates a displacement $\delta u(x)$ along the y axis (see Fig. 2.7 (B)). From the Pythagorean theorem $\delta u = [(v\delta t)^2 + (v\delta t\nabla u)^2]^{1/2}$, it is obtained $v\delta t[1 + (\nabla u)^2]^{1/2} \approx v\delta t[1 + (1/2)(\nabla u)^2]$ for $|\nabla u| \ll 1$. Therefore, they proposed a new equation:

$$\gamma\frac{\partial u(x,t)}{\partial t} = c\frac{\partial^2 u(x,t)}{\partial x^2} + \frac{\lambda}{2}\left(\frac{\partial u(x,t)}{\partial x}\right)^2 + F_p(u,x) + f + \eta(x,t), \tag{2.32}$$

which is the qEW equation with an additional non linear term $((\lambda/2)(\partial u/\partial x)^2)$. The quenched Kardar-Parisi-Zhang (qKPZ) equation constitutes a different universality class from the quenched Edward Wilkinson equation [1]. Moreover the sign of the λ constant in the non linear term plays an important role in the behavior of the surface growth. It induces growth when $(\lambda > 0)$ and decay if $(\lambda < 0)$ [76].

Now that we have defined the universality classes we are interested in, we will discuss the critical exponents. They reflect the geometry of the system and its dynamical properties. The value of the critical exponents depends on the magnitude of the drive, and on the scale at which the system is observed, as illustrated in figure 2.9.

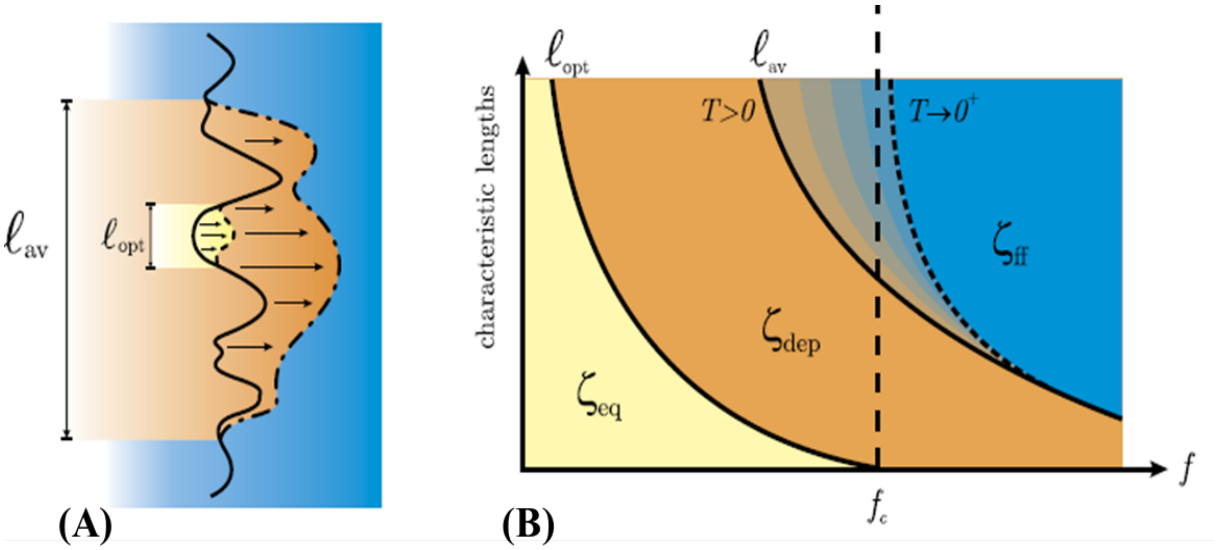

Figure 2.9: **Characteristic crossover lengths.** (A) Crossover lengths: L_{opt} represents the optimal excitation length and L_{av} the deterministic avalanches. (C) Crossover lengths *vs* driving force at different temperature T. (Adapted from [36])

The roughness exponent ζ does not vary continuously when increasing the driving

force f. As it is shown in Fig. 2.9 (B) there is a characteristic roughness exponent for each one of the dynamical regimes (creep, depinning and fast flow) presented in the previous subsection. Each one of these regimes is self affine at asymptotically large length scales. The universal behaviors are characterized by a different roughness exponent (ζ_{eq}, ζ_{dep} and ζ_{ff}, respectively) [36] and separated by two crossover lengths L_{opt} and L_{av} that we define now.

Within the creep regime ($f \ll f_d$), at small but finite temperature ($T \ll T_d$), the interface dynamics results from a sequence of uncorrelated jumps around metastable configurations [37]. The typical size of this activated rearrangements is L_{opt}. Close to the depinning threshold f_d, the interface motion is jerky and DW moves in large and abrupt events called avalanches. The characteristic length of the avalanches is L_{av}. The variation of L_{opt} and L_{av} with the drive f are illustrated in Fig. 2.9. As it can be observed, the predicted critical exponent is expected to depend on the length scale at which the system is observed and on the magnitude of the driving force.

Table 2.1 summarizes the predicted exponents for the creep and depinning regimes:

	ζ_{eq}	ζ_{dep}	μ	β	ψ
qEW ($1d$)	2/3 [70, 91, 63]	~ 1.25 [63], 0.63^* [91]	1/4 [70]	0.25 [10, 12, 35]	0.15 [10, 12, 35]
qEW ($2d$)	$\sim 2/5$ [70]	0.45 [91]	1/2	0.6536 ± 0.026 (RF) [94]	2.336 ± 0.2 (RF) [94]
qKPZ ($\lambda < 0$)	0.997(5) [75]	0.515(20) [75]	1	-	-

Table 2.1: **Summary of numerical results.** Critical exponents for the quenched Edward-Wilkinson universality class for a $1d$ and a $2d$ interface and the negative KPZ universality class of a $1d$ interface. The first two columns show the roughness equilibrium ζ_{eq} and depinning ζ_{dep} exponents. Next we show the creep exponent determined from the scaling relation 2.29. The last two columns show the critical exponents for the velocity v in the depinning transition: β (for $T = 0$) and ψ (for $f = f_d$). The symbol (*)indicates that this critical exponent was calculated taking into account anharmonic corrections in the elasticity.

Depinning transition: scaling approach.

At the depinning threshold $f = f_d$, the moving interface is self-affine, both in space and in time. As we mentioned before, just above the depinning threshold $f \geq f_d$, the velocity follows a power law in the $T = 0$ limit, more precisely:

$$v(f, T) \propto (f - f_d)^{\beta} \tag{2.33}$$

When the temperature is finite, there is no sharp transition between zero- and finite-velocity regimes. Even below the critical force, f_d, the interface is able to move since thermal activation is enough to overcome the effective energy barriers generated by the

disorder. This thermal rounding of the depinning transition can be characterized, at the critical force $f = f_d$, by a power-law vanishing of the velocity with temperature as:

$$v(f_d, T) \propto T^{\psi} \tag{2.34}$$

with ψ the thermal rounding exponent [74, 12]. Following the more general scaling arguments, the velocity can be described as a generalized homogeneous function [88, 100]:

$$y = g\left(\frac{x}{x_0}\right) \tag{2.35}$$

where $x = [(H - H_d)/H_d]^{\beta}(T/T_d)^{-\psi}$ and $y = (v/v_T)(T/T_d)^{-\psi}$ are the scaled field and velocity respectively.

Using Langevin dynamics numerical simulations, Bustingorry *et al.* [10] calculated a value of $\psi = 0.15 \pm 0.01$ for a $1d$ interface moving in a random-bond disorder environment with short-range correlations and short-range elasticity. The β exponent was predicted to have a value of $\beta = 0.245 \pm 0.006$ through non steady dynamics simulations of the continuum displacement qEW equation [35]

At the threshold (with $T = 0$), the motion is characterized by avalanches of a divergent typical size L_{av} (see figure 2.9 (B)), which also follows a power law $L_{av} \sim (f - f_d)^{-\nu_{dep}}$. The velocity of the interface depends also on the characteristic time of the avalanche $t \sim L_{av}^{z_{dep}}$. All this exponents are constrained by scaling relations. In particular β, ν_{dep}, z_{dep} are related by the hyperscaling relation $\beta = \nu_{dep}(z_{dep} - \zeta_{dep})$ [63].

Field induced domain wall creep

In 1998, Lemerle *et al.* verified that the DWs velocity in ultrathin ferromagnets followed the predicted creep law with a creep exponent $\mu = 1/4$, and measured the roughness exponent $\zeta = 0.69 \pm 0.07$, which is close to $\zeta = 2/3$ [70]. This experiments agree with predictions from functional renormalization group theory [14] and numerical simulations for $1d$ elastic lines moving in a random bond weak pinning potentials [36, 92]. Therefore, it was experimentally shown that the creep motion of DWs in ultrathin ferromagnetic films with pinning disorder belonged to the qEW universality class. The logarithmic plot of the velocity v *vs* $H^{-\mu}$ obtained is shown in figure 2.10 (A). In this experiment only the creep regime is observed since it was possible to obtain samples with reduced pinning strengths.

Almost ten years later, Metaxas *et al.* [73], increased the velocity range explored for a similar samples changing the thickness of the Co layer. They were able to observe the linear fast precessional flow regime and showed qualitatively, that the domain wall shape was more "rough" within the creep regime and became smoother as the velocity increased entered in the fast flow regime, [73]. This work also shows for the first time the shape of

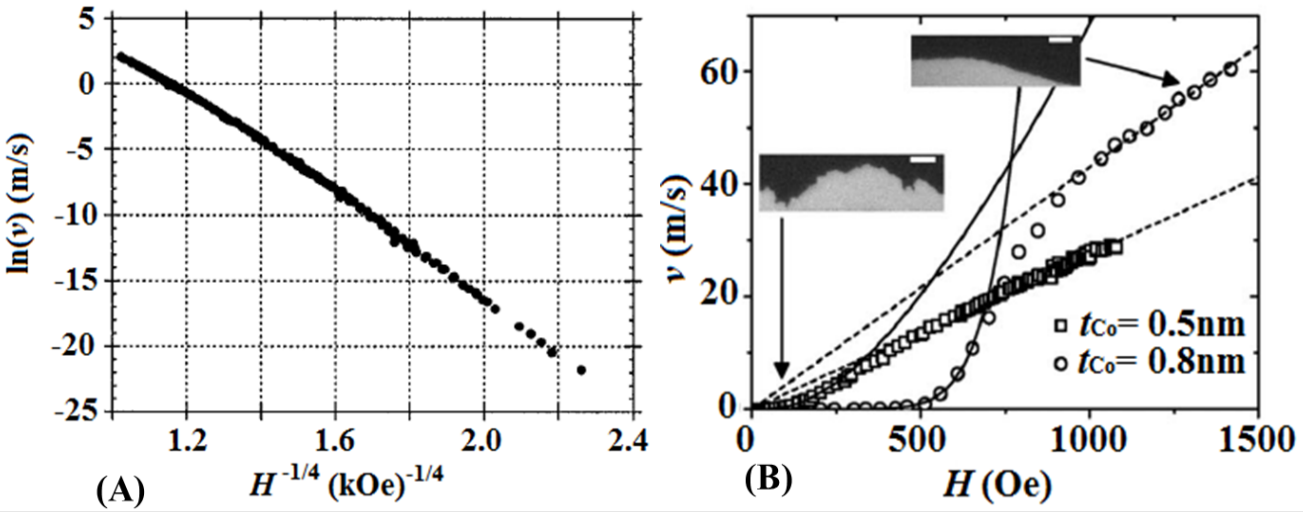

Figure 2.10: **Experimental observation of the creep regime in Pt/Co/Pt thin films.**(A) Log-scale of the mean domain wall velocity *vs* $H^{-1/4}$ at room temperature [70]. (B) Domain-wall velocity v *vs* applied magnetic field H, for different Co thicknesses $t_{Co} = 0.5nm$ and $t_{Co} = 0.8nm$ samples. At high field $v = mH$ fit to the flow data (dashed line) and at low field, the creep law fits the data points (solid line). The insets show domain images in the $t_{Co} = 0.8nm$ film at fields, which lie within the creep and flow regimes. The white scale bars are 5 μm long [73].

the depinning transition that varied with the Co layer thickness, as it can be observed in figure 2.10.

Regarding the pinning energy barrier, it was evidenced by Jeudy *et al.* [51], that the magnetic domain wall motion is controlled by a unique universal reduced energy barrier function (see figure 2.11). They measured the velocity *vs* field in (Ga,Mn)(As,P) and TbFe thin films. They deduced the pinning barrier height ΔE from the velocity curves and show that all the reduced energy barrier curves $\Delta E/k_B T_d(T)$ collapse well onto a single master curve over the full field-range of existence of the creep regime $0 < H/H_d < 1$ [51]. Afterwards, they compared with the data published for other materials and showed that the reduced energy barrier for other materials, could be plot into the same master curve. Finally they concluded that the full thermally activated creep motion, observed below the depinning threshold, is described by a unique universal energy barrier function which is written as:

$$\Delta E = k_B T_d \left[\left(\frac{f}{f_d} \right)^{-\mu} - 1 \right]. \tag{2.36}$$

As we mentioned before, the universality class depends, among other things, on the system's dimensionality. There is experimental evidence showing the change in universality class due to a dimensional transition in a paper authored by Kim, *et al.*, where they change the width of Ta/Pt/CoFe /Pt tracks. Figure 2.12 shows the DW velocity in semilogarithmic

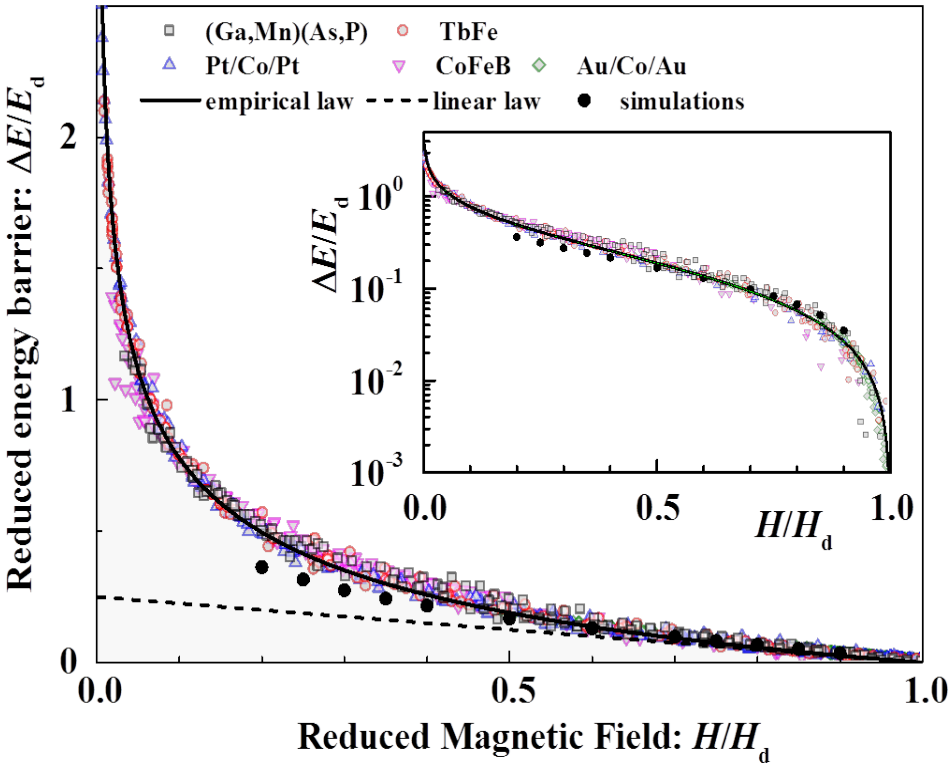

Figure 2.11: **Universal energy barrier of the creep regime.** The variation of the reduced energy barrier height $\Delta E/E_d$, with $E_d = k_B T_d$, is reported as a function of the reduced force H/H_d, for five different magnetic materials and for temperatures ranging from 10 to 315 K. The solid line is a plot of Eq. 2.36. The black circles correspond the predictions of Ref. [63]. The dashed line is the linear variation of the energy barrier close to the depinning field ($H = H_d$). Inset: Universal barrier presented in semi-log scale showing a good quantitative agreement with Eq. 2.36 over more than 3 orders of magnitude. (adapted from [51])

scale *vs* $H^{-1/4}$. It is shown that for tracks narrower than 600 nm the semi-logarithmic velocity deviates from the expected creep law for $1d$ elastic DW. In comparison, the domain wall velocity in the wider tracks agree with the creep law predicted for a $1d$ elastic line with a creep exponent $\mu = 1/4$. When the width of tracks becomes smaller than L_{opt}, the DWs move like stochastic particles hopping back and forth in a quenched disorder potential. This belongs to a different criticality.

Current induced domain wall creep

R. A. Duine and C. Morais Smith [29] present a theoretical model for current driven DW motion moving perpendicular to the direction of electric current in one dimension ($1d$) in the presence of disorder and thermal fluctuations. They took into account the chirality of

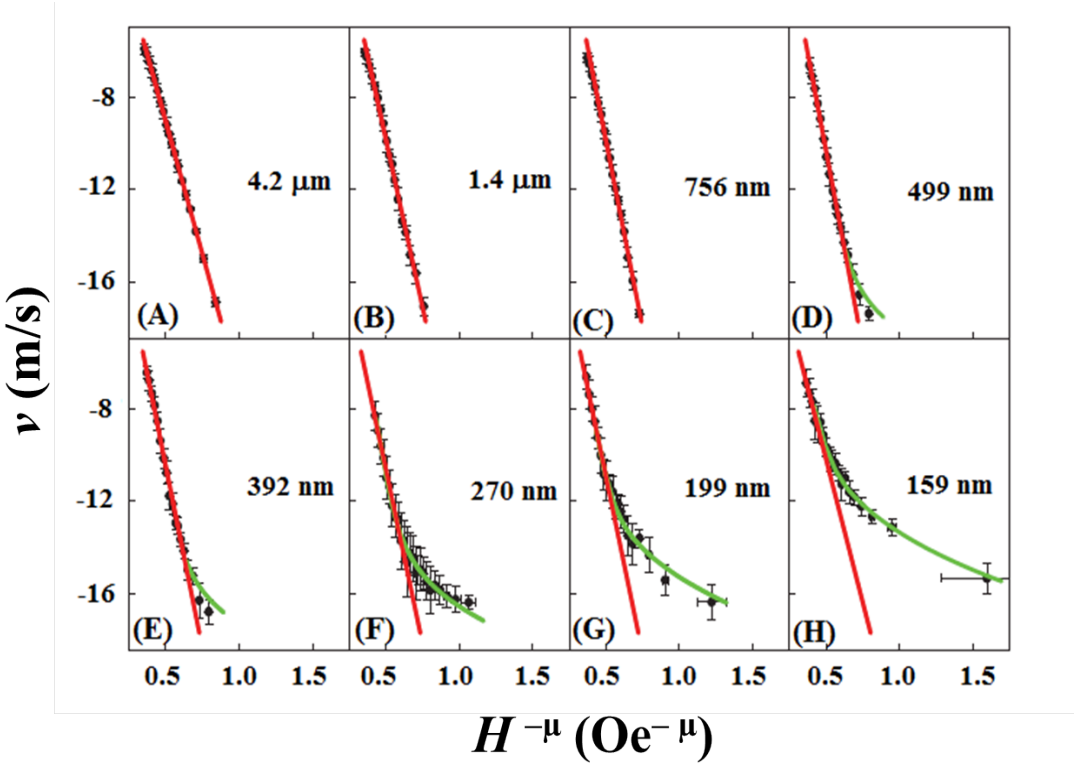

Figure 2.12: **Criticality of DW speed along ferromagnetic Ta/Pt/CoFe/Pt nanowires.** Data are shown for different wire widths: $4.2\mu m$ (A), 1.4 μm (B), 756 nm (C), 499 nm (D), 392 nm (E), 270 nm (F), 199 nm (G) and 159 nm (H). The red lines are the best fit to the $1d$ elastic line criticality ($\mu = 1/4$ is used) and the green lines are the best fit to the $0d$ criticality (Adapted from [58]).

the domain wall and model it as an overdamped vortex line. They introduced an extrinsic pinning potential, and calculated the energy barrier. They obtained a creep exponent of $\mu = 1/4$ when the β term, in the non-adiabatic term of the spin transfer torque, is different from zero. Also Ryu *et al.* [96] studied theoretically the current and field driven creep regime in a nanowire. They conclude that when the tilting angle of the DW is small, and only the non adiabatic contributions of STT are taken into account, the creep regime induced by current and field belong to the same universality class.

Experimentally, Moon *et al.* [76] reported domain wall motion in the creep regime in Pt/Co/Pt ultra thin films driven by current and magnetic field as it is shown in figure 2.13. They generated a straight domain wall and then applied constant magnetic field ($1\ mT$). Then, separately, they applied constant current density ($10^{10} A/m^2$). When the magnetic field is applied, the DW shape does not change significantly and the velocity remains constant at every time step (Figure 2.13 (B)). In contrast, when electric current density is biased perpendicular to the DW, the linear DW develops the shape of mountains with a constant slope. The average velocity of the DW decreases strongly when the faceting is present (Figure 2.13 (A)).

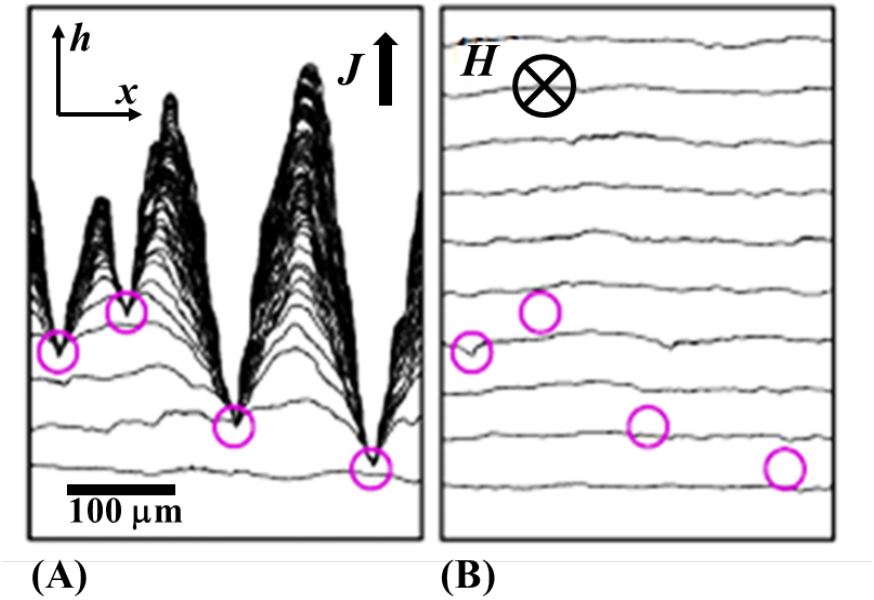

Figure 2.13: **Sequence of magnetic domain walls driven by current and field.** (A) Time-resolved DW lines superimposed sequentially with a constant time step (3 min) driven by a current density of $10^{10} A/m^2$ and by magnetic field $1.0mT$ (B). The circles indicate the position of strong pinning sites that appeared in the current driven motion. (Adapted from [76]).

Moon *et al.* analyzed the roughness exponent in domain walls driven by current density and compared them with the ones driven by magnetic field. In figure 2.14 (A) is shown typical correlation functions for field and current induced DW motion. From this plots, the slope in the linear part is two times the roughness exponent. They obtained different values for current (J) and field (H) driven DW motion: $\zeta_J = 0.99 \pm 0.01$ and $\zeta_H = 0.64 \pm 0.04$ correspondingly. This suggested that the DW motion induced by different drives belongs to different universality classes. Their results for current induced DW motion agree with theoretical predictions for the quenched Kardar-Parisi-Zhang equation of motion (Eq.2.32) when $\lambda < 0$ [56, 76]. Moon *et al.* concluded that the current induced DW motion belongs to the negative qKPZ universality class ($\lambda < 0$) since for a negative λ, the interface forms a typical roughness called facets. However they also measured ζ_J in the direction normal to the DW and find $\zeta_{J\perp} = 0.69 \pm 0.04$ [76] which is similar to the roughness exponent found for field driven DW motion, and predicted for the quenched Edward-Wilkinson universality class.

Yamanouchi *et al.* [112] compared the creep exponent in (Ga,Mn)As tracks for magnetic field and current driven DW motion. They obtained $\mu_H = 1.2 \pm 0.01$ for field induced DW motion and $\mu_J = 0.33 \pm 0.06$ and argue that the discrepancy to other values reported previously is caused by random field disorder in (Ga,Mn)As.

Another work comparing the universality class between magnetic field and current

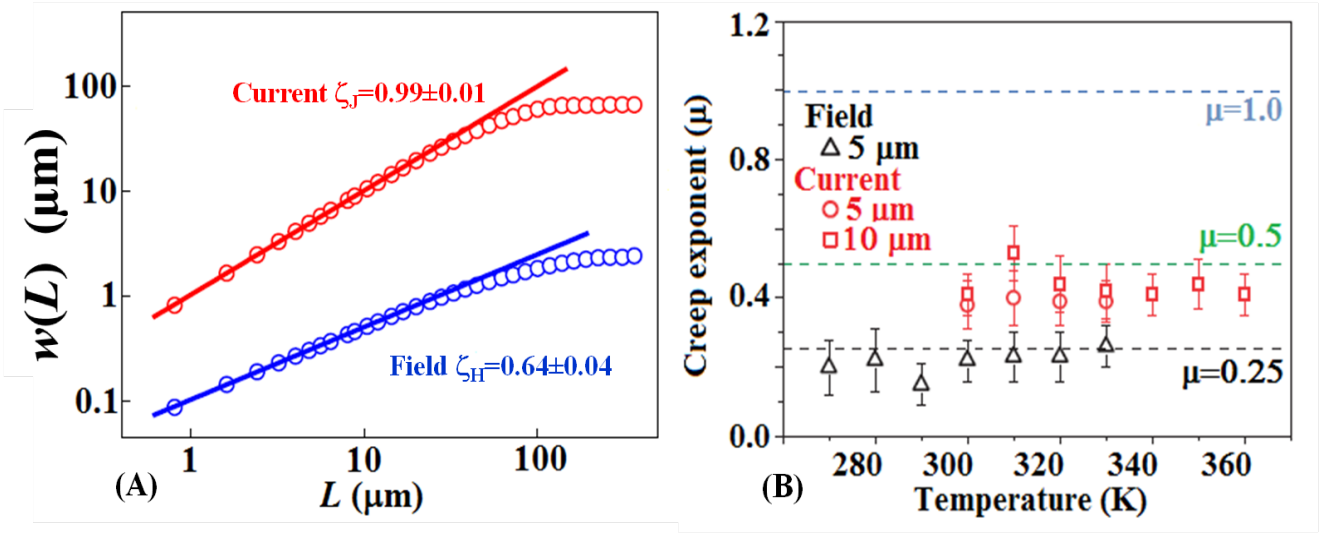

Figure 2.14: **Measured critical exponents for current induced DW motion.**(A) Log-log scaling plot between the DW segment length L along the x axis and the roughness amplitude w along the h axis for DWs driven by the current (red) and field (blue). w is defined as the standard deviation of the roughness fluctuation over the length L [76]. (B) Creep exponent μ for field- and current-driven DW creep. Broken lines show different universality classes. Error bars come from the fitting error of the velocity curves [31].

driven DW motion is the one published by DuttaGupta *et al.* [31] for CoFeB/MgO metallic tracks. They obtained the velocity v *vs* drive $f = H, J$ for current and field, plotted the velocity logarithm *vs* $f^{-\mu}$ ($f = H, J$) and extracted the value of the creep exponent μ. In figure 2.14 (B) we show the results they obtained for field and current at different temperatures.

For field induced DW motion, the measured creep exponent $\mu_H = 0.23 \pm 0.07$ is in good agreement with other experimental results and the predicted value from the Edward-Wilkinson universality class [70, 7]. For current induced DW motion, they measure $\mu_J = 0.39 \pm 0.06$, which suggests a different universality class. The current through the stacks with structural inversion asymmetry gives rise to Spin Orbit Torque (SOT) which has an effect on the DW if it is Néel type wall. However they found that the non-adiabatic STT and SOT with the anti-damping symmetry are not dominant for the current induced DW motion. Moreover, they estimated that the contribution of the field-like component of SOT is estimated to be less than $\pm 0.12mT$. As this value is much smaller than the typical magnetic field scale for which DW motion is observed.

They attribute the change of universality class mainly to the adiabatic STT as the most dominant factor driving the DW [31]. However there is still not a theoretical model that predicts this value.

Therefore, the issue of universality class in current induced DW motion is still controversial. Several measurements of power law exponents are contradictory. Particularly, it

would be interesting to discuss the universal nature of the measured exponents through test of compatibility with predicted scaling laws.

2.3 Chapter summary

In this chapter we made a brief introduction of the state of the art in order to understand dynamical properties of magnetic domain walls driven by magnetic field or electric current in the presence of pinning. We began by discussing the origin of ferromagnetism in (Ga,Mn)As and Pt/Co/Pt. We presented the hole mediated long distance exchange as key ingredient in the spin unbalance at the Fermi level resulting in the ferromagnetic behavior in (Ga,Mn)As. In the case of Pt/Co/Pt the hybridization at the interface causes the perpendicular magnetic anisotropy. Afterwards we summarized the energy terms that give rise to the magnetic domains and domain wall structures when the total energy is minimized.

Next, we gave a summary in magnetic domain wall dynamics when there is no pinning present. We discussed the main characteristics of the LLG equation as well as the predictions for the velocity as a function of field. As a result we expect the velocity to present two different linear regimes (the steady and the precessional) separated by the Walker breakdown and an intermediate regime with negative mobility. We then extended the discussion to current driven DW dynamics, introducing the LLG equation with the adiabatic and non-adiabatic terms of the spin transfer torque. We showed that there is an equivalent Walker like current that separated two linear regimes. We also showed some experimental results that confirmed these theoretical predictions.

In the last part we summarized some relevant results in order to understand DW dynamics in the presence of disorder. We began with an empirical model proposed by Lemerle *et al.* [70]. From this model it is possible to obtain the Arrhenius law followed by the velocity in the thermally activated creep regime and the scaling relation between the creep and the roughness exponent.

CHAPTER 3

Experimental techniques

"The chief cause for my perplexity was what I may truly call the exquisite delicacy of the magnetic mirror as a test for fixing the positions of the plane of polarization of the incident light."

John Kerr. **On Rotation of the Plane of Polarization by Reflection from the Pole of a Magnet**

In this section we describe the experimental techniques, measurement protocols and the samples used in this thesis. The first part focuses on the Magneto-Optical Kerr effect (MOKE) microscopy and the experimental setup. Next, we present the main characteristics of samples used throughout this thesis: namely (Ga,Mn)(As,P) and Pt/Co/Pt films. Finally we explain in detail the methods used to measure the domain wall (DW) velocity, the correlation function of displacements, and the roughness exponent.

3.1 MOKE microscopy

For the studies performed in this thesis we used essentially MOKE microscopy. In this section we explain briefly the fundamental principles in MOKE microscopy and then describe in detail the experimental setup designed to observe magnetic domains in magnetic thin films with perpendicular anisotropy.

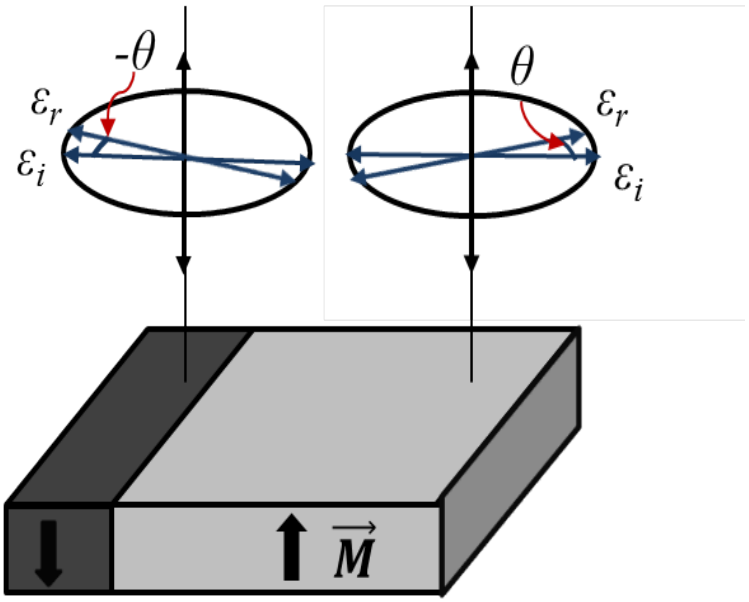

Figure 3.1: **Geometry of polar magneto-optical rotation.**Geometry of polar magneto-optical Kerr effect. Polar rotation for a film with perpendicular magnetic anisotropy for opposite magnetization direction.

3.1.1 Magneto-Optical Kerr effect

The Kerr effect was discovered by John Kerr in 1877 [57]. The magneto-optic Kerr effect (MOKE) is the phenomenon by which polarized light reflected from a magnetized material has a slightly rotated plane of polarization [2]. The change in the polarization of reflected wave with respect to the incident one is characterized by an angle θ and an ellipticity $\epsilon = b/a$ as shown in figure 3.1. There are three possible MOKE configurations according to the magnetization direction with respect to the sample surface: polar, longitudinal and transverse.

In our experiments we use the polar Kerr configuration. Here, the magnetization is perpendicular to the sample's surface. The incident light beam polarization plane is also perpendicular to the sample's surface as shown in figure 3.1. Depending on the direction of the magnetization M_s or $-M_s$, the polarization vector, the polarization vector ε_r of the reflected beam is deviated an angle θ or $-\theta$ with respect to the polarization vector of the incident beam ε_i [2].

3.1.2 Experimental setup

The Kerr microscope uses the so-called Köhler illumination technique in order to obtain an homogeneous lightning of the sample. To improve the quality of the image, it is important to separate well the conjugated planes of the sample and light source.

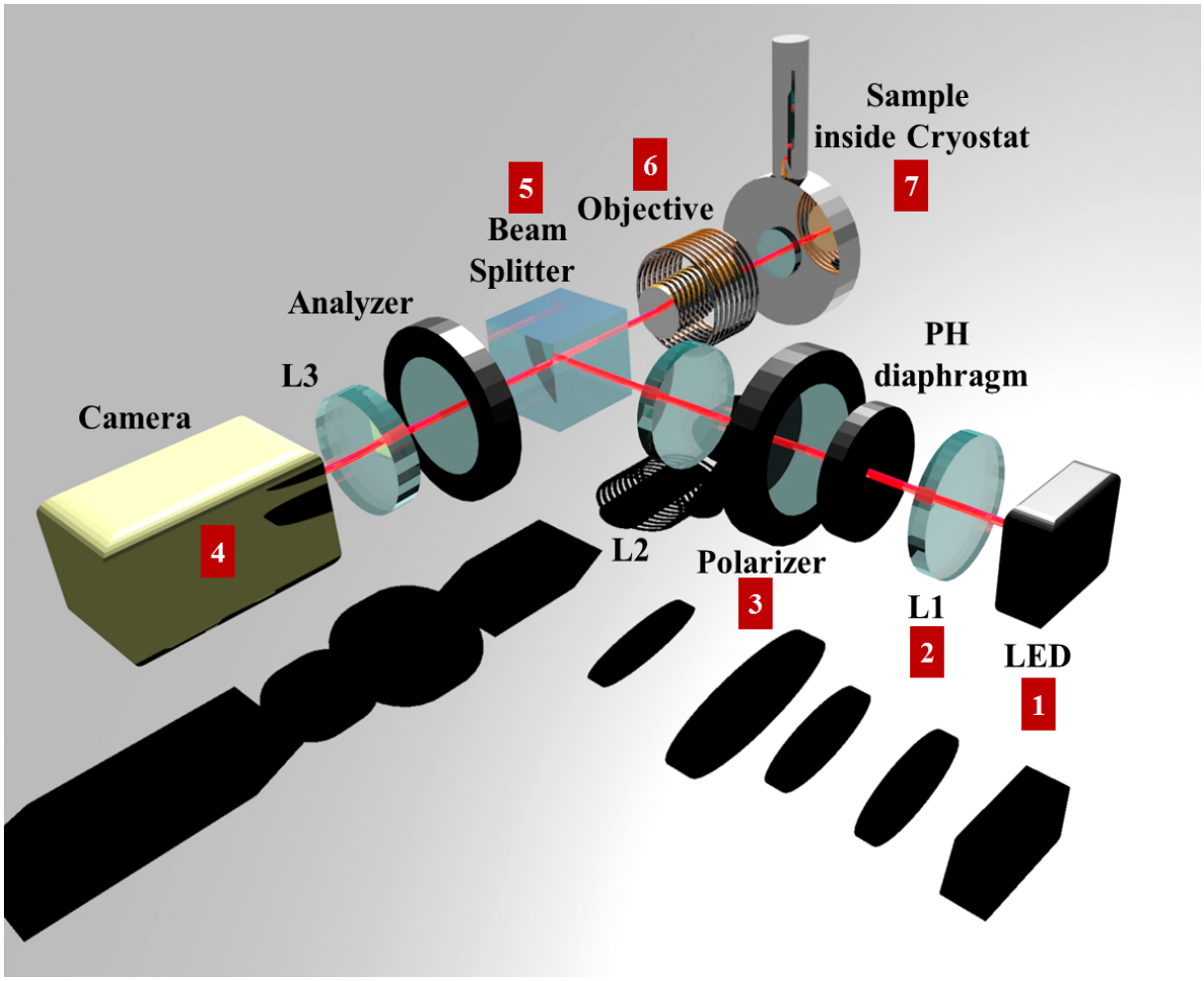

Figure 3.2: **Experimental setup.** Description of the components of microscope.

In figure 3.2 we show a schematic representation of our experimental setup. In the set up, the monochromatic light produced by a LED (see figure 3.2 (1)) passes through a converging lens L1 (2) that collects the maximum amount of light, then through a linear polarizer (3). Next, the beam goes through a second lens L2 which is used to focus the beam into the focal plane of the objective (6). Therefore, the transmitted beam is parallel, which produces an homogeneous lightning of the sample. The pinhole (PH) diaphragm is in the same conjugated plane as the sample. In this way we can control the field of view. Since it is placed in the parallel beam, the diaphragm also controls the light received by the sample. The light reflected by the sample passes through the objective, the analyzer and it is focused into the camera by a third lens L3. We can add a Bertrand lens between the analyzer and the beam splitter in order to focus the illumination plane. This allows to control the illumination in the back focal plane of the objective [43].

We now describe the technical details of each element in our setup and its main characteristics.

1. For the light source we use LED light source at $\sim$ 630 nm controlled and stabilized by a DC power supply CLES 60-3. This allows a stable light intensity and emission in time. For the (Ga,Mn)(As,P), the red light corresponds to the maximum contrast [25]. A good Kerr contrast is also obtained for Pt/Co/Pt.

2. Focalizing lens. L1, L2 and L3 have focal distances of 7, 25 and 30 cm, respectively.

3. Polarizer and analyzer. The polarizers used are Glan-Taylor CasixPGT515.

4. CMOS camera. We used a ORCA-Flash Digital complementary metal-oxide semiconductor (CMOS) Camera C11440 V2. In the CMOS camera, the image sensor is cooled down by a Peltier element to reduce the dark current. It has 6.5 μm $\times$ 6.5 μm pixel sizes. It is possible to make both low noise and high speed readout (100 frames/s with 2048 $\times$ 2048 pixels). For our experiments we use two different operation modes: the free running mode, for which the exposure and readout timing are controlled by the microprocessor and a set of preset parameters; and the external trigger mode, where the exposure and readout timing are controlled by an external trigger.

5. Beam splitter. The optical axes of the calcite crystals are aligned parallel to the plane of reflection. As a result, the s-polarized light is reflected and the p-polarized light is transmitted.

6. Objective. We use two different achromatical objectives with magnification $\times$5 and $\times$20 Olympus LM Plan F1. The $\times$5 objective has a numerical aperture of 0.13 mm and an optimal working distance of 22.5 mm and the $\times$20 has a numerical aperture of 0.4 mm and an optimal working distance of 12 mm. They have a maximum field of view of 5.3 mm and 1.1 mm respectively.

7. Cryostat. We use an open-cycle gas flow optical cryostat KONTI-Cryovac-Micro. The sample is placed inside the cryostat against a cold finger. For low temperature measurements we used helium (down to $\sim 4K$) or nitrogen (down to $\sim 80K$)

   To achieve $\sim 10^{-5} - 10^{-6}$ *mbar* as insulator vacuum, we have used a *Edwards* TIC pumping station turbo pump.

   In order to control the temperature of the cold finger inside the cryostat, we used a proportional-integral-derivative (PID) temperature controller system.

8. Large coil. A large coil generating a magnetic field in the direction of the optical axis was placed in front of the sample. The generated magnetic field is 2.62 mT for 1 A of applied current.

9. Microcoils. The microcoils used through the thesis are typically made of 60-100 turns of 100 μm wire. Their interior diameter is $\sim$ 1.0mm. Their resistance is between 2.5-3.0 Ω and rise times between 200-500 ns.

For field driven velocity measurements (performed with the Pt/Co/Pt ultrathin films and the 12 nm, 50 nm and 80nm thick (Ga,Mn)As samples discussed in chapters 4 and 5), the

samples were glued on the cold finger using silver paint. For (Ga,Mn)As, the microcoil was fixed on the sample using GE7031 varnish. In order to avoid any damage of the Pt/Co/Pt film, the coil was fixed in the proximity using a plastic holder made in a 3D printer.

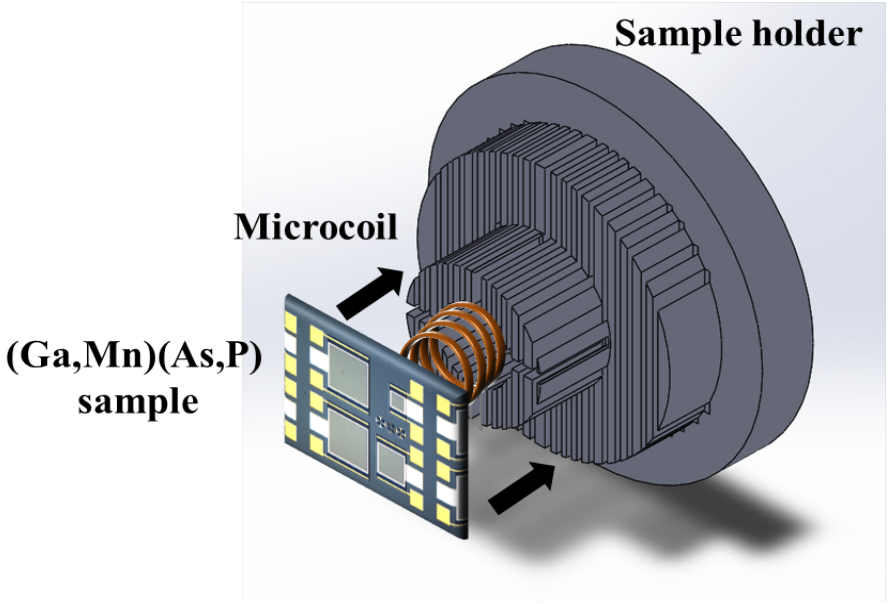

Figure 3.3: **Cold finger (sample holder) designed for simultaneous field and current studies.** To avoid any contact between the wire injecting the current and the magnetic field microcoil, the latter had to be placed in the cold finger below the sample. The cold finger was sliced in order to reduce heating due to eddy current.

For current and field measurements performed with the 4 nm thick (Ga,Mn)(As,P) sample (see chapter 6), the microcoil was placed inside the cold finger under the sample to avoid contact with the micro bonding used to inject current. Figure 3.3 shows the sample holder or cold finger. It contains a hole in the middle that is large enough to place the microcoil. The sample holder was sliced in order to reduce the eddy current generated by the magnetic field variations.

Figure 3.4 shows a comparison of the current pulse proportional to the magnetic field, for a microcoil inside and outside of the hole of a sliced cold finger. We found that the rise time increases $\sim 10\%$ and the current amplitude decreases $\sim 5\%$ when the microcoil is placed inside the cold finger. This is caused by the generation of eddy current. Moreover, as it is observed in figure 3.4, after 3 μs, the amplitude continues to increase. This is due to the long relaxation time of the eddy current. After $\sim 60\mu s$ the voltage amplitude measured for the microcoil outside and inside the sample holder is the same. For the calibration of magnetic field these characteristics were taken into account.

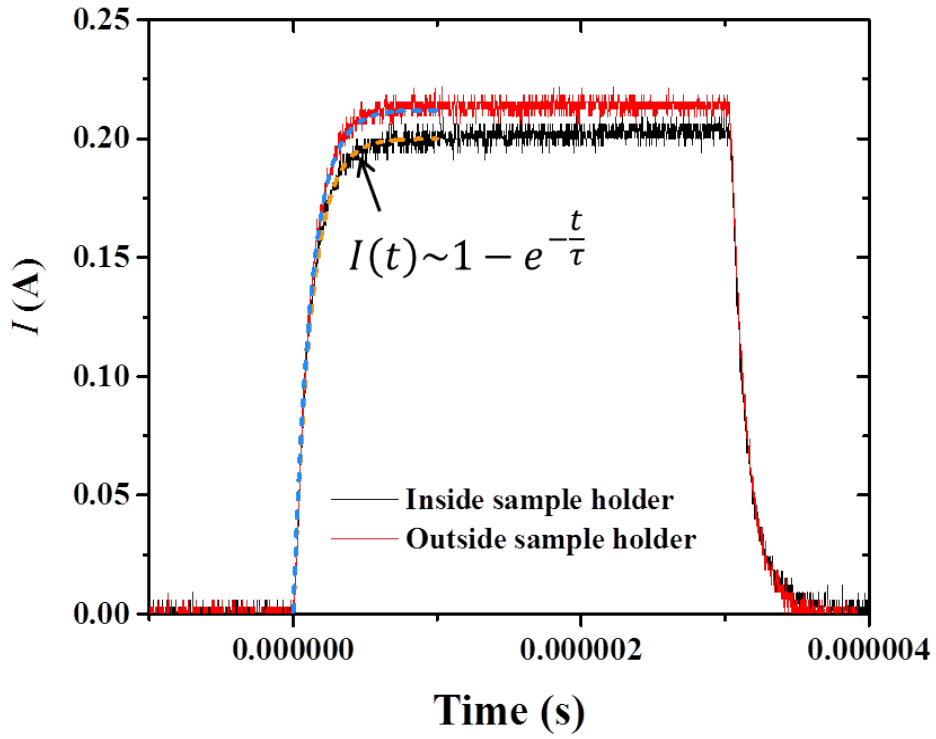

Figure 3.4: **Comparison of the current pulse in a microcoil placed inside and outside of the cold finger.** The current is proportional to the magnetic field. Its magnitude is smaller when the microcoil is set inside the sample holder (black curve) than when it is placed outside (red curve). This is due to eddy currents in the sample holder. The blue and yellow dashed lines are fits used to obtain the rise time τ. After $3\mu s$ the eddy current induced in the sample holder is not yet damped.

3.2 Samples

We used two different kind of samples: a metallic Pt/Co/Pt ultrathin film and ferromagnetic semiconducting (Ga,Mn)(As,P) films with different thicknesses. Their main characteristics are described in the following subsections.

3.2.1 Ultrathin Pt/Co/Pt metallic film

The experimental results on the depinning transition were obtained with a sputter grown ultra-thin film of Pt(3.5nm)/Co(0.45nm)/Pt(4.5nm) deposited on a Si/SiO_2 substrate. The sample was synthesized by B. Rodmacq at Spintec laboratory. It has a Curie temperature $T_C = 415°C$, a saturation magnetization $M_S = 910 \pm 10\%\ kAm^{-1}$. Out of plane PMOKE

and SQUID hysteresis loops were used to determine the sample's saturation magnetization. First and second order effective perpendicular anisotropy fields were determined using polar magneto-optic Kerr effect (PMOKE) anisotropy measurements. To estimate the wall width, these two fields where integrated into a total effective anisotropy field. The effective anisotropy field is $H_{eff} = 0.71T$ and the domain wall width is $\Delta = 6.2nm$. The damping parameter $\alpha = 0.27 \pm 20\%$was obtained from the slope of the precessional flow regime and compared with similar samples. Other properties of this sample are reported by Metaxas *et al.* [73].

3.2.2 Ferromagnetic semiconducting (Ga,Mn)(As,P) films

The experiments discussed in chapter 4 were performed with (Ga,Mn)(As,P) films of thickness 12.5 and 50 nm grown by A. Lemaître at the C2N (CNRS), and a (Ga,Mn)As 80 nm film grown by W. Schoch at the Ulm University and lent respectively by L. Thevenard (INSP, CNRS). All of them were presenting an perpendicular magnetic anisotropy. The films were grown by molecular beam epitaxy. The (Ga,Mn)(As,P) was directly deposited onto a GaAs (001) buffer. For (Ga,Mn)As, a (Ga,In)As interlayer was used to ensure an perpendicular magnetic anisotropy. After annealing, the Curie temperature of the films were 74, 130, and 126 K, respectively [68].

The sample used for current induced DW dynamics in chapter 6 is shown in figure 3.5. It relies on a 4 nm thick (Ga,Mn)As/(Ga,Mn)(As,P) bilayer grown on a (001) GaAs/AlAs buffer and covered by a GaAs cap. The bilayer and the GaAs cap were grown at $\sim 220°C$. The rest of the structure at $\sim 550°C$ [82]. A post-growth annealing was performed to remove interstitial Mn ions. After the annealing the Curie temperature of the films is $T_C \approx 65K$The stack was then patterned by lithography in a set of rectangles with three different sizes: 133 x 210, 228 x 302, and 323 x 399 μm^2. An insulating 55 nm thick SiO_2 gate-oxide layer was deposited by plasma-enhanced chemical vapor deposition at $200°C$. Then it was covered by an evaporated film of Ti/Au serving as the gate (see Fig. 3.5 (B)).

For the experiments presented in chapter 6, this gate was not connected. The motion of domain walls in the bilayer was observed through the square part of the Ti/Au gate which has the smallest thickness. Finally, Ti (20 nm)/Au (200 nm) electrode bars of width 40 μm were deposited onto the GaAs cap on both sides of the rectangle to connect the ferromagnetic (Ga,Mn)As/(Ga,Mn)(As,P) bilayer. Those electrodes were used to generate an homogeneous current density along the direction of the largest side of rectangles.

3.3 Domain wall velocity and roughness measurement.

In this section we describe the procedure used to generate magnetic domains in the samples and to induce motion of domain walls. Then, we discuss the measurement of DW velocity

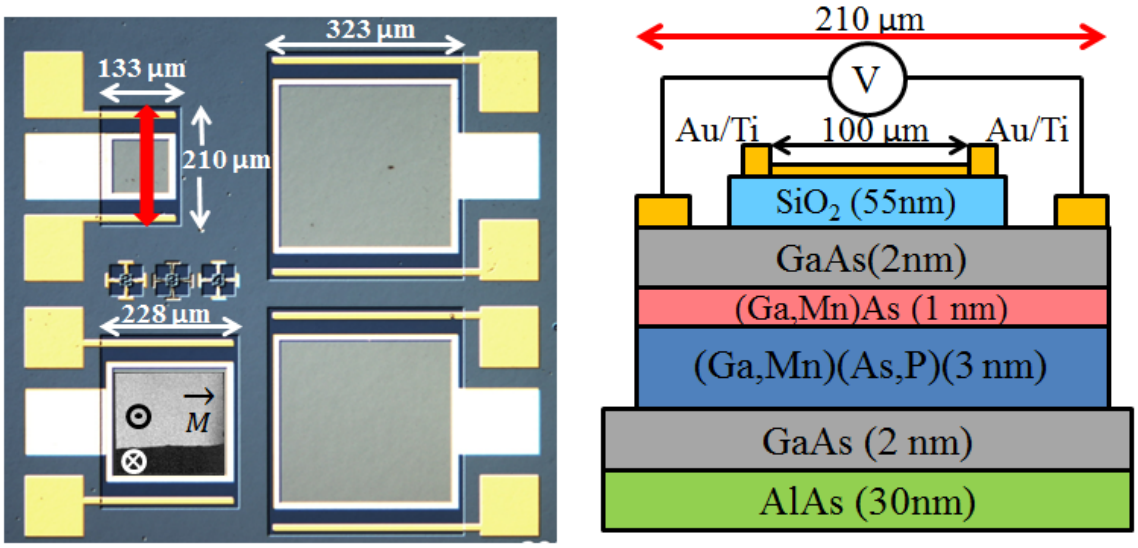

Figure 3.5: **Optical image and schematic drawing of the (Ga,Mn)(As,P) sample used to study current induced DW motion.** (A) Optical image of a set of devices showing the rectangular (Ga,Mn)As/(Ga,Mn)(As,P) bilayer of three different sizes, the connecting Ti/Au electrodes (in yellow) used to generate current pulses and an example of the location were domain wall motion is observed. (B) Schematic of the stack in the direction of the red arrow of Fig. (A). The DW motion is observed through a SiO_2 layer and the thinest part of a Au/Ti electrode deposited above. The latter is not connected for the experiments discussed in this thesis.

and roughness.

3.3.1 Field induced domain wall velocity.

The protocol used to measure the domain wall velocity in the Pt/Co/Pt sample is detailed in figure 3.6. In order bring the sample to its saturation magnetization, it first was submitted to a $\sim$ 18 mT magnetic field pulse during $1s$ produced with the large coil ($H > 10mT$). An image recorded after the saturation pulse constitutes the background and can be used to enhance the contrast.

Then, a magnetic field pulse generated by the microcoil in the opposite direction was used to nucleate small magnetic domains. The DW displacement was produced by magnetic field pulses of fixed amplitude and duration (Δt). Images were recorded after each pulse. The conversion factors are 1 pixel = 0.162 μm for the 20$\times$ objective, and 1 pixel = 0.787 μm for the 5$\times$ objective. The successive images were subtracted to highlight DW displacements ($u(x)$).

In order to make sure that we can define an average DW velocity, which is independent

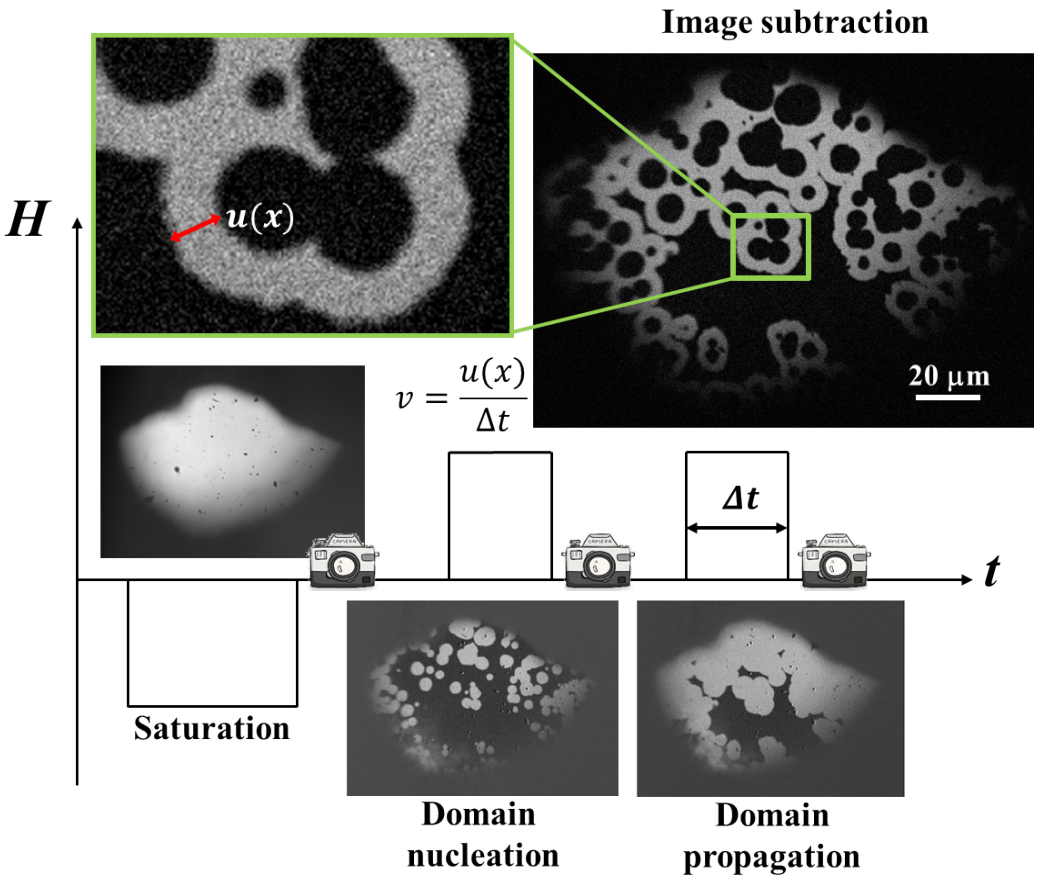

Figure 3.6: **Protocol for DW velocity measurements in the Pt/Co/Pt ultrathin film.** The rectangular steps along the t axis represent the time variation of magnetic field H applied perpendicular to the sample. Here we show a typical example at $T = 225K$ First, the magnetization of the film is saturated using a "negative" magnetic field. Next, we apply a short "positive" pulse to nucleate magnetic domains with opposite magnetization direction and record an image of the domains. Finally we apply a field pulse and record an image when the pulse is finished ($\Delta t = 1\mu s$ and $H \sim 100mT$ in the example shown here). We then subtract the last two images taken and measure the displacement $u(x)$ like it is shown in the inset. We define the velocity as the ratio between the displacement and the pulse duration $v = \frac{u(x)}{\Delta t}$.

of the rise time of the microcoil, displacements were recorded for different pulse duration and magnitude, as shown in figure 3.7. The velocity v corresponds to the slope of the linear part of the plot $u(x)$ *vs* Δt. Once we obtained the DW velocity v as a function of magnetic field H, we smoothed the velocity curve using a rolling average over 5 successive points.

The protocol used to measure the field induced DW velocity in the 12.5, 50 and 80 nm thick (Ga, Mn)(As,P) films is identical to the one described for the Pt/Co/Pt ultrathin film except for the chosen temperature range, which is limited by the sample's T_C. The velocity curves where measured between 6 and 96 K.

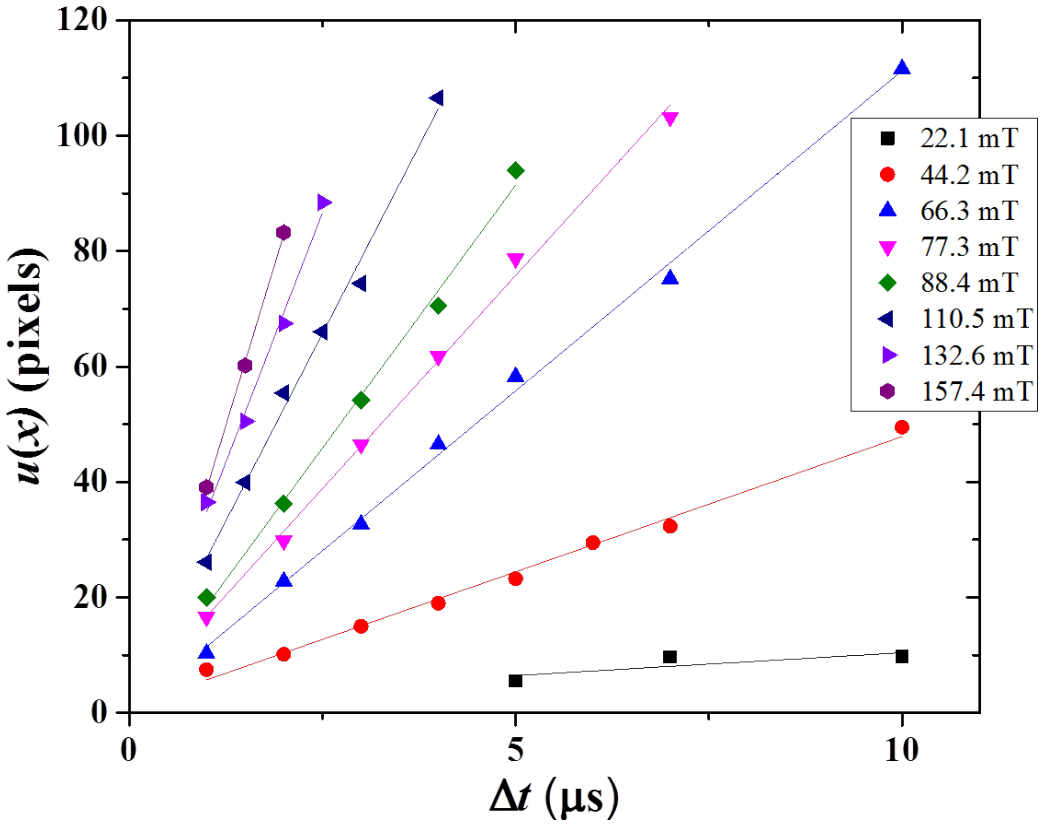

Figure 3.7: **Protocol used for DW velocity measurements in the Pt/Co/Pt ultrathin film.** We measure the DW displacement for different magnetic fields H. The straight lines are the best linear fits for each magnetic field and its slope is the obtained DW velocity.

For the 4 nm thick (Ga,Mn)(As,P) film study reported in chapter 6, we use a similar protocol. The only difference is that we nucleated a single, almost straight domain wall instead of several, as illustrated in figure 3.8 (B). The protocol to generate one straight DW is the following: we apply a "negative" pulse with the large coil to saturate the magnetization. Next, we apply simultaneously a short ("positive") field and current pulse. The amplitude and pulse duration of those pulses are chosen empirically, and depend on the temperature. For instance for $T = 55$K we apply a simultaneous $2\mu s$ pulse of 3.5 mT and 7.9 GA/m^2. Then we apply simultaneous short pulses of field and current until the DW reaches the chosen location in the sample.

The shape of the domains nucleated in the 4 nm thick (Ga, Mn)(As,P) film is different when we nucleate a magnetic domain by applying only field pulses and when we apply a combination of current and field pulses due to the geometry of the golden electrodes through which the current flows into the sample in a certain direction and the combined effect of the field and current. In figure 3.8 we show two different ways to nucleate magnetic domains in the same sample at $T \sim 25K$. In 3.8 (A) we nucleate oval domains applying only a

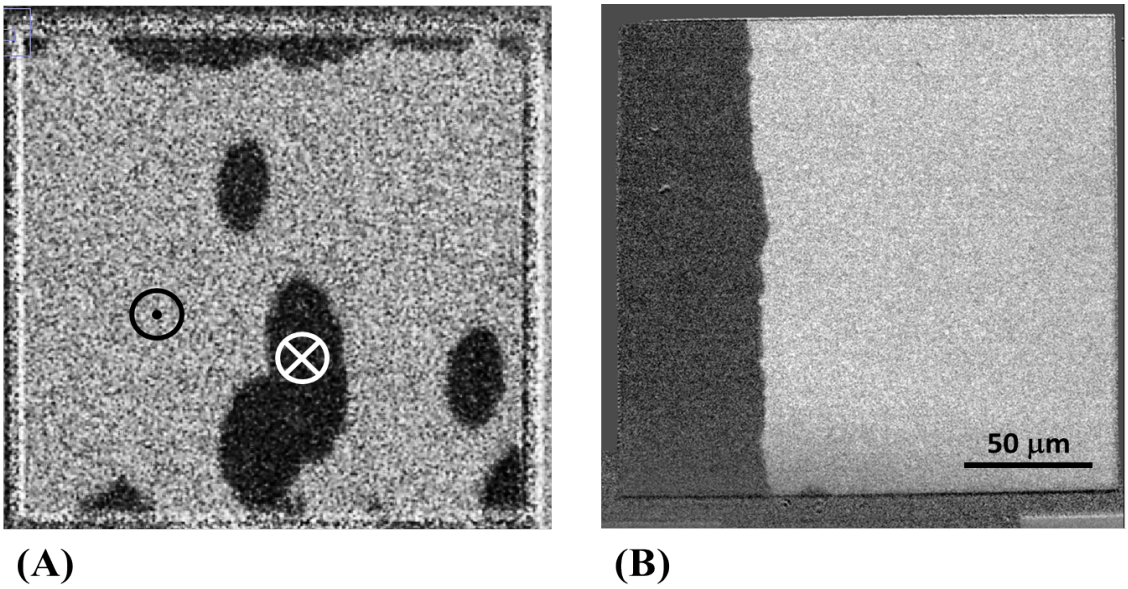

Figure 3.8: **Different magnetic domain nucleation processes in a 4 nm thcik (Ga,Mn)(As,P) film.** We show two different magnetic domain nucleation processes in a 4 nm (Ga,Mn)(As,P) film. (A) Nucleation produced only by a $\sim 10mT$ field pulse of with a $20\mu s$ duration at $T = 25K$. (B) Nucleation produced by a combination of simultaneous field and current pulses at $T = 24K$. ($J = 9.7GA/m^2$, $H = 5mT$ and $\Delta t_H = \Delta t_J = 2\mu s$).

magnetic field pulse ($\sim 10mT$, $\Delta t = 20\mu s$). In 3.8 (B), we produce a unique flat DW with a combination of simultaneous field and current pulses ($J = 9.7GA/m^2$, $H = 5mT$ and $\Delta t_H = \Delta t_J = 2\mu s$).

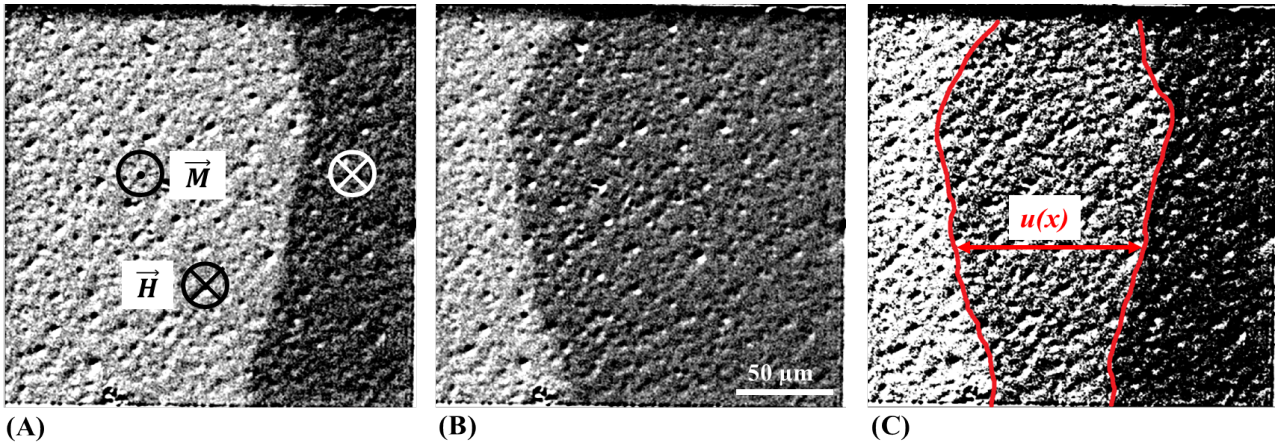

Figure 3.9: **Measurement of DW displacement for (Ga,Mn)(As,P) 4nm thick film.** The domain wall velocity was deduced from the average value $\langle u(x) \rangle$ of the whole DW displacements as indicated in (C).

The velocity was deduced from the mean displacement in the direction of growth as indicated in figure 3.9. With a program written in Python 2.7 we binarized the images by

taking the average between the maximum and minimum intensity recorded in the image. The region with intensity below (above) this average value corresponds to opposite directions of magnetization. The frontier defines the domain wall position. In this way, we can measure the DW displacement $u(x)$ between consecutive images for each pixel of the DW, and calculate the average value $\langle u(x) \rangle$ for the whole DW. Then we define the velocity as $v = \langle u(x) \rangle / \Delta t$, where Δt is the field pulse duration. For current induced DW motion we used the same protocol.

3.3.2 Current induced domain wall velocity measurements

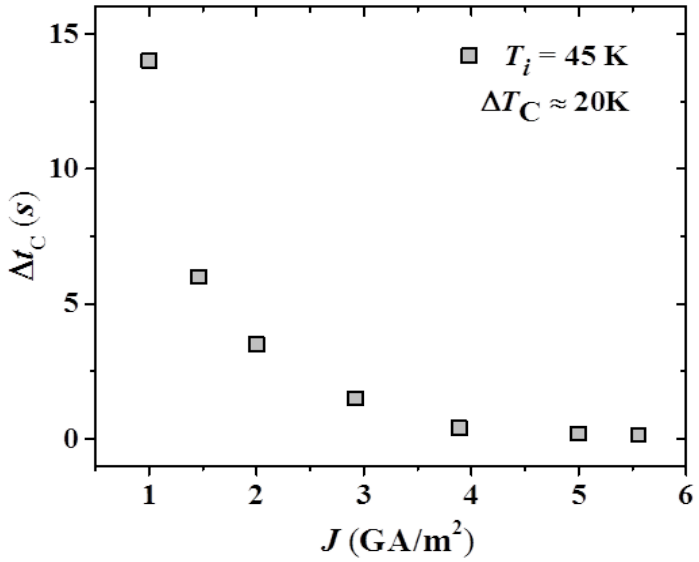

Figure 3.10: **Critical time t_C to reach T_C for different current densities J.** For a fixed initial temperature $T_i = 45K$ we obtain the critical pulse duration Δt_C needed to heat the sample until T_C is reached. This critical time is measured for different current densities.

The flow of an electric current in the (Ga,As)/(Ga,Mn)(As,P) bilayer produces Joule heating. Since the temperature gradients may affect the magnetic properties of ferromagnets and they contribute to magnetization reversal, we have to analyze the contribution of Joule heating to DW motion.

In order to estimate the temperature rise due to Joule heating, we used a procedure similar to one proposed by Curiale *et al.* [19]. For each measurement, we prepare an initial magnetic state consisting in a domain surrounded by an homogeneous reversed magnetization. First, we determine the critical (Curie) temperature at which the contrast of polar Magneto-Optical Kerr effect vanishes ($T_C \approx 65K$) by increasing progressively the temperature. The experimental protocol used to measure the temperature rise is the following one:

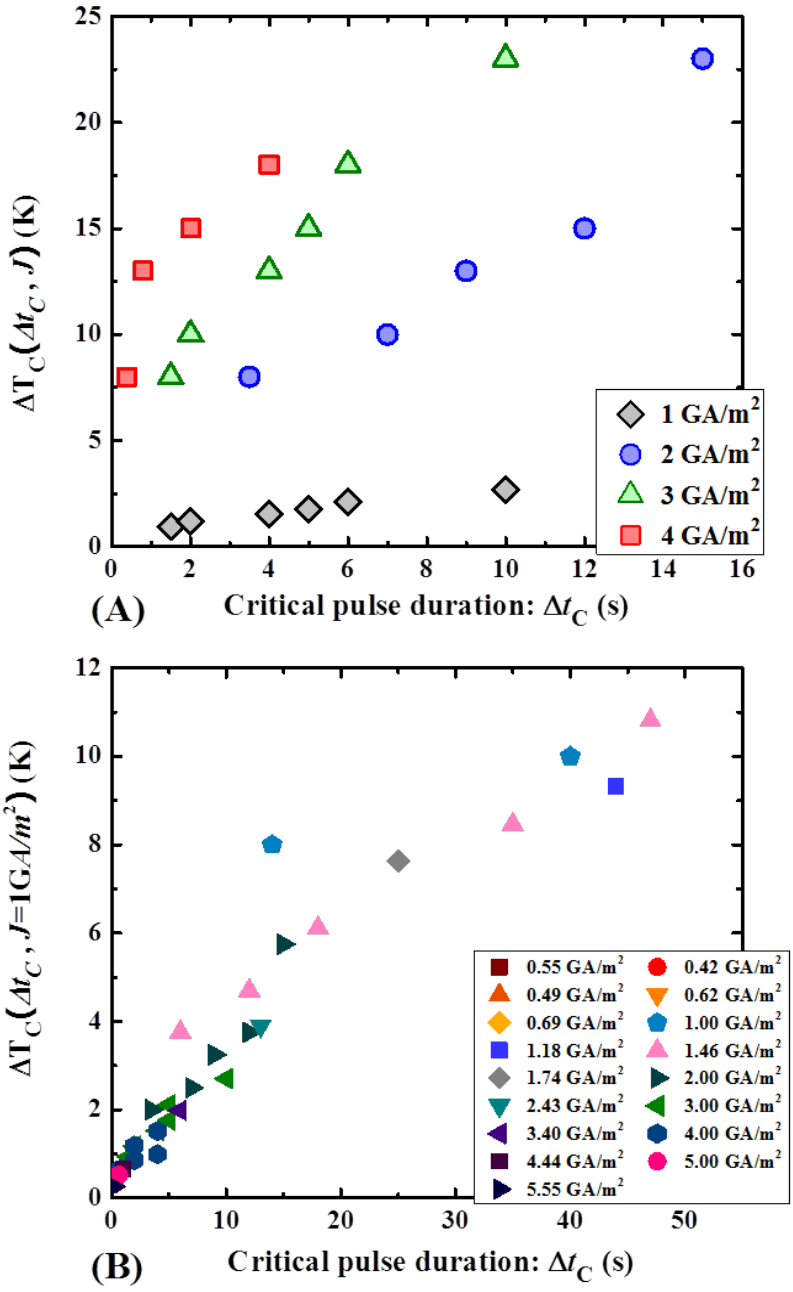

Figure 3.11: **Temperature rise produced by Joule heating.** (A) Temperature rise ΔT_C in a $228 \times 302\ \mu m^2$ device produced by current pulses of different magnitude J (as indicated in the legend) *vs* pulse duration Δt_C. (B) Temperature rise $\Delta T_C(\Delta t_c, J)$ divided by J^2 and normalized to $J = 1GA/m^2$.The current density is relatively low so it takes longer pulse durations to reach T_C in comparison with similar experiments in (Ga,Mn)(As,P) tracks for example [19].

1. We set an initial sample temperature T_i which determines the temperature rise ΔT_C required to reach T_C, i.e. $\Delta T_C = T_C - T_i$.

2. We choose a given current density J and a given pulse duration Δt which induces a temperature increase $\Delta T(J, \Delta t)$ that depends on the current density J and on the duration of the applied current pulse Δt. If $\Delta T(J, \Delta t) < \Delta T_C$ the magnetic domains are still be visible after the we apply the pulse, i.e. the sample has remained in a ferromagnetic state during the pulse. If $\Delta T(J, \Delta t) > \Delta T_C$, the magnetic domains are no longer visible after the pulse is applied: the Joule heating has produced a transition between ferro- and paramagnetic state.

3. For a fixed current density J, we estimate the critical pulse duration Δt_C at which $\Delta T(J, \Delta t_C) = \Delta T_C$ by progressively increasing the pulse duration Δt until the domain vanishes.

4. We repeat the last two steps for a different current densities J. What we obtain obtain the necessary time (the critical pulse duration Δt_C) that a current density should be applied (J) in order to increase the temperature of our sample from the fixed initial temperature T_i to the Curie temperature T_C. A typical example is shown in figure 3.10 where we show the critical current pulse duration Δt_C to reach T_C for different current densities. In this example, the initial fixed temperature is $T_i = 45K$ and therefore $\Delta T_C \approx 20K$.

5. Steps 1 to 4 are repeated for a different initial temperature T_i.

This procedure enables us to associate the necessary time (pulse duration Δt_C) that a current density (J) should be applied to the sample in order to increase the temperature from an initial T_i to T_C, i.e. ($\Delta T(\Delta t_C, J)$). The results are shown in figure 3.11 for different initial temperatures T_i. The temperature rise ΔT_C is found (see figure 3.11 (A)) to increase with increasing current density.

For a given current pulse, the temperature rise ΔT should be proportional [19] to the power produced by Joule heating per unit time and volume:

$$\frac{dP}{dV} = \rho J^2, \tag{3.1}$$

where ρ is the resistivity. In order to verify the compatibility of our results with Joule heating, we have divided the measured ΔT_C (see figure 3.11 (A)) by J^2, in order to renormalize the data. The results are reported on figure 3.11 (B). As we can observe, the data points collapse in one single curve, thus confirming the signature of Joule heating.

In order to check that the disappearance of the magnetic domain is not due to a fast DW motion induced by the current, we performed a similar temperature rise measurement on a device located $\sim 1mm$ away from the one where current was injected. In this case, the heat is transfered through the substrate. The results are shown in figure 3.12. The curve

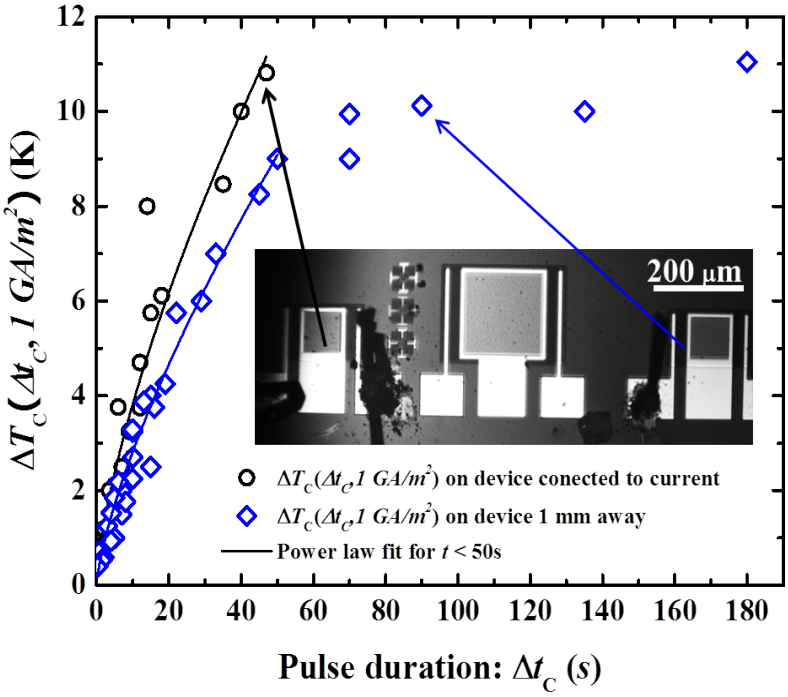

Figure 3.12: **Normalized temperature rise produced by Joule heating.** Normalized temperature rise $\Delta T_C(\Delta t_c, J = 1GA/m^2)$ *vs* pulse duration Δt_C measured for a 228 × 302 μm^2 device connected to current source (circles) and located $\sim 1mm$ away (diamonds). The solid blue and black lines are the best fit of the function $\Delta T(\Delta t, 1GA/m^2) = a(\Delta t_C)^b$ for $t < 50s$. Inset: Optical image of the devices.

$\Delta T_C(\Delta t_C, 1GA/m^2)$ *vs* Δt_C is very similar as the one obtained for device with the current. This confirms that the disappearance of the magnetic domain is due to Joule heating.

As it can be observed in figure 3.12, the temperature rise presents a strong variation for short durations ($t < 50s$). For longer duration ($t > 50s$), the temperature tends to saturate, which suggests that a quasi-thermal equilibrium has been achieved between the Joule power produced by the current, the cooling power and the temperature regulation of the cryostat.

Let us now discuss the contribution of Joule heating to domain wall dynamics. For short current pulses ($\Delta t < 50s$) used in the DW dynamics study, the contribution of Joule heating can be easily estimated. The normalized temperature rise can be accurately fitted by an empirical function:

$$\Delta T(\Delta t, J = 1GA/m^2) = a(\Delta t)^b, \tag{3.2}$$

with $a = 0.78 \pm 0.13$ and $b = 0.69 \pm 0.05$. Since the Joule effect is proportional to the square of the current density, we can therefore write:

$$\Delta T(\Delta t, J) = J^2 \Delta T(\Delta t, J = 1GA/m^2) = aJ^2(\Delta t)^b \tag{3.3}$$

and calculate ΔT for any current pulse amplitude and duration. For the whole set of pulses used to measure DW velocity in chapter 6, the maximum temperature rise we find is $\Delta T \leq 0.3K$. The corresponding velocity variation is $\frac{v(J,T)-v(J,T+0.3K)}{v(J,T)} \approx 3\%$. As this is smaller than the typical error bars for the measurement of DW velocity, the Joule heating can be neglected.

3.3.3 Correlation function and estimation of the roughness exponent

In this section we detail the procedure followed for the statistical study of DW roughness. The roughness exponents for magnetic field (ζ_H) and current (ζ_J) driven DW motion were determined systematically from consecutive images of DW displacements separated by a constant time step Δt as illustrated in figure 3.13.

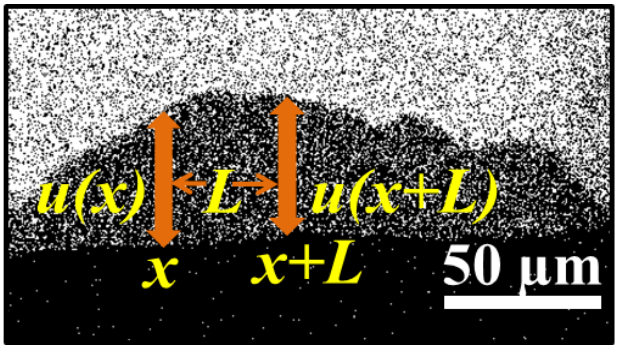

Figure 3.13: **DW displacement.** Schematics of the displacements $u(x)$ and $u(x+L)$ of two DW positions separated by a distance L, which are used to calculate the displacement-displacement correlation function. The darker part of the image shows initial DW position, the middle gray is the region covered by the DW during its motion in a time step Δt.

For each position x along the initial DW we compute the displacement-displacement correlation function: $w(L) = \langle [u(x) - u(x+L)]^2 \rangle$ for $\sim 1\mu m < L < R$, where L is the length of an arbitrary segment and R is the length of the whole DW. The terms $u(x)$ and $u(x+L)$ are the displacement of DW at positions x and $x+L$ respectively after the field or current was applied during $\Delta t =$ (typically Δt is equal to 1.0 or 0.5s). We choose $u(x)$ and $u(x+L)$ as the closest positions between x and $x+L$ and the subsequent DW.

The next step is plotting $\log(w(L))$ *vs* L as the example shown in figure 3.14. We obtain the plot with a code written in Python 2.7.

In order to obtain a value of the roughness exponent, we follow the next procedure: we consider the region of the plot $\log(w(L))$ *vs* L where a linear behavior is observed, $(1\mu m < L \lesssim 10 - 15\mu m)$ as it is illustrated in figure 3.14. Below this value there is correlation present in the DW. The upper limit of the linear fit is determined by the offset of the divergence between the linear behavior and the experimental data. We calculate the mean square weighted deviation χ^2 between the liner fit and the experimental data, when

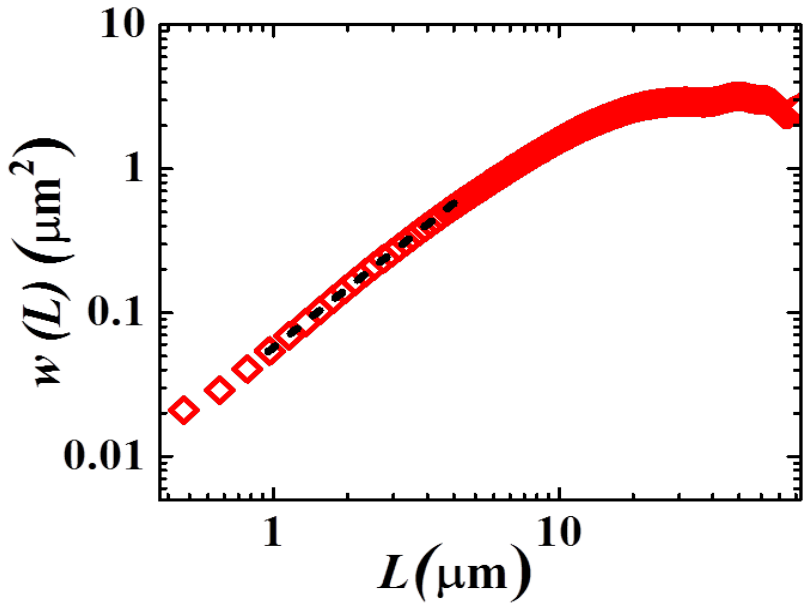

Figure 3.14: **Typical displacement-displacement correlation function.** Example of a $w(L)$ *vs* L plot in log-log scale for current driven DW motion at $T = 14K$. In order to determine the roughness exponent ζ, we fit a line (see the dashed line) up to the limit where the behavior is no longer linear. The slope corresponds to 2ζ.

$\chi^2 \gtrsim 10\%$ of the slope value $m = 2\zeta$ we stop the linear fit. It is an arbitrary criterion, however, we use it consistently through the roughness exponent measurement in all our data. This fit is done with the software Origin2015 (64bit)Sr1. We recall that according to Eq. 2.25, the slope of this linear part, is two times the roughness exponent, ζ.

For the exploration of the time variation of the roughness, we made movies of the DW displacement for constant field or current values. We have repeated the same procedure for each time step Δt. As discussed in chapter 6, we could evidence a transient creep regime and verify that for a steady motion, the exponent ζ remains constant.

3.4 Chapter summary

In this chapter we described the experimental setup used to study the magnetic domain wall dynamics. We described in detail the Kerr microscope, along with the coils used to generate the magnetic field, and the cryostat used to control the temperature. This setup allowed us to observe the motion of magnetic domain walls in two different kind of sam-

ples with perpendicular anisotropy: a Pt/Co/Pt metallic ultra thin film and ferromagnetic semiconducting (Ga,Mn)(As,P) films with different thicknesses.

We obtained information of the magnetic domain shape, velocity and geometry under the effects of magnetic field and electric current varying in a wide range of amplitudes and time duration. In the last section of this chapter we explained in detail the procedure to systematically process this information from the images stored with the CCD camera: we established protocols to measure the DW velocity from the subtraction of consecutive images obtained after field or current pulses were applied to the sample.

In the case of current pulses, we quantified the temperature rise due to Joule effect. For the current amplitudes and pulse duration used in our experiments, the temperature fluctuations were found to be negligible.

We developed a Python code to compute the correlation function $w(L)$ and to extract the roughness exponent ζ. We performed a time resolved analysis of the roughness exponent.

CHAPTER 4

Depinning transition

"Owl explained about pinning and creep. He had explained this to Pooh and Christopher Robin once before, and had been waiting ever since for a chance to do it again, because it is a thing you can easily explain twice before anybody knows what you are talking about."

A. A. Milne . Winnie the Pooh (Adapted by G. Blatter *et al.*)

In this chapter we present a quantitative and comparative study of magnetic-field-driven domain wall (DW) depinning transition in ultrathin ferromagnetic films made of different materials over a wide range of temperature.

At sufficiently low drive f, the competition between elasticity, weak random pinning and thermal fluctuations results in the creep motion over effective pinning barriers. In this dynamical regime, the velocity follows an Arrhenius law. Close to zero drive ($f \to 0$), the phenomenological scaling theory [7, 81] and functional renormalization group [14] calculations for an elastic line moving in a random pinning disorder, predict that effective pinning barriers present universal power-law variations. This has been observed in experimental systems as well [70, 44]. It has been well established that the whole thermally activated creep regime can be universal, and controlled by a unique pinning energy barrier function [51]. On the other hand at sufficiently large drives, the DW velocity follows a linear behavior

that characterizes the flow regime.

Between the creep and the flow regimes, at the depinning transition, it has been shown that at low temperature limits, the velocity follows a critical power-law behavior [39, 74, 36]. In experimental works the shape of the depinning transition has been observed and seems to be compatible with the power law that predicts the velocity to behave like $v \sim T^{\psi}$ [73, 51]. Similar behavior is expected also for other physical systems such as random-field Ising model [93], and charge density waves models [74].

Some of the open questions regarding the depinning transition are listed next. Does the depinning transition of DWs in ferromagnetic ultrathin films present universal behaviors? Theoretical predictions suggest that at the depinning transition the domain wall velocity presents two asymptotic behaviors, one at $T \to 0$ where $v(H, T = 0) \sim (H - H_d)^{\beta}$ and the other at the depinning threshold $v(H = H_d) \sim T^{\psi}$. Is the DW dynamics compatible with these asymptotic behaviors? and, can we characterize the depinning transition beyond the asymptotic behavior? What are the links between the creep and the depinning regime? How is the crossover between the depinning transition and the flow regime?

More technically, can we determine the depinning threshold when applied field and thermal effects are present? How can the universal behavior be distinguished from non-universal behavior?

From the experimental point of view it has been challenging to go beyond critical exponent analysis [87, 53, 16] due to the characteristics of the velocity when there are thermal effects present [10, 11]. This complicates a straightforward determination of the depinning threshold and the distinction between material-dependent and universal behaviors.

In order to address these questions we study the motion of domain walls (DW) driven by magnetic field in an Pt/Co/Pt ultrathin film with perpendicular anisotropy [73, 44] in a wide range of temperatures [4.4 - 300 K] and compare them to results published in the literature for Au/Co/Au [60] and Ta/CoFeB/MgO [9] ultrathin films, which presents different strengths of pinning disorder.

4.1 Domain Wall dynamics

Here, we propose a phenomenological description of the observed DW dynamics at different temperatures in a Pt(3.5nm)/Co(0.45nm)/Pt(4.5nm) film. We analyze the creep regime in order to deduce the depinning threshold $H_d(T)$ and other material dependent parameters: $v(H_d(T))$, $v_d(T)$ and $T_d(T)$.

In figure 4.1 (A), we show the DW velocity v as a function of applied magnetic field H for different temperatures in the range 4.4 to 300 K. For every one of them we observe an inflection point $(H_d(T), v(H_d(T)))$ indicated by solid diamonds that separate the low drive

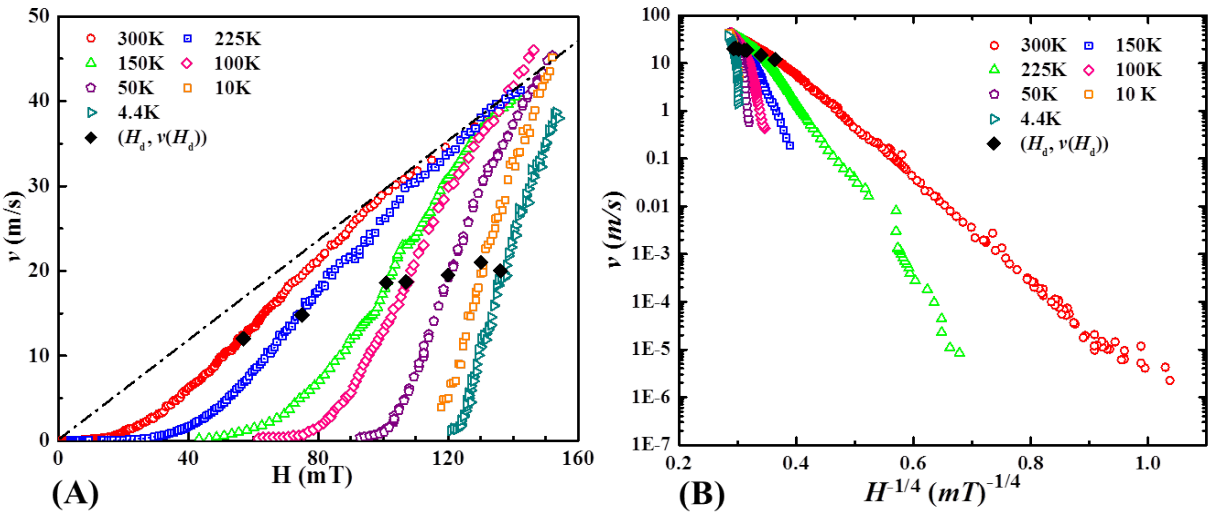

Figure 4.1: **Domain wall dynamics.** (A) DW velocity v in Pt/Co/Pt *vs* field H measured for different temperatures. The inflection points $(H_d(T), v(H_d(T)))$ are indicated by solid diamonds. (B) DW velocity v *vs* $H^{-1/4}$ in semi-log plot. The solid diamonds indicate the coordinates of the inflection points in the linear scale.

creep regime ($H < H_d$) from the depinning regime. The linear variation observed at higher drives ($v > 30m/s$) is only reached for the highest temperatures (300 and 225 K). It extends over the magnetic field range of 110-155 mT. The straight dashed line indicated in figure 4.1 (A) extrapolates the flow regime to low drives and has a slope m which corresponds to the mobility. The measured mobility ($m = v/H = 0.29 \pm 0.03 m/smT$) is in good agreement with the reported value [73, 51] for the precessional flow regime in similar samples where the mobility was obtained from the velocity curves as well.

Within the creep regime ($H < H_d$), the DW velocity v increases several orders of magnitude over a narrow applied magnetic field interval as it can be observed in the semi-log scale in the velocity curves in figure 4.1 (B). The shape of the velocity v *vs* $H^{-1/4}$ curves is found to be a straight smooth line within the creep regime for different temperatures in good agreement with previous works [73, 51].

Between the creep and the linear flow regime lies the depinning transition, which covers a narrow range in the field compared with the creep and flow regimes. This regime, until now it has not been easy to delimit and fully characterize. In order to discuss the depinning transition we first analyze quantitatively the creep regime. For that we recall the equation characterizing the creep regime:

$$v(H,T) = v(H_d,T)\exp(-\Delta E/k_B T), \tag{4.1}$$

where the parameters H_d and $v(H_d,T)$ are the coordinates of the upper boundary of the creep regime indicated with diamonds in figures 4.2, and

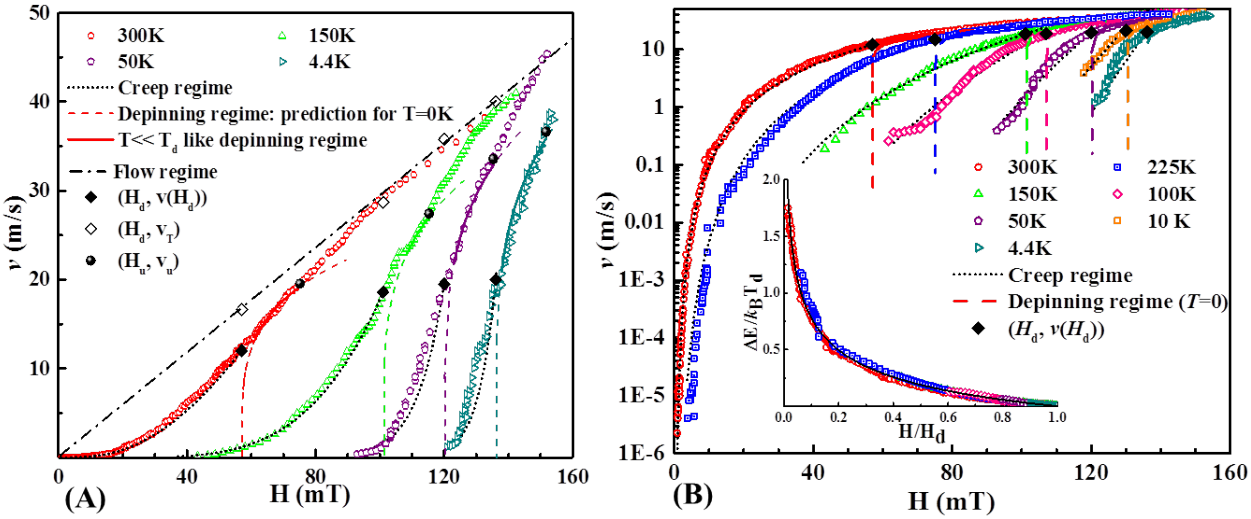

Figure 4.2: **Analysis of domain wall dynamics.** DW velocity in Pt/Co/Pt measured for different temperatures and presented in linear (A) and semilog (B) scales to show the high and low drive regimes, respectively. The fit for the *creep regime* $[0 < H < H_d(T)]$ is shown by the black dotted curves and ends for velocities $v(H_d(T), T)$ indicated by black diamond symbols. The depinning regime extends from the depinning threshold $H = H_d(T)$ to the universality limit $H_u(T)$ (indicated by black solid spheres). The depinning velocities $v_T(H_d(T), T)$ correspond to empty diamonds. The dashed curves are the predictions of equation 4.4 for a unique value of $x_0 = v_T/v_H = 0.65$ and match with part of all velocity curves as indicated by solid segments, here v_H is the prefactor for the $T \to 0$ asymptotic behavior (see Eq. 4.4). The linear flow regime, indicated by a straight dashed-dotted line, is reached for high drives (and only for $T > 50K$). Inset: universal reduced energy barrier as a function of reduced field deduced from velocity curves.

$$\Delta E = k_B T_d \left[\left(\frac{H}{H_d} \right)^{-\mu} - 1 \right], \tag{4.2}$$

is the effective pinning energy barrier. Here, $k_B T_d$ is a characteristic energy that measures the pinning strength. The exponent $\mu = 1/4$ corresponds to the creep exponent for the motion of an elastic line in a 2-dimensional disordered medium.

The parameters $v(H_d(T), T)$, $T_d(T)$ and $H_d(T)$ were determined using the following method:

- Step 1: We assumed the coordinates of the upper boundary of the creep regime $(H_d, v(H_d))$ correspond to the inflection point of the velocity v *vs* field H curves. As discussed in Chapter 2, section 2.2, the curvature is predicted to be positive for the creep regime $(H < H_d)$ and to become negative for the depinning regime $(H > H_d)$.
- Step 2: An estimate of T_d is then deduced from a fit of $v(H)$ with equations 4.1 and

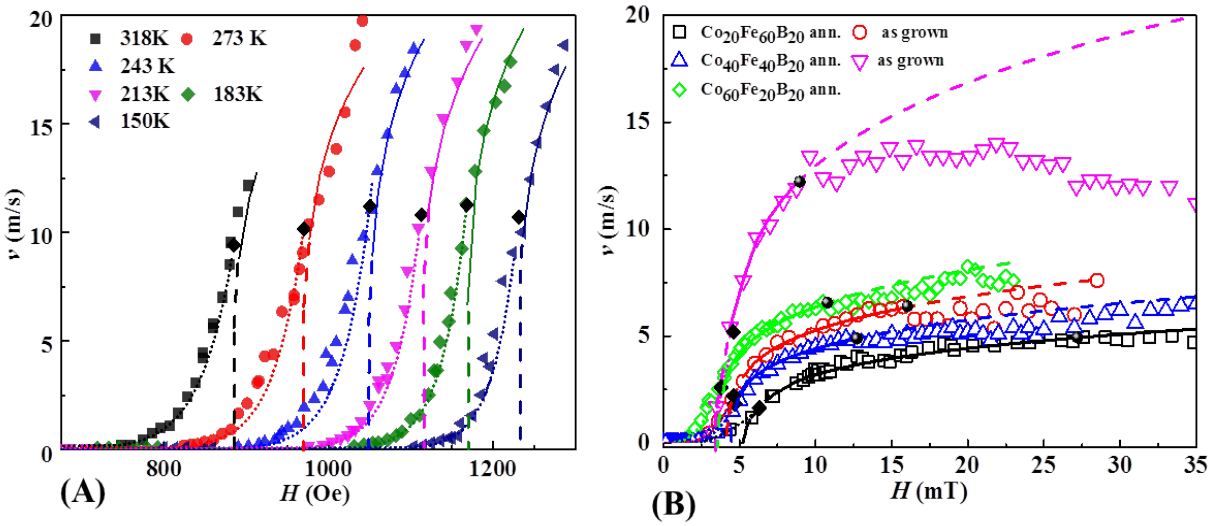

Figure 4.3: **Analysis of DW dynamics for Au/Co/Au and CoFeB.** Domain-wall dynamics observed (A) in Au/Co/Au for different temperatures and (B) in Ta/CoFeB/MgO for different cobalt and iron concentrations and for as-grown (ag) and annealed (an) films. The data are taken from [60] and [9], respectively. The diamond symbols represent the upper boundaries of the creep regime $[H_d(T), v(H_d, T)]$. The black solid spheres correspond to the universality limit $H_u(T)$. The dotted lines are fits for the creep regime. The solid and dashed curves correspond to the $T \to 0$ asymptotic predictions of the depinning transition for $x_0 = 0.65$ and is obtained without adjustable parameter. The solid curve is the range in which the asymptotic behavior agrees with the experimental data.

4.2 over the range $0 < H < H_d$.

- Step 3: In order to improve the accuracy of the estimated H_d and $v(H_d)$ values, we fit equation 4.1 and the effective pinning energy barrier for increasing values of H as shown in figure 4.2 by dotted curves. The upper boundary of the creep regime $(H_d, v(H_d))$ was defined as the set off of the divergence between the data points and the fit of the creep law.

- Steps 2 and 3 were then repeated in order to provide a fine tuning of the values of H_d, $v(H_d)$ and T_d.

In figure 4.2, we show the v *vs* H curves and the fit of equation 4.1 which are in good agreement over the whole creep regime below the depinning field H_d (see figure 4.2 (B)). The coordinates $(H_d(T), v(H_d, T))$ are also indicated with solid diamonds in figure 4.2. The set of temperature-dependent parameters H_d, $v(H_d)$, and T_d are reported in Table 4.1.

In order to verify that the parameters H_d and T_d are compatible with the universal behavior, we plot the reduced energy barrier height $\frac{E}{k_B T_d(T)} = \frac{T}{T_d(T)} \ln\left[\frac{v(H_d(T),T)}{v(H,T)}\right]$, as a function of the reduced force $H/H_d(T)$. In the inset of figure 4.2 (B) we show that this

transformation collapses all the velocity curves onto a single master curve which reflects the universal behavior of the pinning energy barrier [51]. The good agreement of data with the equation 4.2 for $\mu = 1/4$ indicates that the whole creep dynamics indeed belongs to the universality class described by the quenched Edward-Wilkinson equation for an elastic line with short-range elasticity moving in a random-bond short-range correlated microscopic pinning potential [51].

Material	$T(K)$	$T_d(K)$	$H_d(mT)$	$v(H_d)(m/s)$	$v_T(m/s)$	$H_u(mT)$	$v(H_u)(m/s)$
Pt/Co/Pt	4.4	450(100)	136(3)	20.0(1.0)	40.0(1.0)	151(3)	18.5(1)
(0.5 nm)	10	660(70)	130(1)	21.0(2.0)	39.3(1.0)	138(2)	29(1)
	50	2860(150)	120(2)	19.5 (0.5)	35.8(1.0)	133(3)	31(2)
	100	3090(280)	107(2)	18.7 (0.5)	31.3(1.0)	117(2)	27(1)
	150	2700(150)	101(1)	14.8(1.0)	28.7(1.0)	116(2)	27(1)
	225	2750(120)	75(1)	18.6 (1.0)	21.5(1.0)	96(3)	24(1)
	300	2650(20)	57(1)	12.0(1.5)	16.6(1.0)	73(2)	18.5(1)
Au/Co/Au	150	25800(1000)	123.5(1.0)	10.7(0.5)	23.1(1.0)	126.5(0.5)	15.8(0.6)
(1.0 nm)	183	28800(1500)	115.0(1.0)	11.3(0.2)	23.9(1.0)	121.5(0.5)	16.7(0.6)
	213	29400(1500)	110.0(1.0)	10.8(0.2)	22.8(1.0)	116.0(0.5)	16.9(0.6)
	243	29300(1500)	102.5(1.0)	11.2(0.5)	23.0(1.0)	108.5(0.5)	16.5(0.6)
	273	29000(1500)	96.5(1.0)	10.2(0.3)	20.5(1.0)	102.0(0.5)	15.5(0.6)
	318	28400(1500)	88.0(1.0)	9.4(0.1)	18.5(1.0)	90.5(0.5)	12.2(0.6)
$Co_{20}Fe_{60}B_{20}$ an	293	1800(100)	6.6(0.2)	1.6(0.3)	2.4(0.5)	27.0(7.0)	4.9(0.4)
$Co_{20}Fe_{60}B_{20}$ ag		1800(100)	4.8(0.2)	2.2 (0.8)	3.3(0.5)	16.0(3.0)	6.4(0.6)
$Co_{40}Fe_{40}B_{20}$ an		1400(100)	5.0(0.2)	1.9(0.5)	2.8(0.5)	12.6(3.0)	4.9(0.6)
$Co_{40}Fe_{40}B_{20}$ ag		2000(100)	4.3(0.2)	5.2(0.8)	8.1(0.5)	8.9(2.0)	12.2(2.0)
$Co_{60}Fe_{20}B_{20}$ an		2200(100)	3.5(0.5)	2.6(0.4)	3.7(0.5)	10.7(2.0)	6.5(0.5)
(1.0 nm)							

Table 4.1: **Material and temperature dependent parameters.** For each material we show the sample thickness (nm) (written below the sample name), the temperature of the experiment ($T(K)$), the fitted parameters in the following order: depinning temperature ($T_d(K)$), depinning magnetic field ($H_d(mT)$), velocity on the depinning field ($v(H_d)(m/s)$) and depinning velocity ($v_T(m/s)$). The coordinates (H_u, $v(H_u)$) correspond to the upper boundary of the universal behavior. Quantities between parenthesis are the errors associated to each parameter. The data depicted for Au/Co/Au and Ta/CoFeB/MgO are deduced from results reported in references [60] and [9] respectively.

4.2 Universality of the depinning transition

Let us now address the universality of the depinning transition. We recall the predicted asymptotic behavior for the variation of velocity with temperature at the depinning threshold ($H = H_d$) [74, 10]:

$$v(H_d, T) = v_T(H_d, T)\left(\frac{T}{T_d}\right)^{\psi} \tag{4.3}$$

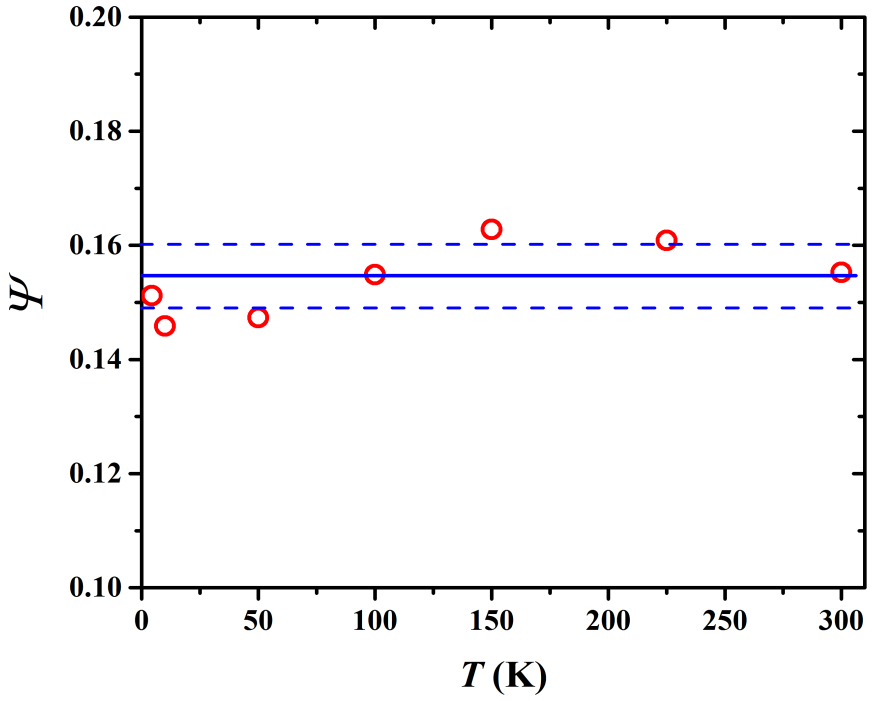

Figure 4.4: **Depinning critical exponent.** Depinning critical exponent ψ deduced from experimental v *vs* H curves as a function of temperature for the Pt/Co/Pt v vs H curves.

In the case of applied magnetic field H for $T \ll T_d$:

$$v(H, T \ll T_d) = v_H(H, T) \left(\frac{H - H_d}{H_d} \right)^{\beta}. \tag{4.4}$$

Here, H_d and T_d are respectively, the depinning field and temperature obtained from the fit described in the previous section, and displayed in table 4.1. Equations 4.3 and 4.4 define the depinning velocities v_T and v_H. In order to identify the magnetic field range over which the depinning transition could present universal behavior, we assume $\psi = 0.15$ and $\beta = 0.25$. Those values correspond to the numerical predictions of the elastic line model with short-range elasticity in a random-bond short-range correlated weak pinning potential, previously shown to be compatible with the observed creep behavior [74, 10]. As it can be observed in figure 4.2, the predictions of Eq. 4.4 present a good agreement with the measurement over a narrow field range for all the explored temperatures. Let us analyze the depinning transition in more detail.

4.2.1 Universality at the depinning threshold.

We can determine the depinning velocity v_T at $H = H_d(T)$ from equation 4.3 for different T. As it can be observed in figure 4.2, this parameter $v_T(T)$ presents good agreement with the velocity corresponding to the asymptotic flow regime. This suggest that v_T corresponds to the velocity that the DW would have in the absence of pinning. The values of v_T are also shown in table 4.1.

Moreover, in order to estimate the value of ψ directly from the velocity curves at $H = H_d$, we take $v_T = mH_d$, where m is the measured slope of the flow regime, and substitute it in equation 4.3. We show the obtained values of ψ in figure 4.4 from where we see that ψ is temperature independent. The average value is $\psi = 0.154 \pm 0.006$. This value is in very good agreement with previous experimental reports [44] and numerical predictions [10], and gives a first signature of the universality of the depinning transition.

The velocity v *vs* magnetic field H curves for Au/Co/Au and Ta/CoFeB/MgO films [9, 60] (see Fig. 4.3), also present an inflection point corresponding to the depinning threshold $(H_d(T), v(H_d(T)))$. However, the linear flow regime is not observed at high drive. Therefore, we cannot determine the value of ψ from those results.

4.2.2 Upper boundaries of the depinning transition.

The next step to analyze universal behaviors of the velocity *vs* field, above the depinning threshold $(H_d, v(H_d))$. We aim to find a criterion to set the upper limit of the depinning transition H_u. In table 4.1 we observe that the depinning temperature T_d is at least one order of magnitude larger than the experimental T in every curve, i.e. $(T \ll T_d)$. For this reason, part of velocity curves should follow the predictions for low temperature limit $T \ll T_d$, only with $\beta = 0.25$ (see Eq. 4.4).

In order to find this upper limit H_u, the values of the prefactor v_H were adjusted so that the predictions by Eq. 4.4 present the largest possible matching region with the experimental velocity curves (see the solid part of the curves in figure 4.2 (A)). As expected, a good agreement is only obtained over a limited field range. In every case the agreement between Eq. 4.4 and the experimental data starts slightly above H_d due to thermal effects. The onset of the divergence between the experimental curve and the fit of equation 4.4, can define the upper boundary of the depinning regime $(H_u, v(H_u))$. The obtained values are reported in table 4.1. Above $H_u(T)$, the DWs follow a non-universal crossover to the linear flow regime observed at larger drive, since it seems to be material dependent.

4.2.3 Universal depinning function.

Once we set the boundaries of the depinning transition, we investigate the universality of the entire regime ($H_d < H < H_u$) beyond power laws and critical exponents.

Following a more general scaling hypothesis [100], the DW velocity at the depinning transition can be described as a generalized homogeneous function [11, 88], which implies the following scaling form:

$$y = g\left(\frac{x}{x_0}\right) \tag{4.5}$$

where the dimensionless variables: scaling field (x) and scaling velocity (y), are defined as:

$$x = [(H - H_d)/H_d]^{\beta}(T/T_d)^{-\psi}, \tag{4.6}$$

and

$$y = (v/v_T)(T/T_d)^{-\psi}. \tag{4.7}$$

Here, $x_0 = v_T/v_H$ is the ratio [88] between depinning parameters. In this model, the function g is expected to be universal within a given class of universality, as it is the case for the critical exponents. The shape of the function g should be consistent with the two asymptotic behaviors in equations 4.3 and 4.4. The ratio x_0 is a priori a non-universal parameter.

Let us first discuss the variations of the ratio $x_0 = v_T/v_H$ as a function of the reduced temperature T_d/T. Figure 4.5 shows that x_0 is found to be temperature independent ($x_0 = 0.64 \pm 0.02$). As a direct consequence, a unique value of x_0 allows the predictions of equation 4.4 to describe the full set of velocity curves as shown in figure 4.2.

Furthermore, an identical analysis can be performed for other ferromagnetic ultrathin films (see figure 4.3). The obtained results present a particularly good agreement for CoFeB [9] ($x_0 = 0.64 \pm 0.02$) and a slightly lower value $x_0 (= 0.62 \pm 0.02)$ for Au/Co/Au [60]. Since the mean values vary by less than 5 % over wide explored range of reduced temperature ($10 < T_d/T < 170$), x_0 can be reasonably considered as material and temperature independent. This suggests that the temperature-dependent parameters ($v_T = x_0 v_H$, H_d, and T_d), are sufficient to describe the whole domain-wall glassy (extremely slow) dynamics in a universal way.

Let us now discus the universal depinning function g. For the depinning parameters H_d, v_T and T_d, we can deduce the values of the scaling variables x and y. In figure 4.6 we show the variation of experimental values for the scaled velocity y as a function of the scaled driving field x (see Eqs. 4.6 and 4.7). For this curve we plot only the data points $(H, v(H))$, for $H_d < H < H_u$.

We observe that all the experimental velocity curves collapse onto a single master

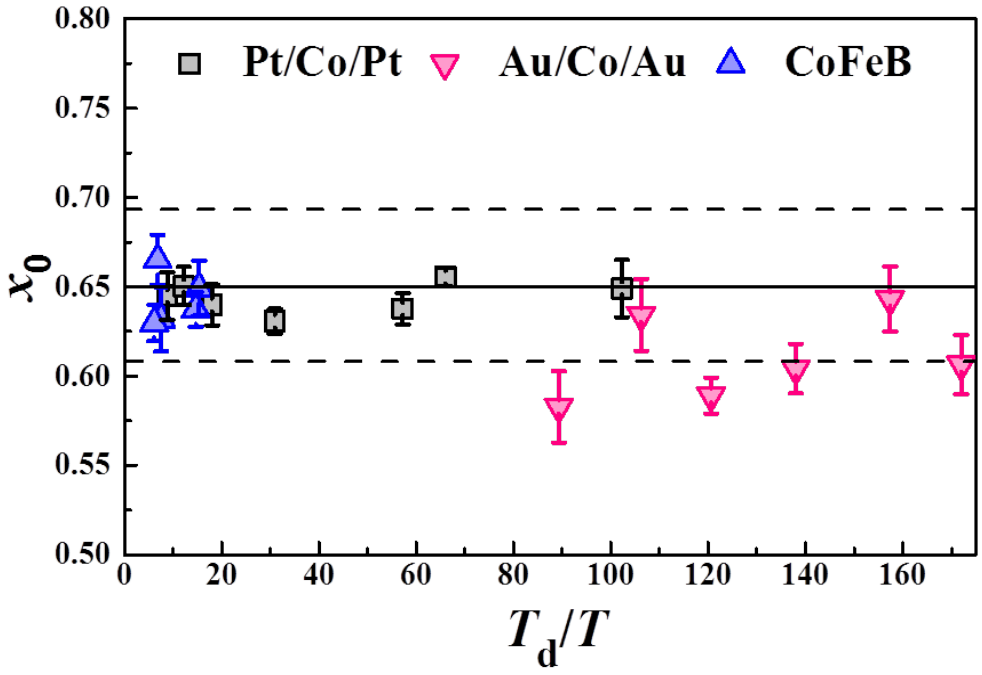

Figure 4.5: **Universal velocity ratio x_0.** Universal velocity ratio $x_0 = v_T/v_H$ as a function of the reduced temperature T_d/T for different ferromagnetic materials. The solid and dashed lines indicate the average value and standard deviation deduced from a fit of the curve in Fig. 4.2 and 4.3, respectively.

curve, indicating that the reduced variables x and y describe the depinning transition and lead to the universal function g. The expected linear asymptotic behavior for $T \to 0$, and $y = g(x/x_0) \to x/x_0$ is observed for $x > 0.8$. Following Eq. 4.6, this indicates that over the magnetic field range $H_d[1 + 0.8(\frac{T}{T_d})^\psi] < H < H_u$, the velocity is well described by the asymptotic limit for $T \to 0$ given by Eq. 4.4.

For $x < 0.5$, the scaled field y remains almost constant, and the data for $x \to 0$ (for $H \to H_d$), can be extrapolated to $y = 1$ in agreement with Eq. 4.3.

Therefore, the universal g function essentially displays two linear asymptotic behaviors and a narrow crossover region ($0.5 < x < 0.8$) centered around $x = x_0 \simeq 0.65$. This is in qualitative agreement with predictions deduced from numerical simulations, which found $x_0 \sim 1$ [11, 12].

An accurate empirical description of data (see the solid lines in figure 4.6) is given by:

$$g(x) = [1 + (x - x_0)^n]^{1/n}, \tag{4.8}$$

where n reflects the width of the crossover between the two asymptotic limits. The best fit

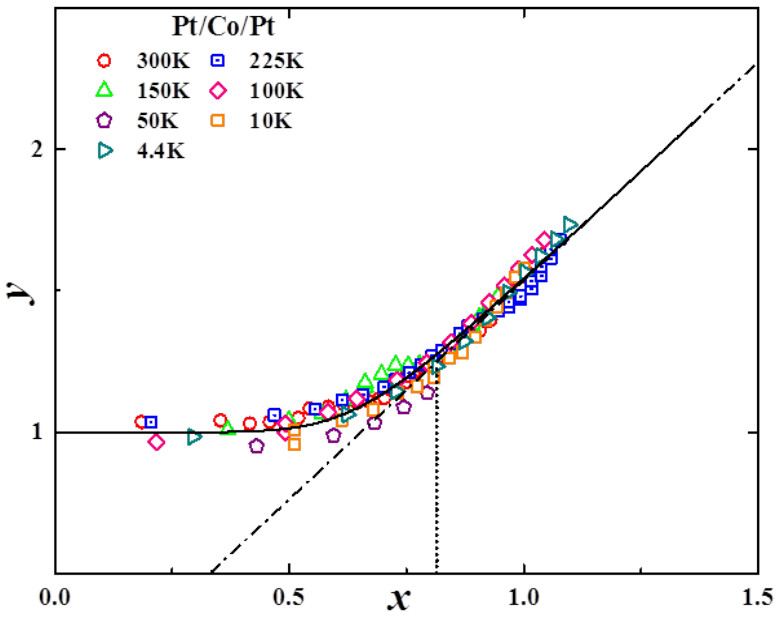

Figure 4.6: **Universal depinning scaling function** Universal depinning function obtained using the scaled domain-wall velocity y as a function of the scaled field x. The data points correspond only to the depinning transition ($H_d < H < H_u$). The solid curve is the empirical function $g(x/x_0)$ describing the data. The dashed-dotted straight line is the linear asymptotic limit of this function.

is obtained for $x_0 = 0.65 \pm 0.04$, $n = 8.7 \pm 0.4$.

As it is shown in figure **??**, this equation is also found to be relevant for other magnetic materials. For Au/Co/Au [60] and CoFeB [9] the data taken from the v *vs* H curves collapse into an identical single curve as the one for Pt/Co/Pt with the same values for the parameters n, and x_0. This confirms that the depinning transition exhibits a universal behavior, which can be described by a unique universal function. This function includes both the field and thermal effects.

4.2.4 Thermal effects on the depinning velocity.

The shape of the universal depinning function allows to go beyond the usual asymptotic analysis. In particular, we adress in this section the thermal rounding of the depinning transition.

In figure 4.8 we present a comparison of the velocity curves in reduced coordinates (v/v_T *vs* H/H_d) for increasing values of the reduced temperature T_d/T covering a large range ($9 - 172$). For the creep regime ($H/H_d < 1$), the velocity presents a strong variation with temperature associated to the thermal activated nature of the motion.

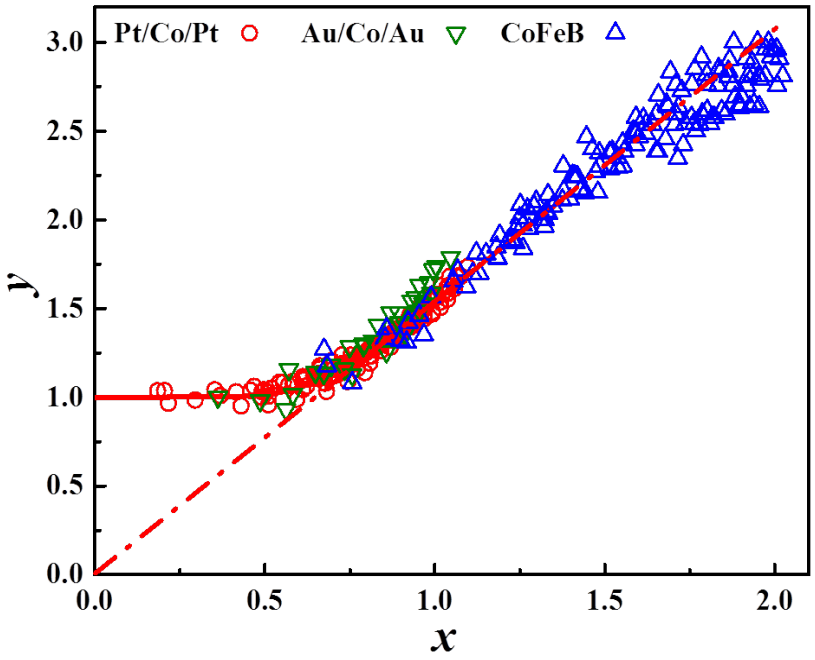

Figure 4.7: **Universal depinning scaling function for different materials.** Scaled domain-wall velocity y as a function of scaled field x for Pt/Co/Pt, Au/Co/Au and Ta/CoFeB/MgO.

For the depinning transition, just above the depinning threshold ($H/H_d \simeq 1$), the thermal effects are still important as shown in the area of figure 4.8 highlighted in gray.

The magnetic field interval for which thermal effects are relevant increases when the ratio $T_d/T \gtrsim 1$. For $T_d/T \gg 1$, the interval where thermal effects are observable is almost negligible.

As described in the previous paragraph, the thermal effects are expected to play a role in the depinning transition only when the scaled driving force is $x < 0.8$. Following the definition of the scaled dimensionless variables (Eqs. 4.6 and 4.7), this corresponds to $H/H_d \lessapprox 1 + [0.8(T/T_d)^{\psi}]^{1/\beta}$ which is the upper magnetic field boundary below which thermal effects are observed in the depinning transition. In consequence, there is an upper limit for the velocity $v \approx v_T\ 0.8/x_0$.

Figure 4.8 shows that the reduced velocity curves agree with the predictions of equation 4.4 for a range of H/H_d that decreases as T_d/T increases. Moreover, for the explored reduced temperature range, no more thermal effects are observed above $H/H_d \approx 1.1$. Above this limit, the reduced velocity displays explicit temperature independence as reflected by the merging of the curves on predictions of equation 4.3.

The crossover between the depinning transition and the flow regime is also shown in figure 4.8. The upper limit of the depinning transition H_u/H_d depends strongly on

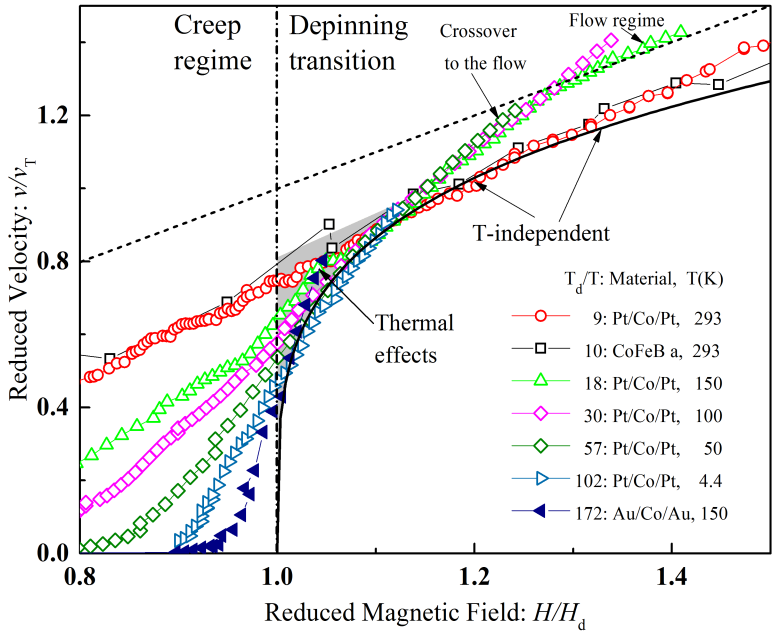

Figure 4.8: **Domain wall dynamics in reduced coordinates.** Domain-wall velocity in reduced coordinates for different reduced temperatures T_d/T and materials. The vertical dashed-dotted line corresponds to the depinning threshold which separates the creep regime ($H/H_d < 1$) from the depinning transition ($H/H_d > 1$). The inclined dashed line corresponds to the linear flow regime ($v/v_T = H/H_d$). The solid curve corresponds to the zero-temperature depinning curve. The gray surface area is the magnetic and velocity ranges over which thermal effects contribute to the velocity. At higher drive, the reduced velocity becomes independent of temperature as reflected by the merging of velocity curves on the solid curve. Eventually, velocity curves quit the universal depinning transtion at a magnetic field H_u which depends on temperature and material and undergo a crossover to the flow regime

temperature and materials properties. In the case of Pt/Co/Pt, H_u/H_d varies between 1.1 and 1.3 over the reduced temperature range $T_d/T = 9 - 102$ and it is significantly smaller than for CoFeB ($H_u/H_d = 3 - 4$). The variation of H_u/H_d and of $x_u = 1.1 - 2.0$ suggests that the limit of universality H_u is not a universal parameter.

4.3 Chapter summary

In this chapter we provided a self-consistent phenomenological framework for analyzing the sub-threshold thermally activated creep regime and the depinning transition of domain walls in magnetic thin films. This whole dynamics are controlled by only three material dependent parameters: H_d, v_T, and T_d. In figure 4.9 we summarize the detailed analysis for all the dynamics in a typical v *vs* H curve in Pt/Co/Pt at room temperature.

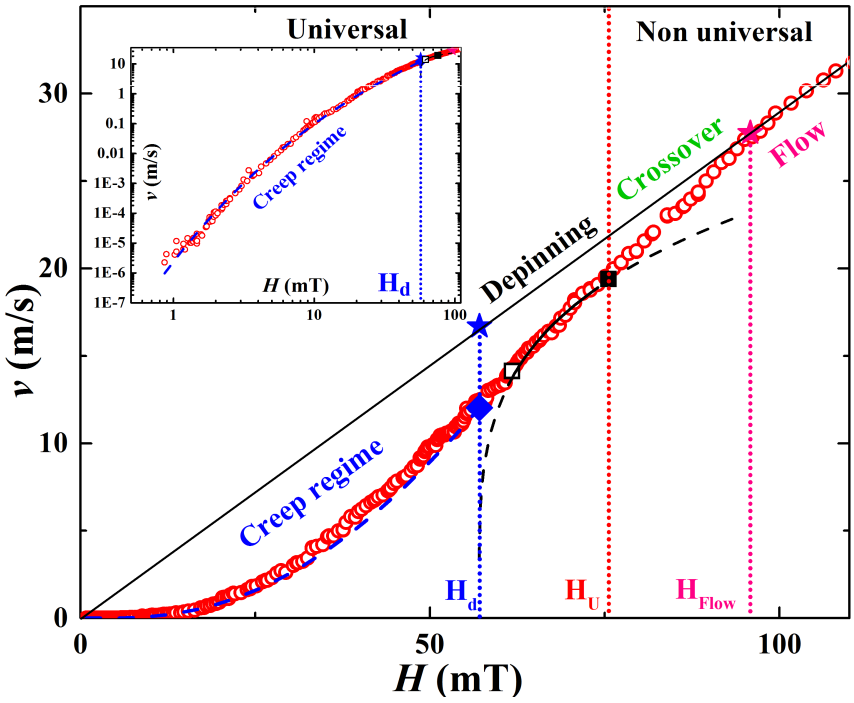

Figure 4.9: **Universal and non-universal behaviors of magnetic field driven domain walls.** DW velocity (v) *vs* field (H) in Pt/Co/Pt at room temperature. The universal and non-universal dynamics are separated by the boundary field H_u, which corresponds to the upper limit of the depinning transition. Within the non-universal dynamics, DWs present a crossover between the depinning transition and the linear flow regime. The threshold $H = H_d$ separates the creep regime ($H < H_d$) from the depinning transition ($H_d < H < H_u$). The solid black straight line corresponds to the linear extrapolation of the flow regime. The dashed blue curve is a fit of the creep regime. The dashed black curve is a fit for the depinning transition using $x_0 = v_T/v_H \simeq 0.65$. The part that matches with experimental data is underlined by black solid segments. The blue diamond and star points are the velocity at depinning $v(H_d)$ and the depinning velocity v_T. The parameter $v(H_d)$ corresponds to the inflection point separating the creep regime from the depinning transition and H_{flow} corresponds to the beginning of the flow regime. Inset: log-log plot of the velocity curve highlighting the creep regime.

We evidenced the universal behavior of the depinning transition for three different materials and more than one order of magnitude of reduced temperature variation (T/T_d). The depinning transition is characterized by a universal scaling function g of the rescaled field, temperature, and velocity. The shape of this function governs the domain-wall velocity including its asymptotic scaling law behaviors.

We also found that the parameter $x_0 = v_T/v_H$ in the function g, is material independent, and has an experimental value of $x_0 = 0.64 \pm 0.02$, which was *a priori* not expected to be universal.

Finally, we showed that the universal behavior extends over the whole creep regime and the depinning transition, as it is shown in figure 4.9.

This work opens new questions regarding the material and temperature dependent parameters, such as their relation with micromagnetic parameters and microscopic pinning properties (coherence length of the disorder and pinning strength).

CHAPTER 5

Dimensional cross-over of the creep motion

"...but Alice had got so much into the way of expecting nothing but out-of-the-way things to happen, that it seemed quite dull and stupid for life to go on in the common way...."

Lewis Carrol.- Alice's adventures in Wonderland

In this chapter we analyze the motion of magnetic domain walls driven by magnetic field in ferromagnetic (Ga,Mn)(As,P) films of different thickness.

As discussed in chapter 2, DW motion in the creep regime results from a series of events where the DW overcomes a series of energy barriers and passes from one stable configuration until it reaches the next stable configuration passing through several metalstable configurations, this series of events are known as avalanches. The characteristic length of the excitation that triggers the avalanches producing DW motion [36] is known as optimal length $L_{opt}(f)$, which decreases as the driving force is increased ($L_{opt}(f) \sim f^{-}1/(2-\zeta)$). Finite size effects are expected to occur when $L_{opt}(f)$ has the same order of magnitude as one length-scale of the medium embedding the DW [63, 37].

A well known example of finite size effects is the DW motion in ultra thin films [70]. As $L_{opt}(f)$ always remains larger than the film thickness t, the DWs behave as elastic lines ($d = 1$) moving in a two dimensional medium ($D = 2$). Another evidence of finite size effect was reported in narrow tracks (of width $w < 600nm$) made from ultrathin films by Kim et

al. [58]. The motion was shown to present a crossover between a $1d$ elastic line criticality ($L_{opt}(f) < w$) at high drive and a $0d$ hopping behavior ($L_{opt}(f) > w$) at low drive. In this chapter, we explore the crossover between a $1d$ and a $2d$ creep motion of a DW.

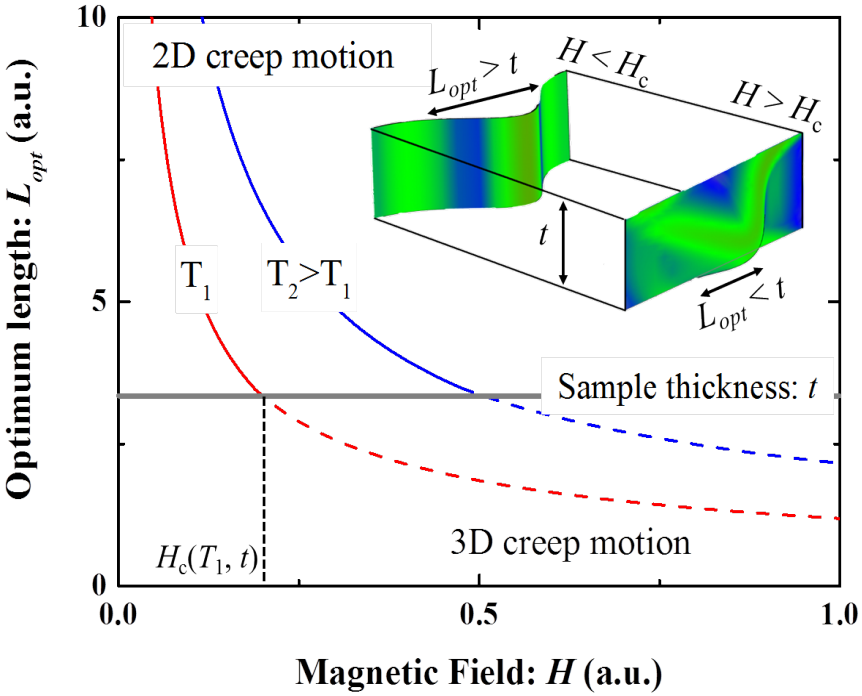

Figure 5.1: **Dimensional crossover of creep motion.** Variation of the optimal length $L_{opt}(H)$ with magnetic field for two different temperatures ($T_2 > T_1$). At low drive $L_{opt}(H) > t$, where t is the sample thickness, the DW behaves like a line ($d = 1$) moving in a 2D film. At larger drives ($L_{opt}(H) < t$), the DW can be considered as a surface ($d = 2$) moving in a 3D film. The solid curve indicates the region where L_{opt} is larger than t and therefore the DW presents a line ($d = 1$) behavior. The dashed line indicates where L_{opt} is smaller than t and analogously, the DW behaves like a surface ($d = 2$). At $H = H_c(T, t)$ the sample thickness is the same as the avalanche size are ($L_{opt} = t$).

In figure 5.1 we illustrate the predicted variation of L_{opt} with magnetic field H. The optimal length L_{opt} decreases with increasing magnetic field. For a given film thickness t, a dimensional crossover should occur at a critical magnetic field $H = H_c(T, t)$ for which $L_{opt} \approx t$. Above $H_c(T, t)$, as $L_{opt} < t$, the DW should behave as an elastic surface ($d = 2$) moving in a three dimensional medium ($D = 3$). In contrast, below $H_c(T, t)$, as $L_{opt} > t$, the DW should behave as an elastic line ($d = 1$) moving in a two dimensional medium ($D = 2$).

Some of the questions we try to unravel in this chapter are following. What are the experimental parameters (critical field and film thickness) allowing to observe the creep motion of two dimensional wall ($d = 2$)? How can we obtain non-ambiguous signatures of the expected dimensional cross-over?

Theoretically, the equilibrium roughness exponent for a $d = 1$ elastic line is predicted to be $\zeta = 2/3$ according to analytical calculations [14]. In contrast, for an elastic surface ($d = 2$), theoretical calculations, including anharmonic contributions for the elastic energy and assuming that the elasticity is isotropic, predict $\zeta_{eq} \approx 2/5$ the equilibrium and $\zeta_{dep} = 0.45$ as depinning exponents [70, 91]. Accordingly, the creep exponent should vary between $\mu = 1/4$, for $1d$ elastic lines [14, 70], and $\mu = 1/2$ for a $2d$ elastic surface [80, 14]. To our best knowledge, experimental evidences of such variations of critical exponents has no yet been reported in the literature.

In order to answer these questions we compare the velocity v *vs* magnetic field H curves for (Ga,Mn)(As,P) films with different thicknesses: 12, 50 and 80 nm. We show that a single exponent is not sufficient to describe the whole creep regime. We measure the roughness exponent for the three samples at different fields and we compare the experimental velocity curves with the predictions for the quenched Edwards-Wilkinson (qEW) model for an elastic line ($d = 1$) and an elastic surface ($d = 2$).

5.1 Domain Wall dynamics and dimensionality

In figure 5.2 we show magnetic field (H) driven domain wall (DW) velocity (v) curves at different temperatures for 12.5 and 80 nm thick (Ga,Mn)(As,P) samples with out of plane magnetization. An inflection point $(H_d(T), v(H_d(T))$ is systematically observed and corresponds to the depinning threshold which separates the thermally activated creep regime ($H < H_d(T)$) from the depinning transition ($H > H_d(T)$).

For the 80 nm thick sample, we observe the linear variation observed at high drive ($v > 5m/s$) corresponds to the precessional flow regime. Indeed, the straight dashed lines indicated in figure 5.2 extrapolate the flow regime to low drives. The measured mobility, corresponding to the slope ($m = v/H = 0.38 \pm 0.02$), is close to the reported value [26] for the precessional flow regime in similar samples. For the 12.5 nm thick sample, we observe the beginning of the linear flow regime as indicated by the dashed line in figure 5.2 (B), however for this sample, the measured mobility corresponds to the slope ($m = v/H = 0.60 \pm 0.04$).

In the creep regime ($0 < H < H_d(T)$), the velocity is strongly dependent on temperature, as reported in figure 5.3. It varies over several orders of magnitude in a relatively small range of magnetic field, as expected for a thermally activated motion. However, the shape of curves for the thickest sample is strongly different from those reported for ultrathin films for which the log of the velocity varies linearly with $H^{-1/4}$. In contrast, as shown in figure 5.3 (A), the curves present "kinks" (indicated by the filled diamonds). An agreement with the $H^{-1/4}$ law is only observed for the lowest drives. Moreover, part of the velocity curves present a better agreement with a $H^{-1/2}$ (see figure 5.3 (B)), which is the prediction for the motion of an elastic surface.

In our system, however, a "kink" (indicated by filled diamonds in 5.3) that breaks the

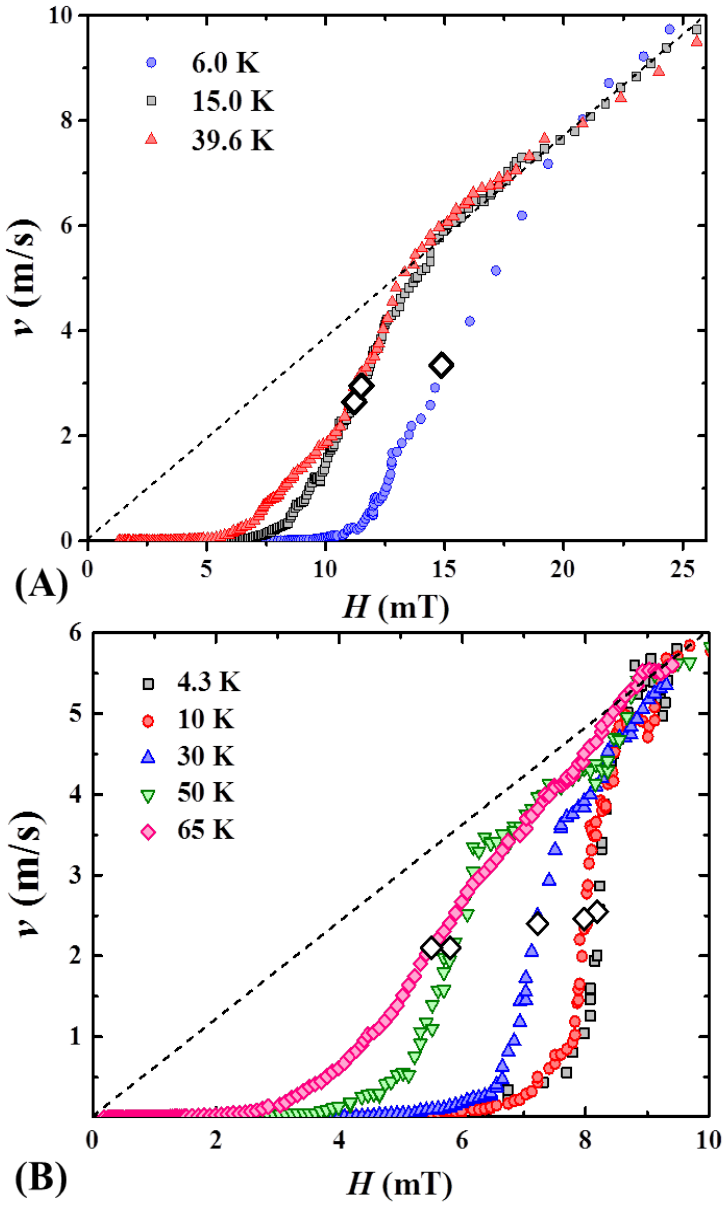

Figure 5.2: **Domain wall velocity *vs* field at different temperature.** (A) DW velocity v as a function of magnetic field H measured for a 80 nm and (B) a 12.5 nm thick (Ga,Mn)(As,P) film. The inflection points, indicated by open diamonds, correspond to the depinning threshold $(H_d(T), v(H_d(T), T))$ separating the creep regime ($H < H_d$) from the depinning transition. At higher fields we show the linear flow regime (highlighted by the dashed straight line).

linearity in the semi-log v *vs* $H^{-\mu}$ curve is systematically observed at well defined coordinates $(H_c(T), v(H_c(T), T))$. In order to characterize quantitatively the origin of this "kink" we fit

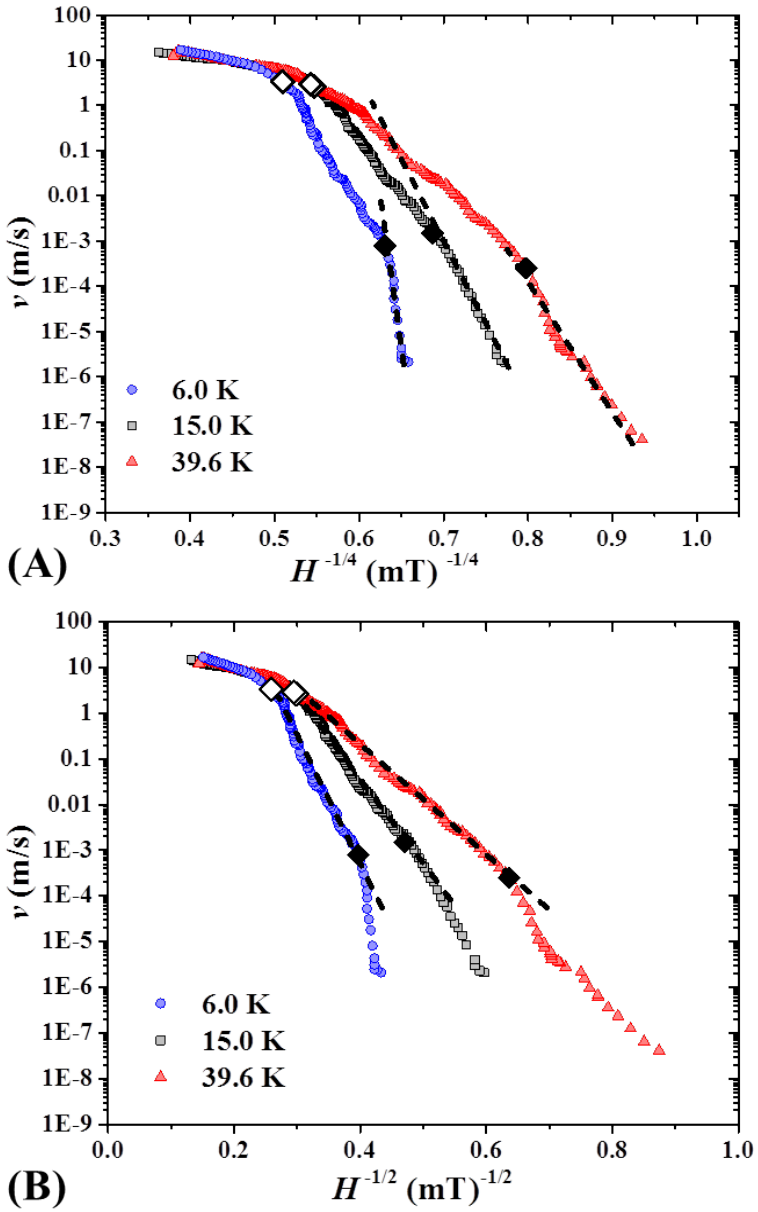

Figure 5.3: **Domain wall velocity *vs* H^{μ}.** (A) DW velocity v as a function of magnetic field $H^{-1/4}$ in semi-log scale measured for a 80 nm thick (Ga,Mn)(As,P) films. The dashed line is the range of field where the experimental data is compatible $d = 1$ and $\mu = 1/4$. We indicate the dimensional crossover (filled diamonds) as the point where the linear fit deviates from experimental data. (B) DW velocity *vs* $H^{-1/2}$ in semi-log plot. The dashed lines is the range of field where the experimental data is compatible with $d = 2$ and $\mu = 1/2$: from the dimensional crossover (filled diamonds) until the depinning threshold (indicated by open diamonds).

the creep equation:

$$v(H,T) = v_i exp\left(- \frac{k_B T_d}{k_B T} \left[\left(\frac{H}{H_i} \right)^{-\mu} - 1 \right] \right), \tag{5.1}$$

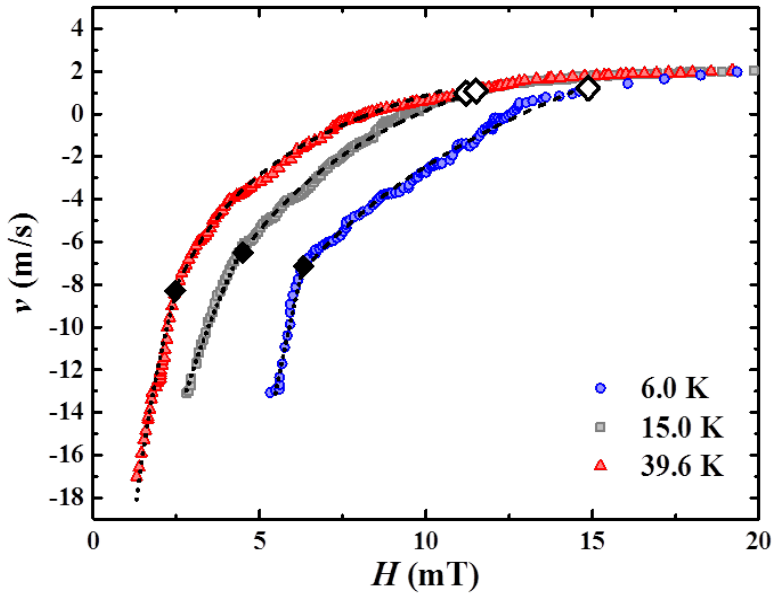

Figure 5.4: **Logarithmic domain wall velocity *vs* field H.** Logarithmic DW velocity v as a function of magnetic field H for a 80 nm thick (Ga,Mn)(As,P) film. The dotted line is the best fit of Eq. 5.1 $d = 1$ and $\mu = 1/4$. We indicate the dimensional crossover (filled diamonds) as the point where the linear fit deviates from experimental data. The dashed line for $H_C < H < H_d$ indicates the best linear fit for $d = 2$ and $\mu = 1/2$ ranging from the dimensional crossover (filled diamonds) until the depinning threshold (indicated by open diamonds).

where k_BT is the thermal activation energy, and μ the universal creep exponent. In equation 5.1, the material and temperature dependent pinning parameters are the characteristic pinning energy scale (k_BT_d) and the coordinates (H_i, v_i) is the set-of of the divergence between the experimental velocity curve and the creep equation.

This is illustrated in figure 5.4 where the logarithmic DW velocity is plotted for the 80 nm thick sample. Below the field where the "kink" is found ($0 < H < H_c(T)$), the curves in figure 5.4 are fitted with a critical creep exponent $\mu = 1/4$ and a first set of parameters ($v_i = v(H_c(T), T)$, $H_i = H_c(T)$, $T_i = T_c(T)$) (dotted curve). Above this threshold in ($H_c < H < H_d(T)$) the fit was done with a different creep exponent ($\mu = 1/2$) and another set of parameters ($H_i = H_d(T)$, $v_i = v(H_d, T)$ and $T_i = T_d$), used in order to find an accurate fit of the experimental curves with the creep equation (dashed curve).

The compatibility of velocity curves with the predicted creep exponents $\mu = 1/4$ for $H < H_c(T)$, and $\mu = 1/2$ for $H_c(T) < H < H_d(T)$ suggests a dimensional crossover between a line ($d = 1$) and a surface ($d = 2$) behavior of DWs. In table 5.1 we report the crossover parameters that corresponds to the coordinates where the creep equation, for $d = 1$ ($\mu = 1/4$) and the experimental curve diverge. We also show the material and temperature depinning parameters used for fitting the creep equation for $d = 2$ ($\mu = 1/2$)

between ($H_c < H < H_d$).

$t(nm)$	$T(K)$	$dynamics H_c(mT)$	$roughness H_c(mT)$	$H_d(mT)$	$T_d(K)$
80	6 (0.1)	6.3 (0.5)		14.9 (1)	110 (20)
	15 (0.1)	4.5 (0.5)	5.0 (0.4)	11.2 (1)	224 (20)
	39 (0.1)	2.5 (0.4)	2.5 (0.3)	11.5 (1)	315 (20)
50	30 (0.1)	3.3 (0.4)		3.3 (0.4)	1119 (100)
	60 (0.1)	1.2 (0.2)	1.4 (0.1)	3.2 (0.2)	855 (50)
	90 (0.1)	0.6 (0.1)	0.8 (0.2)	3.2 (0.4)	564 (20)
	96 (0.1)	0.2 (0.1)		3.1 (0.2)	547 (50)
12	4.3 (0.1)	3.8 (0.5)		8.2 (0.5)	324 (40)
	10 (0.1)	3.7 (0.3)		7.9 (0.4)	713 (50)
	30 (0.1)	2.6 (0.3)		7.2 (0.3)	1041 (40)
	50 (0.1)	5.2 (0.3)	5.7(0.4)	5.8 (0.3)	1041 (40)

Table 5.1: **Material and temperature dependent crossover and depinning parameters.** For each (Ga,Mn)(As,P) sample with different thickness (nm) the temperature of the experiment ($T(K)$) is indicated. Then we show the fitted crossover field ($H_c(T)$) for the creep law with $\mu = 1/4$ and the crossover field ($H_c(T)$) identified by the roughness exponent shift. In the last two columns we show fitted parameters for the creep equation with $\mu = 1/2$: the depinning magnetic field (H_d) and the depinning temperature (T_d).

5.2 Roughness exponent

In order to confirm that the variation of the creep exponent is associated to a dimensional crossover, we have investigated the roughness scaling properties of domain walls [70]. We have calculated the displacement-displacement correlation function of domain wall displacements $u(x)$ defined by:

$$w(L) = \langle |u(x+L) - u(x)|^2 \rangle \tag{5.2}$$

where x corresponds to a position on the DW (in this case a point in the inner red contour as shown in figure 5.5 (A)), the parameter L is the length of a segment. The symbol $\langle\rangle$ corresponds to an average of measurements over all the positions x.

The displacements $u(x)$ were deduced from the subtraction of two consecutive Kerr images as it is illustrated in figure 5.5 (A). In this case, $u(x)$ corresponds to the shortest distance between the two red contours and L is the length of the curve segment in the inner contour. In figure 5.5 (B) we present typical examples of computed correlation function $w(L)$ *vs* L in log-log scales for different magnetic fields in the 80 nm sample. In each case we observe a linear behavior for $L < 10$ μm.

The linear behavior in the correlation functions of figure 5.5 (B) implies that the expected power law variation $w(L) \sim L^{2\zeta}$ is present. We fit a line within the range $(1 - 5\mu m)$

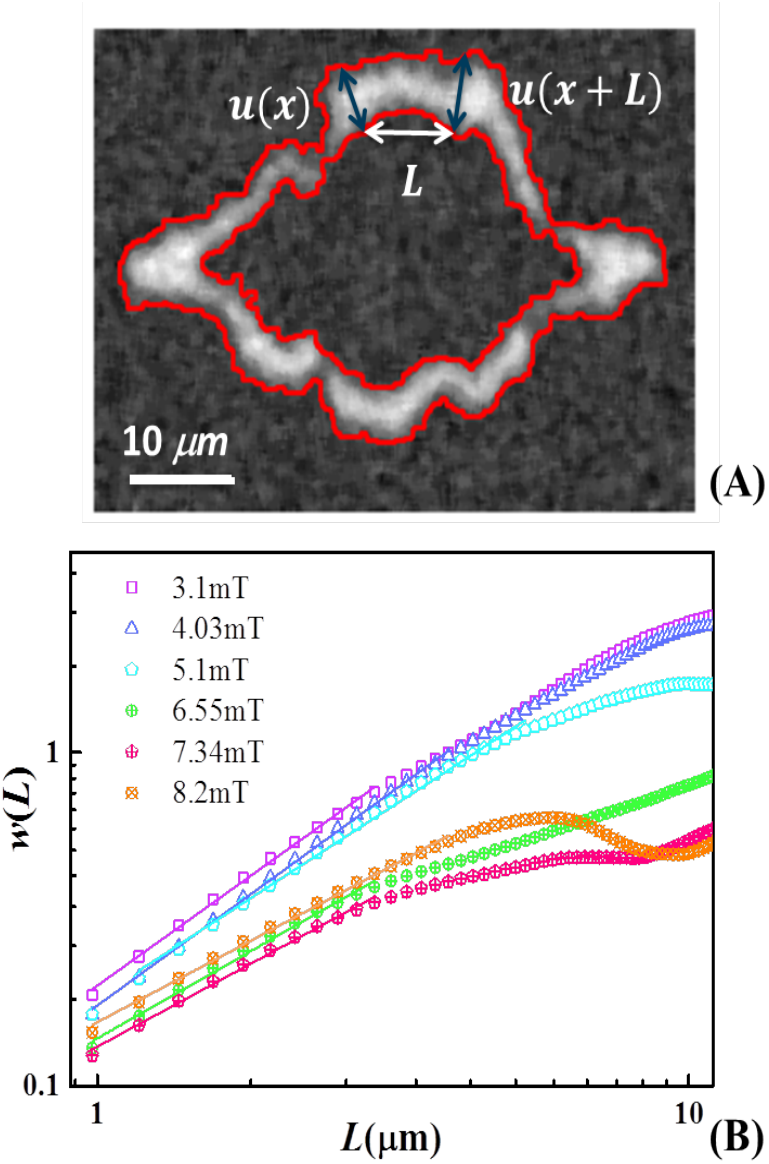

Figure 5.5: **Displacement-displacement correlation function for different field values.** (A) Typical image of a domain wall displacement (in light gray) deduced from differential Kerr imaging showing two successive domain wall positions (indicated by the red contours). (B) Displacement correlation function $w(L)$ *vs* segment length L along the domain wall in log -log scale obtained for different applied magnetic field values with the 80 nm thick film and $T = 15$ K. The solid lines are fits for the lowest L -values of the scaling relation $w \sim L^{2\zeta}$. Two separated sets of curves are presenting a different slope (empty symbols and crossed symbols). The slope change is observed for $H = 5.1 - 6.55$ mT and corresponds to step of the roughness exponent ζ.

over which the universal scaling is observed. The slope of the linear fit corresponds to twice the roughness exponent 2ζ. The lower limit ($L > 1\mu m$) is fixed above the microscope reso-

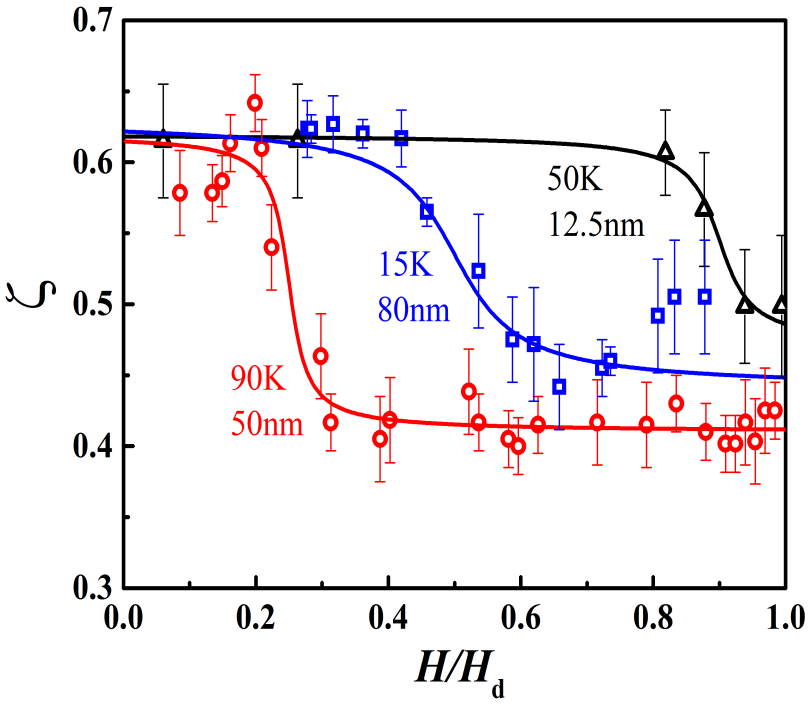

Figure 5.6: **Roughness exponent (ζ) as a function of the reduced magnetic field.** Roughness exponent ζ as a function of the reduced magnetic field H/H_d for three film thicknesses and different temperatures. The step between the two ζ-values reflect a dimensional crossover between $1d$ and $2d$ behavior. The curved lines are a visual guide.

lution and width of the Gaussian filter used during the image processing, which corresponds to 3-4 times the length of the microscope resolution. The upper limit is simply where the linear fit and the experimental curve diverge. This range is rather narrow compared to usual measurements [70, 85]. This, most probably originates from the anisotropy of domain wall displacements, which is due to the small in-plane magnetic anisotropy [28].

In figure 5.5 (B) we can observe that the curves are grouped in two groups according to their slopes: at low field ($H \leq 5.1mT$) the $w(L)$ curves present a larger slope than at large field ($H \geq 6.55mT$). Therefore we can expect that the crossover is somewhere between the field values ($5.1mT < H_c < 6.55mT$) and that the roughness exponent presents different values for the two ranges of applied magnetic field. Indeed for the analyzed temperature ($T = 15K$) we found in the previous section that the crossover field was $H_c = 4.6 \pm 0.5$ mT .

In order to determine more precisely the value of the magnetic field at which the crossover is observed, ζ was measured systematically as a function of applied magnetic field. Typical results are reported in figure 5.6 for the three film thicknesses, and different temperatures. As it can be seen, the curves present a sigmoid shape. The high level is close to $\zeta_{1d} = 2/3$ and the low level value close to $\zeta_{2d} = 2/5$, which is compatible with a dimensional

crossover. By taking into account the measurements performed sufficiently away from the crossover, we obtain the global average values $\zeta_{1d} = 0.62 \pm 0.02$ and $\zeta_{2d} = 0.45 \pm 0.04$, respectively.

In figure 5.6 we can also see that the range in which the crossover occurs in rather narrow (between $0.1 - 0.2H/H_d$). This allows us to define more accurately the crossover field H_c as the inflection point of the curves. The obtained values are reported in table 5.1 for different sample thicknesses and temperatures. The values of the field in the inflection point of the ζ-curves (figure 5.6) and the "kink" in the v *vs* H (figure 5.2) are found to coincide within experimental error bars. This confirms that the DW present a dimensional crossover between a $1d$ and a $2d$ universal behavior, which is highlighted by a change of critical exponent values.

5.3 Critical exponents

In this section we compare our measurements of critical exponents to theoretical predictions.

Below the critical field H_c, the measured average roughness exponent $\zeta_{1d} = 0.62 \pm 0.02$ and the creep exponent ($\mu = 1/4$) used to fit the velocity curves are in good agreement with previously reported results ($\zeta = 0.69 \pm 0.07$) and ($\mu = 0.24 \pm 0.04$) obtained for ultra-thin films presenting an isotropic growth [70]. This confirms that the domain wall can be considered as an elastic line ($d = 1$) in a $2D$ medium.

For an elastic line ($d = 1$), analytical calculations [14] and numerical simulation [92, 91] including an-harmonic contributions for the elastic energy in the q-EW equation predict $\zeta_{eq}^{1d} = 2/3$, close to equilibrium ($f \approx 0$) and $\zeta_{dep}^{1d} = 0.635$ close to the depinnning transition ($f \approx f_d$). Both values are found in good agreement with our experimental findings ($\zeta_{1d} = 0.62 \pm 0.02$). Moreover, as it is discussed in references [37] and [63], if we want to compare the predicted exponents (ζ_{eq} or ζ_{dep}) with experimental findings, we need to take into account the scale L_{MOKE} at which the domain wall motion is observed, in our case $L_{MOKE} \approx 1\mu m$ is the resolution of our MOKE microscope. Indeed, fluctuations are expected to be described by the equilibrium roughness exponent ζ_{eq} for $L_{MOKE} < L_{opt}$ and by the depinning exponent ζ_{dep} for $L_{MOKE} > L_{opt}$. This means that experimentally we have access to the roughness exponent at the depinning ζ_{dep}.

Close to the crossover field H_c we are in a case where ($L \approx L_{opt} \approx t \in [12 - 80nm]$) while the roughness exponent is determined for lengths in the micrometer scale ($L = 1 - 5\mu m$). Therefore, our result presents a good agreement with the predicted critical depinning roughness exponent ζ_{dep}^{1d} for the quenched Edward-Wilkinson (qEW) Universality class.

Above the critical field H_c, the obtained roughness exponent value is $\zeta_{2d} = 0.45 \pm 0.04$. For an elastic surface ($d = 2$), the predictions including an an-harmonic contribution for the elastic energy are $\zeta_{eq}^{2d} = 0.41$ and $\zeta_{dep}^{2d} = 0.45$, for equilibrium and depinning roughness

[92, 91] exponent, respectively. Both values are pretty close to the experimental findings. However, as the observation length-scale L is larger than L_{opt}, our results are in agreement the predictions for depinning roughness exponent $\zeta_{dep}^{2d} = 0.45$.

On the other hand, the corresponding creep exponent is given by the scaling relation $\mu = (d+2\zeta_{eq}-2)/(2-\zeta_{eq})$ which leads to $\mu_{2d} = 0.52 \pm 0.07$. This is in good agreement with the creep exponent ($\mu = 1/2$) used to describe the velocity curves. Therefore, our results are compatible with the predicted scaling relation.

5.4 Optimal length

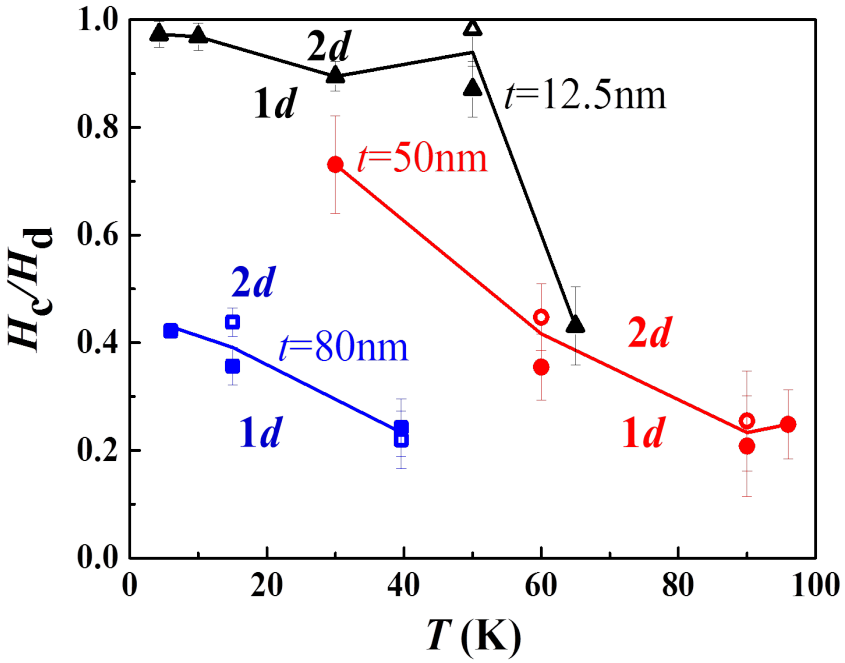

Figure 5.7: **Temperature variation of H_c/H_d.** H_c/H_d *vs* T deduced from the kink in the velocity curves (filled symbols) and from the "step" in the value of the measured roughness exponent ζ (empty symbols). The dimensional crossover is shifted towards the depinning transition ($H_c/H_d = 1$) for decreasing film thickness.

We now discuss the variation of the optimum length with the drive H and with temperature. In figure 5.7, we report the ratio H_c/H_d between the critical and the depinning field as function of temperature for the three different film thicknesses. The curve obtained for each film thickness separates the reduced magnetic field range corresponding to a $d = 1$ ($H/H_d < H_c/H_d$, i.e. $L_{opt}(T) > t$) and a $d = 2$ ($H/H_d > H_c/H_d$, i.e.$L_{opt}(T) < t$) behavior.

As it can be observed in figure 5.7, for a fixed temperature (for example $T = 40K$), the

range over which the $2d$-creep is observed, i.e. $(H/H_d > H_c/H_d)$, decreases with decreasing film thickness. As the crossover is expected to occur for $L_{opt}(H) \approx t$, the results reported in the same figure are in qualitative agreement with the predicted variation of $L_{opt}(H)$ $(\sim H^{-}1/(2-\zeta))$ with drive the H.

Moreover, for a fixed ratio H_c/H_d, $L_{opt}(H,T)$ is decreasing with increasing temperature. This strongly suggests that the maximum size of the activated events $(\approx L_{opt}(H,T))$ which overcome the energy barriers and ultimately, controls the average DW velocity in the creep, decreases with increasing temperature.

5.5 Chapter summary

In conclusion, we have evidenced the two dimensional creep behavior of magnetic domain wall motion in the thermally activated creep regime. We were able to determine the variation of the crossover field H_c with film thickness and temperature. At low drive, below the crossover field $(H < H_c(T,t))$, the velocity curves follow the well studied $1d$ creep law: the DW behaves as an elastic line moving in a $2D$ medium $(\mu_{1d} = 1/4)$. Above the crossover field and below the depinning field $(H_c(T,t) < H < H_d)$ the experimental velocity curves follow the creep law predicted for a $2d$ elastic surface moving in a $3D$ medium $(\mu_{2d} = 1/2)$.

This scenario was confirmed by an independent DW roughness analysis. At the same critical field $H_c(T,t)$, we observed a step of the measured roughness exponent from $\zeta_{1d} = 0.62 \pm 0.02$ to $\zeta_{2d} = 0.45 \pm 0.04$, which is a clear signature of the dimensional crossover. Indeed, the measured roughness exponent values were found in good agreement with theoretical predictions ($\zeta_{dep}^{1d} = 0.635$ and $\zeta_{dep}^{2d} = 0.45$ [37, 63]). Additionally we show that the maximum avalanche size $L_{opt}(H,T)$ decreases with increasing drive and temperature.

Our analysis should shed light on interface dynamics in weakly disordered systems whose dimensions are larger than the optimal triggering events. Moreover, as the $1d$ and $2d$ creep motion is described by the same quenched Edwards-Wilkinson equation with anharmonic elasticity corrections, the dimensional crossover should also present a universal character.

CHAPTER 6

Current driven domain wall motion

"It is this new property of current-driven exchange which implies the novel mesoscopic magneto-dynamics illustrated below. These motions due to spin transfer can dominate over those due to precession about the magnetic field...."

J.C. Slonczewski - Current-driven excitation of magnetic multilayers.

This chapter, presents a study of current induced domain wall (DW) motion. We analyze the temporal evolution of the shape of DWs, their roughness and dynamics. We discuss in particular, the thermally activated creep regime, and address the question of universality class of current induced DW motion. An interesting starting point of this study is the comparison with the well documented magnetic field induced DW motion.

We recall briefly the main results of the previous studies on the compared criticality of current and magnetic field induced DW motion in the creep regime. For CoFeB/MgO tracks, DuttaGupta *et al.* [31] determined different values of the creep exponent for current ($\mu_j = 0.39 \pm 0.06$) and field ($\mu_H = 0.23 \pm 0.07$) induced DW motion. For Pt/Co/Pt films, Moon *et al.*[76] observed a very strong faceting of DWs and measured different roughness exponent for current ($\zeta_j = 0.99 \pm 0.01$) and field ($\zeta_H = 0.68 \pm 0.04$) induced DW motion. The difference between critical exponents suggests that current and field induced DW motion belong to different universality classes. Moon *et al.* propose that current induced DW

motion belongs to the negative quenched Kardar-Parisi-Zhang (q-KPZ) universality class. However, the results are not compared to theoretical predictions. Moreover, the onset of the facets close to strong pinning centers suggests that different pinning disorder control the motion of DWs.

As only few studies have been published on this topic, several issues remain to be addressed. We list here some important questions we try to answer in this chapter. Can we observe the faceting of domain walls in other materials than Pt/Co/Pt? What is the origin of the facets? How could the contribution of spin transfer torque (STT) be described as a driving force? To what extent the current induced creep regime presents universal behaviors? Do we confirm the strong difference between the criticality of current and field induced DW motion? Is there a strong difference between the pinning processes as suggested by Moon *et al.*?

In order to discuss those questions, we proposed several experimental improvements. We choose to study an ultra-thin (Ga,Mn)(As,P) film. In this material, the depinning current and field are sufficiently low for all the dynamical regimes to be observed (from the creep to the flow regimes). Therefore we have access to the whole creep regime, while previous studies were restricted to the low [31] and ultra-low creep regimes [76]. This also increases substantially the flexibility of experiments since the faceting of DWs can be observed in less than a minute, while for Pt/Co/Pt ultra-thin films around four hours are needed. Moreover, the motion of DW is observed in extended geometry. This eliminates possible contributions of edge pinning, which may modify DW dynamics [47], and allows a combined measurement of the roughness and creep exponents. Finally, previous studies are made at room temperature [76] or cover a narrow range of temperature [31, 112]. Our measurements cover more than one order of magnitude in temperature, which allows to distinguish temperature dependent and universal behaviors.

6.1 Evolution of domain wall shape

Typical sequences showing successive DW shape and position driven by current and magnetic field are reported in Fig. 6.1. The sample is a (Ga,Mn)(As,P) $4nm$ thick film as we described in detail in chapter 3. In particular we choose a $200\mu m$ window where the ferromagnetic part of the sample is visible. In figure 6.1 (A), a constant magnetic field ($H \sim 0.2\ mT$) is applied perpendicularly to the plane of the film. The images are taken each $\Delta t = 0.5s$. For figure 6.1 (B), the experiment is performed with a constant current density ($J \sim 0.5\ GA/m^2$), at the same location of the sample. The images are taken each $\Delta t = 0.5s$.

For the magnetic field drive, the initial DW shape is relatively well conserved during the motion. Close to strong pinning centers (see red triangles in figure 6.1 (A)), the DWs become curved, when they pin, and flat again when they depin. This is typical of an interface whose motion is described by the quenched Edward-Wilkinson (qEW) model.

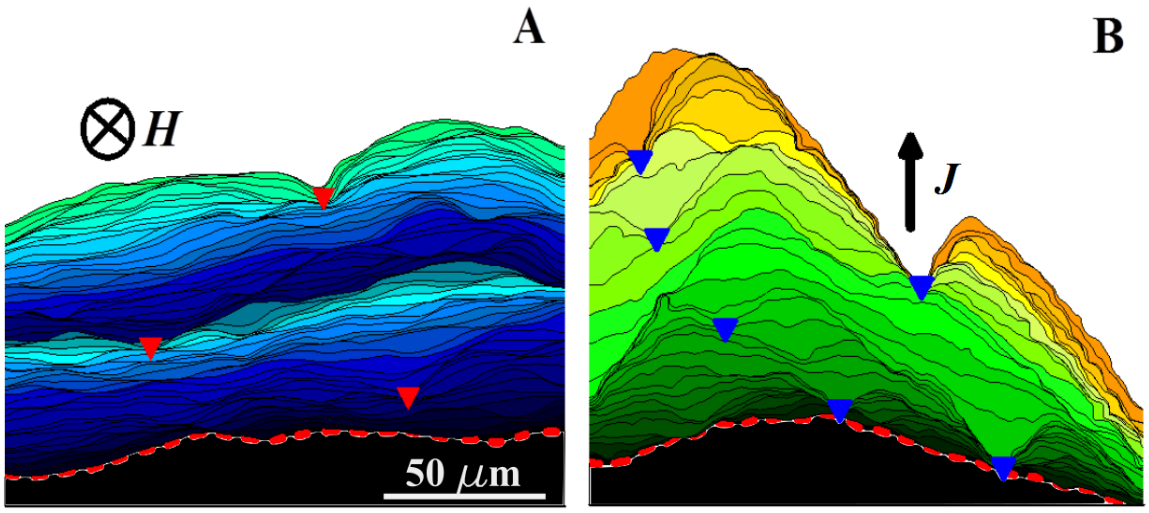

Figure 6.1: **Magnetic field and current induced DW motion.** Successive position of a DW driven by a constant (A) magnetic field $H = 0.16mT$. The time step between images is $\Delta t = 0.5s$, and the total duration is $60s$ and (B) current density $J = 0.45\ GA/m^2$ ($\Delta t = 0.5s$, total duration $16s$). The direction of the field and current density are indicated by a cross $\otimes$ and an arrow, respectively. In both cases, DWs are moving upwards from an initial underlined by the red dashed line. The red and blue triangles indicate strong pinning sites. Both succession of images were taken in the same location of the film.

For current induced DW motion the situation is different. The initial DW shape is not conserved during the motion. Facets are formed when the DW encounters strong pinning centers.

We define a strong pinning center one section of the DW does not move (stays pinned) during ≈ 4 times the duration of the time step Δt and there is distortion of the DW. In other words, when we look at the DW trajectory through the successive DW positions driven by field or current density, we define a strong pinning center when 4 or more DWs overlap on the same position and the shape of the DW is distorted when it passes through the center. This is an arbitrary criteria and depends on the used time step (Δt), however we used similar time steps in all our experiments ($\Delta t = 0.5\mu s$ and $1\mu s$).

As it can be observed in figure 6.1 (B), there is a clear correlation between the displacement of DW and its relative orientation to the current density direction $\vec{J}$. The largest displacements are observed when the normal direction to the DW $\vec{n}$ is parallel to $\vec{J}$. As the angle between $\vec{n}$ and $\vec{J}$ increases, the mean DW displacement $\langle u(x) \rangle$ decreases. The shape of the current induced DW motion is strongly different to the case of magnetic field which acts an isotropic force. For a limit facet angle ($\approx 45°$), the DW velocity tends to decrease, as expected for a motion described by the negative quenched Kardar-Parisi-Zhang model (qKPZ) [56, 92]. The velocity measurements described in later are only performed for $\vec{n} \parallel \vec{J}$.

6.2 Domain Wall roughness

In this section, we compare the roughness of DWs driven by current and magnetic field. We analyze their variation with time and temperature. The estimation of roughness exponents is deduced from computing the correlation function of the DW displacement.

6.2.1 Statistical quantities in surface roughening

For both driving forces, H and J, we measure the displacement-displacement correlation function at different times after the driving force H, or J, is applied:

$$w(L) = \langle |u(x+L) - u(x)|^2 \rangle. \tag{6.1}$$

In our case, L is the length of a DW segment along the x axis, and $u(x)$ is the displacement perpendicular to the DW as it is shown in figure 6.2 (A). Typical examples of displacement-displacement correlation functions obtained for the magnetic field and electrical current driven DWs are shown in log-log plots in figure 6.2 (B).

As it can be observed, above the spatial resolution of the microscope ($\sim 0.5\mu m$), the displacement-displacement correlation function presents a linear variation over a DW length $L \approx 10\ \mu m$, clearly reflecting the self-affinity of DWs. In order to obtain a value of ζ, we perform a linear fit fixing the lower and upper limit in the following way: the lower limit starts just above the spatial resolution of the microscope ($0.5\ \mu m$) or, when it is the case, above the length of the averaged section of the image (we use Gaussian filter in the image processing). The size of the filter is usually 2-3 times the spatial resolution of the microscope. Below this limit, the correlation function $w(L)$ depends exclusively on image properties and image processing procedures and not on the actual correlations in the DW. The upper limit is established simply as the divergence point between the linear fit and the experimental correlation function $w(L)$.

We obtained a linear fit from this section of the $w(L)$, and from the relation $w(L) \sim L^{2\zeta}$, we obtain the roughness exponent ζ as half of the slope in the linear fit.

As it can be observed in figure 6.2, the slope of the curves are similar for current and field induced DW motion. Consequently, the values of the roughness exponent are close ($\zeta_H = 0.70 \pm 0.01$ for the field and $\zeta_j = 0.71 \pm 0.01$ for the current). For field induced DW motion, the measured roughness exponent is close to the prediction of the qEW model ($\zeta_{eq} = 2/3$ and $\zeta_{dep} = 0.63$). For current induced DW motion, the measured roughness exponent is significantly lower than the value reported by Moon *et al.* ($\zeta_j = 0.99 \pm 0.01$). In order to obtain an accurate value of the roughness exponent, we performed the same procedure for succession of DW positions, as shown in figure 6.1, and repeated the experiment over a

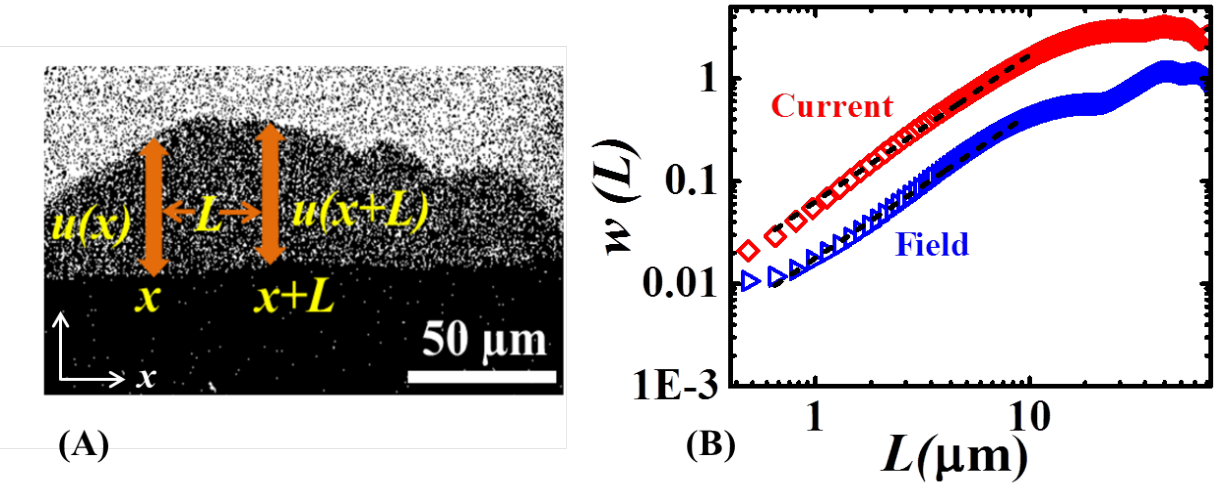

Figure 6.2: **Correlation function definition.** (A) Subtraction of consecutive domain images where the current induced DW displacement $u(x)$ of the coordinate x is indicated in the beginning and the end of a segment $u(x+L)$ of lenght L along the DW. (B) Typical correlation function $w(L)$ vs DW segment L in log-log scale, for current driven DW motion (red diamonds) and field induced DW motion (blue triangles) for $T = 14K$. The dashed lines indicate the linear section from which the roughness exponent is estimated. In this example the obtained values for current and field induced motion are $\zeta_j = 0.71 \pm 0.01$ and $\zeta_H = 0.70 \pm 0.01$ correspondingly.

temperature range covering one decade (from 6 to $59K$).

6.2.2 Roughness exponent and temperature

Let us now examine the variation of the roughness exponent ζ as a function of time and temperatures. In figures 6.3 to 6.5, we show the temporal evolution of the roughness exponents deduced from successive DW positions, as presented in figure 6.1 for magnetic field H and current density J, correspondingly.

For magnetic field driven domain wall, figure 6.3 shows the temporal variation of $\zeta_H(H,T)$ for different values of H and temperature T varying over a decade ($T = 6 - 59K$). Each point was deduced from a fit of the correlation function as discussed in the previous subsection. As it can be observed, $\zeta_H(T)$ is globally independent of time except at short times ($t < 7s$) for some experiments (See figure 6.3 (C), (E), (I), (J), and (K)). The origin of this variation can be discussed from figure 6.4, which compares the time evolution of the mean DW velocity $< v(t) >$ and the roughness exponent $\zeta_H(t)$.

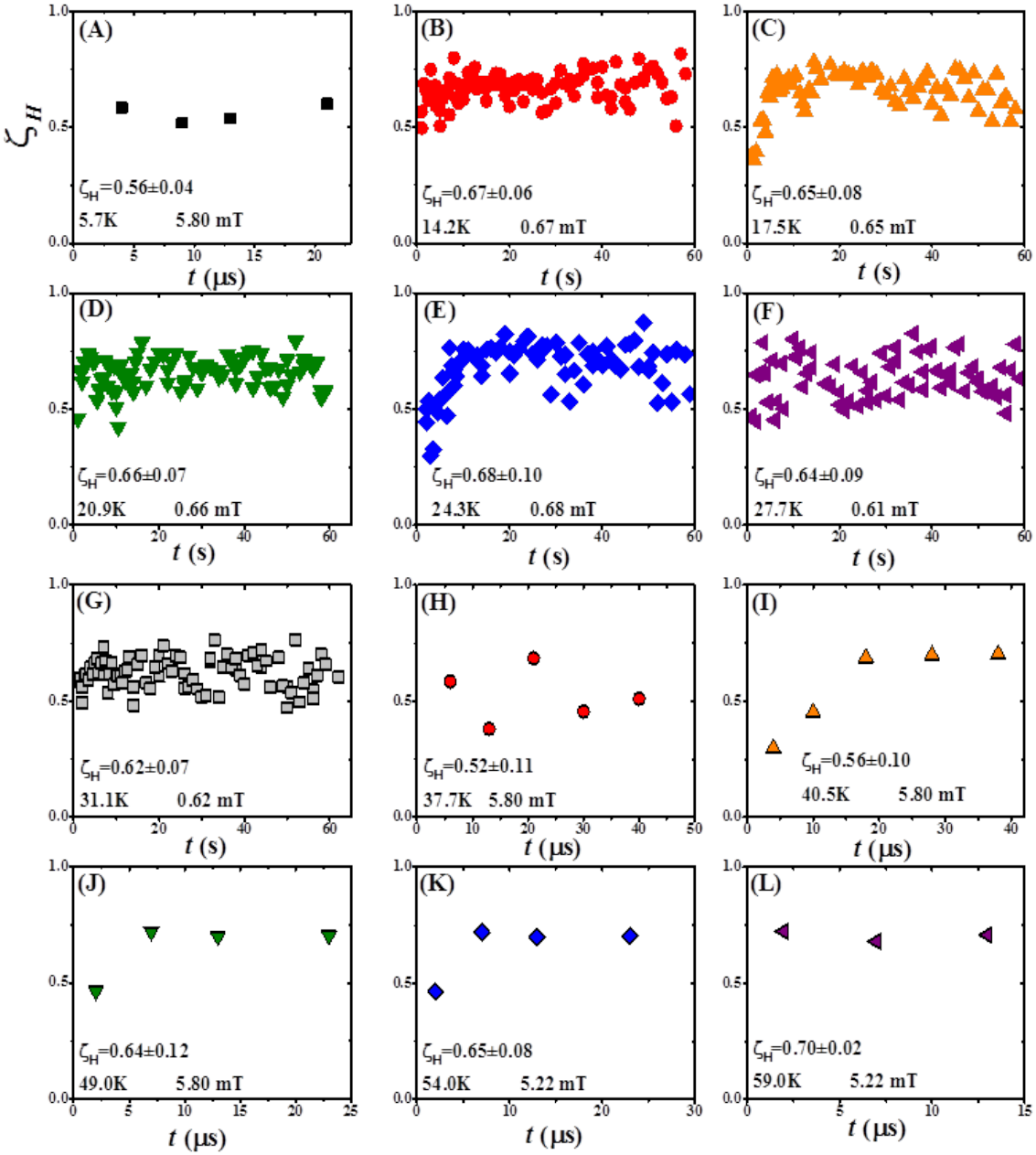

Figure 6.3: **Roughness exponents ζ_H *vs* time.** ζ_H as a function of time for different temperature and applied magnetic field values. For the curves C, E, I, J, and K, ζ_H initially increases with time and then becomes constant, reflecting the transient and steady creep regimes. For all the other curves, ζ_H remains constant within experimental fluctuations. The average ζ_H value for the steady creep with standard deviation is indicated below each curve. The corresponding temperature and the constant magnetic field H are shown for each experiment.

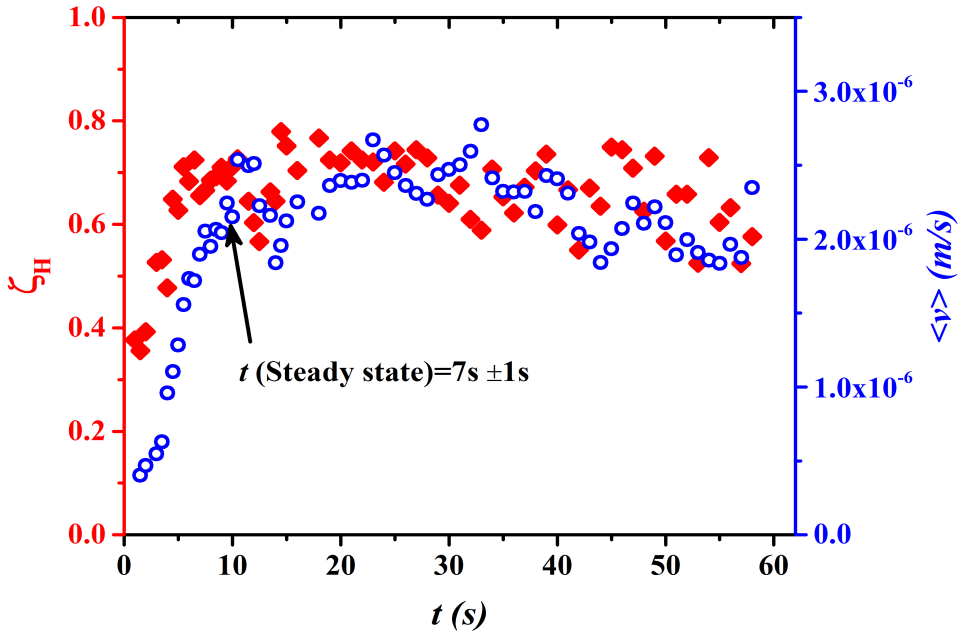

Figure 6.4: **Transient Regime.** Time variation of mean DW velocity (blue open circles) and the roughness exponent (red diamonds) with a constant magnetic field $H = 0.7mT$ at a fixed temperature $T = 17K$.

As it can be observed, the velocity $< v(t) >$ increases until it reaches a constant value (for $t > 7s$). The variation of the roughness exponent ζ_H is found to be strongly correlated to the velocity. This curve evidences an increase of the roughness exponent during the transient creep regime ($t < 7s$ in figure 6.4). The reason why transient creep is not systematically observed is not well understood. It probably depends on the way initial DW state was prepared, and the time elapsed since its preparation.

Let us only consider the values obtained in the steady creep regime. Figure 6.6 reports the variation of time average values of $\zeta_H(T)$. As it can be seen, $\zeta_H(T)$ remain constant within experimental error, over the decade of explored temperature, as expected for a universal critical exponent. The value of the roughness exponent, corresponding to an average over all the measurements (~ 350 curves) is $\zeta_H = 0.60 \pm 0.04$. This is consistent with measurements reported in the literature for Pt/Co/Pt ($\zeta_H = 0.69 \pm 0.07$ and $\zeta_H = 0.68 \pm 0.04$, in references [70] and [76], respectively). This value of the roughness exponent is also compatible with the theoretically predicted equilibrium value of $\zeta_H = 2/3$, and the anharmonic depinning value ($\zeta_{dep} = 0.63$) for the Edward-Wilkinson Universality class [91].

For current induced DW motion, the time variation of the roughness exponent $\zeta_J(J, T)$ for different values of J, and a temperature T vaying over a decade ($T = 6-59K$) is reported in figure 6.5. As it can be observed, ζ_J remains independent of time and temperature. The mean values obtained for each temperature present no variation over one decade of

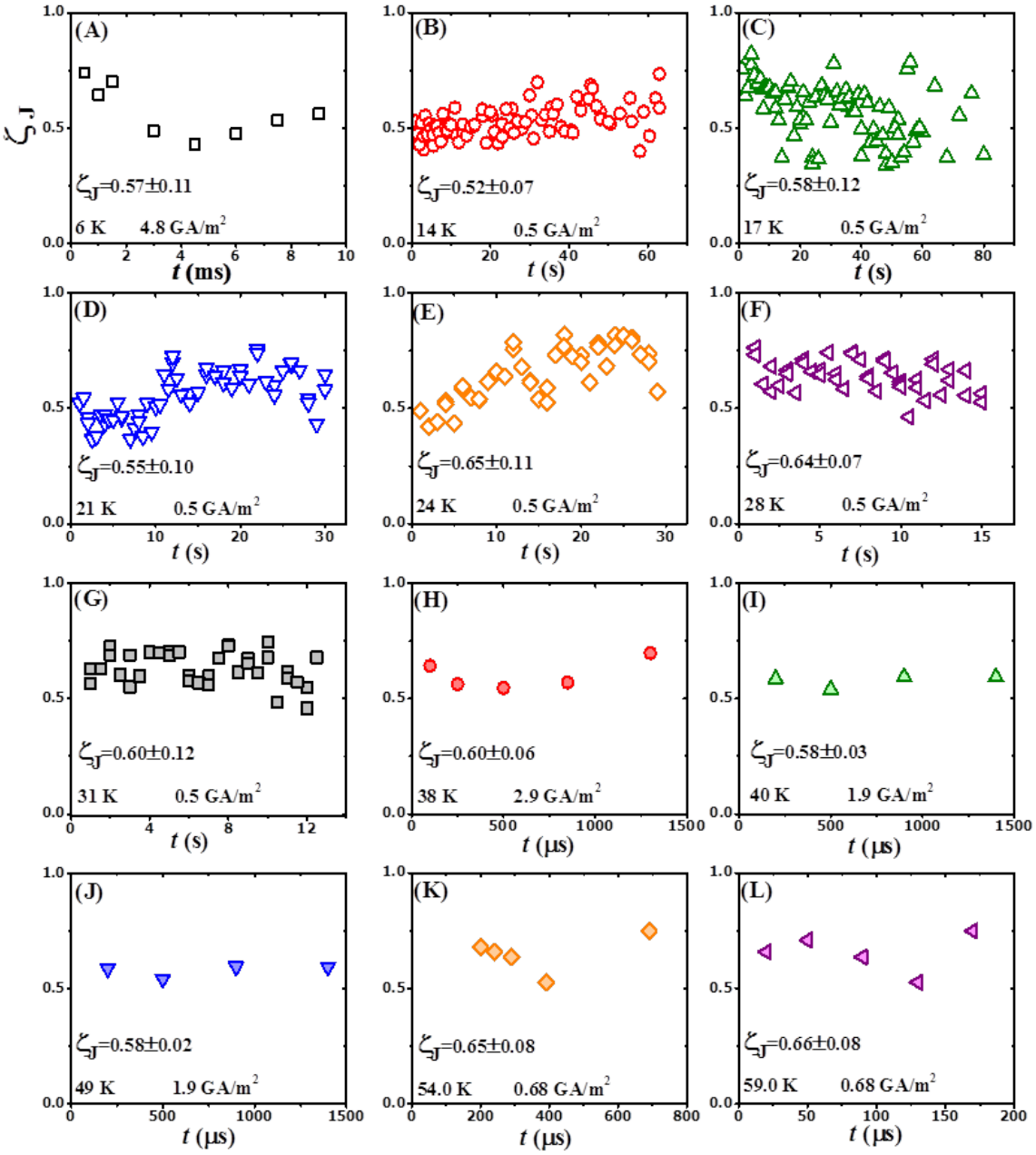

Figure 6.5: **Roughness exponents ζ_j *vs* time.** ζ_J *vs* time for different temperatures T with a constant current density J. In each subplot we indicate the temperature at which each experiment was performed, the value of the constant current density and the average roughness exponent found for each experimental T.

temperature (see Fig. 6.6). The global average value (over ~ 350 values) is $\zeta_J = 0.61 \pm 0.05$.

We now compare our measurements of the roughness exponent to those published by

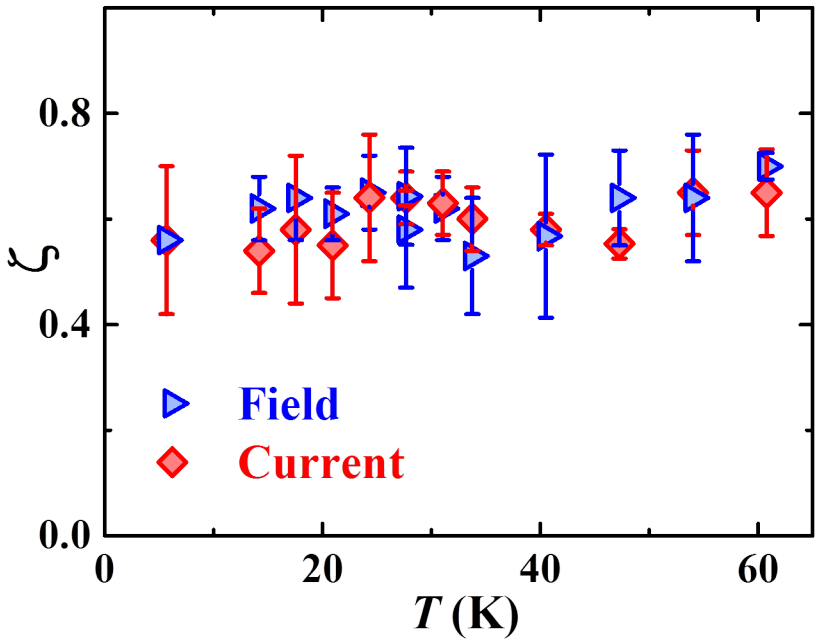

Figure 6.6: **Roughness exponents** for field ζ_H and current ζ_J induced DW motion as a function of temperature. The error bars correspond to the standard deviation of the average roughness exponent at each T.

Moon*et al.* [76]. First, we obtain compatible values for field driven DW motion (($\zeta_H = 0.68 \pm 0.04$) for Moon *et al.*, and $\zeta_H = 0.60 \pm 0.04$). This indicates that both the different methods used for the determination of ζ (via the correlation function of the displacement, for us) lead to compatible results.

For current driven DW motion we obtain a value ($\zeta_J = 0.61 \pm 0.05$) significantly smaller than the one reported by Moon *et al.* [76] ($\zeta_J = 0.99 \pm 0.01$). The result from Moon was obtained from the determination of the standard deviation of displacement $u(x)$ (with respect to a flat base line) along a direction parallel to current $\vec{J}$, and not from the displacement-displacement correlation function. Even for the highest faceting angles, we do not recover the value obtained by Moon *et al.*

Interestingly, Moon *et al.* obtained another value of the roughness exponent for a measurement along the normal to the DWs ($\vec{n}$). The reported value ($\zeta_{J\perp} = 0.69 \pm 0.04$) is compatible with our result ($\zeta_J = 0.61 \pm 0.05$).

This set of results suggests that the self-affinity measured in the direction of the current depends on the tilting angle between the current and the direction normal to the DW. For the largest tilting angle ($\theta_{max} \approx 80°$ for Pt/Co/Pt), the roughness exponent is significantly larger. For the lowest tilting angles (here $\theta_{max} \approx 45°$), the roughness exponent is similar for current and field driven DW motion.

For a measurement of the roughness in the direction normal to the DW or for sufficiently low tilting angles, the self-affinity is compatible with the predicded roughness exponent ($\zeta = 0.63$) for the positive qKPZ and the qEW whith anharmonic corrections on the elasticity [92, 75].

This suggests that for sufficiently low faceting angles, DWs driven by magnetic field and current present a self-affinity corresponding to the quenched Edward-Wilkinson universality class. There, according to the scaling relation $\mu = (2\zeta_{eq} - 1)/(2 - \zeta_{eq})$ with $\zeta_{eq} = 2/3$, the expected creep exponent should be close to $\mu = 1/4$.

6.3 Current driven domain wall motion

In this section, we compare the field and current driven DW dynamics. As discussed in chapter 3, the contribution of Joule effect on current induced DW can be neglected. (The maximum variation of velocity due to Joule heating is $\approx 3\%$, which corresponds to a temperature rise of $0.3K$.) In order to eliminate any contribution of tilting angle to current induced DW dynamics (see figure 6.1), the velocity was always measured from an almost straight DW aligned perpendicularly to the current.

6.3.1 Creep exponent

The velocity curves for current and field driven DW are reported in Fig. 6.7. Here we only present results obtained in a narrow temperature range ($T = 49 - 59K$). Above 59 K the DWs were not stable enough to measure accurately the displacement since we approach the Curie temperature ($T_C \approx 65$) and therefore the Kerr contrast is very weak. Below 49 K, we were not able to reach the depinning transition, which is important for a precise analysis of the creep regime.

At low drive ($H < H_d$ and $J < J_d$), the velocity presents a strong non-linear variation with drive and temperature which characterizes the thermally activated creep regime (see the inset of Figs. 6.7 A and B). At the depinning threshold ($H = H_d$ and $J = J_d$), the curves present inflection points (indicated by diamond signs in Fig. 6.7). The linear variation observed well above the threshold corresponds to the beginning of the flow regime.

In order to discuss the velocity curves more quantitatively, we fit the creep law and proceed to extract the depinning parameters. The velocity in the creep regime is described by the empirical law:

$$v(x,T) = v(x_d,T)\exp\left[-\frac{\Delta E}{k_B T}\right], \tag{6.2}$$

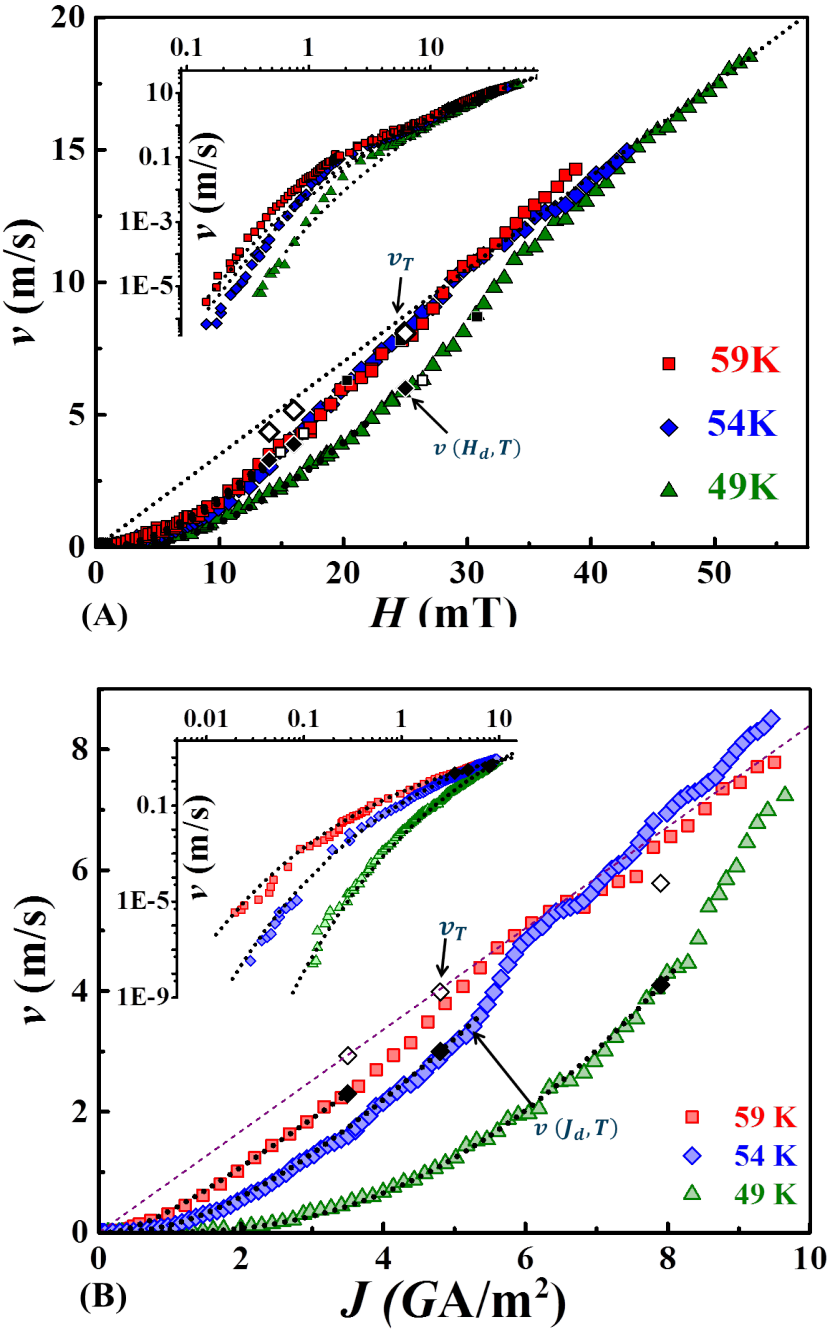

Figure 6.7: **Domain wall dynamics.** Domain wall velocity *vs* (A) magnetic field H and (B) current density J for different temperatures. The insets in figure (A) and (B) are the log-log scales highlighting the creep regime. The solid diamonds indicate the end of the creep regime, being $(H_d, v(H_d))$ and $(J_d, v(J_d))$ the coordinates of the depinning field and current density correspondingly. The dotted lines are the fit of the creep equation.

with

$$\Delta E = k_B T_d \left[\left(\frac{x}{x_d} \right)^{-\mu} - 1 \right], \tag{6.3}$$

where $x = J$ or H. $k_B T$ is the thermal activation energy, $k_B T_d$ the characteristic height of the effective pinning barriers and μ the universal creep exponent.

For magnetic field driven DW motion ($x = H$), a global fit of Eqs. 6.2 and 6.3 of all the velocity curves (see Fig. 6.7 (A, B)) was done using the procedure detailed in chapter 4 [51, 22]. The depinning parameters $H_d(T)$ and $v(H_d, T)$ are fixed and correspond to the inflection point's coordinates. The depinning temperature $T_d(T)$ was taken as a free temperature dependent parameter, and creep exponent μ as a free shared parameter. The fitted creep law is shown in figure 6.7 and presents a good agreement with experimental data. The pinning parameters ($H_d(T)$, $v(H_d, T)$, and $T_d(T)$) are reported in Table 6.1. For the creep exponent, the best global fit gives $\mu_H = 0.247 \pm 0.011$. This value is in good agreement with values reported in the literature [70, 44], and with the predictions for the quenched Edwards-Wilkinson universality class $\mu_H = 1/4$ [63], with random bond and short-range pinning.

Driving force	$T(K)$	$H_d(mT)$	$v(H_d, T)(m/s)$	$T_d(K)$
Magnetic Field	49	32.4 (0.4)	7.6 (0.4)	310 (10)
	54	20.5 (0.4)	5.2 (0.2)	323 (20)
	59	19.7 (0.5)	5.0 (0.4)	329 (12)
	$T(K)$	$J_d(GA/m^2)$	$v(J_d, T)(m/s)$	$T_d(K)$
Current density	49	8.4 (0.6)	5.1 (0.5)	439 (35)
	54	4.9 (0.4)	3.5 (0.4)	349 (25)
	59	3.5 (0.3)	2.3 (0.2)	296 (30)

Table 6.1: **Depinning parameters of DW dynamics.** Fitting parameters of Eqs. 6.2 and 6.3 for different temperature $T(K)$. H_d and J_d are the depinning threshold for the magnetic field and current driven DW motion, respectively. $v(H_d, T)$ and $v(J_d, T)$ are the velocities at depinning and T_d the depinning temperature.

For the current driven DW motion ($x = J$), the same procedure was used to fit the velocity curves. $\mu = \mu_J$ was also set as a shared free parameter. The best fits (see Fig. 6.7 (B)) are obtained for the depinning parameters reported in table 6.1. The obtained creep exponent is $\mu_J = 0.259 \pm 0.004$. This value is in very good agreement with the one deduced for field driven motion ($\mu_H = 0.247 \pm 0.011$) and with the predictions for qEW model. Therefore, for sufficiently small tilting angle between the current direction and the normal of the DW, the current and magnetic field driven DW motion present similar universal behaviors which can be described by the quenched Edward-Wilkinson universality class.

Here, it is important to note that our results are strongly different from the creep exponent reported Yamanouchi *et al.* [112], and DuttaGupta *et al.* [31], for current induced DW motion (Ga,Mn)As and CoFeB/MgO tracks, respectively.

For (Ga,Mn)As, the reported values are $\mu_H = 1.2 \pm 0.1$, and $\mu_j = 0.33 \pm 0.06$. The authors argue that in this material the value of μ_H is compatible with random field disorder and not with random bond disorder implying that the universality class is a different one. However, for almost the same material (Ga,Mn)(As,P), it has been shown (See Jeudy *et al.* [51] supplementary material) that the DW dynamics in the creep regime is compatible with $\mu_H = 1.2 \pm 0.1$ only over a small magnetic field range while the value predicted for a random bond disorder $\mu_H = 1/4$ is compatible with experiments over the whole creep regime. Therefore, one cannot exclude that a similar problem arises for μ_J. In other words, in order to improve the estimation of the creep exponent, it is necessary to measure the DW velocity through the whole creep regime and, if possible be able to obtain the depinning parameters.

For CoFeB/MgO, the value $\mu_H = 0.23 \pm 0.07$ is compatible with q-EW with random bond, short range disorder. Our study indicates we should have a similar value for current induced DW motion, while a different value is reported ($\mu_J = 0.39 \pm 0.06$). A possible origin of the differences could be found in the methods for the determination of the exponent (too narrow temperature and magnetic field range, fit of the data with a creep law which only describes the very low drive regime, undiscussed fitting parameters, etc.), or in the contribution of edge pinning, which diminishes the velocity in the creep regime and leads to overestimation of the creep exponent [47].

6.3.2 Universal energy barriers

In order to analyze the criticality of current induced DW dynamics beyond the asymptotic power law variation, we deduce the effective height of the pinning barrier $\Delta E(x,T)$ from the depinning parameters of Table 6.1. We can rewrite Eq. 6.3 as:

$$\Delta E(x) = k_B T \ln[v(x_d,T)/v(x,T)].$$

In Fig. 6.8, we compare the reduced energy barrier $\Delta E(x)/k_B T_d$ as a function of reduced drive (x/x_d) for $x = H$ and J.

As it can be observed, all the data collapse onto a single master curve over the whole explored range of driving forces, $(0.01 < H/H_d < 1)$ and $(0.01 < J/J_d < 1)$.

This demonstrates that beyond sharing the same asymptotic behavior close to zero drive, the criticalities of current and field induced DW motion share an equivalent universal reduced energy barrier which describes the whole creep regime up to the depinning threshold.

6.3.3 Domain wall pinning and faceting process

We now discuss the contribution of pinning disorder to current induced creep motion and its contribution to the faceting of DWs (see Fig. 6.1). In their letter, Moon *et al.* write that

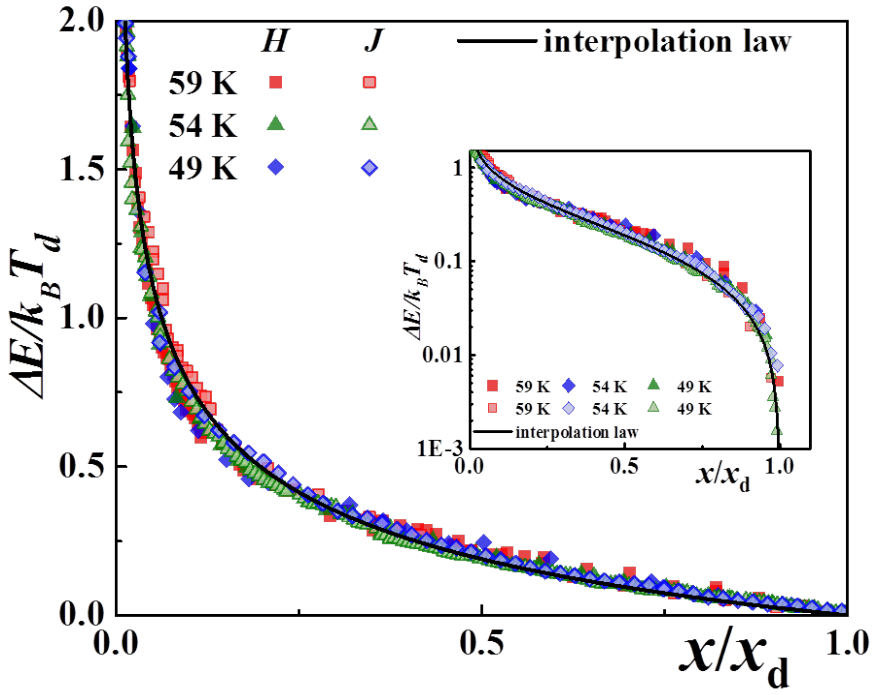

Figure 6.8: **Universal energy barrier height.** Reduced energy barrier height $\Delta E/k_bT_d$ is a function of reduced driving forces x/x_d: magnetic field H/H_d (solid symbols) and current density J/J_d (empty symbols). The solid curve is a plot of equation 6.3 with $\mu_H = \mu_J = 1/4$. Inset: Universal barrier presented in semi-log scale presenting a good agreement over 3 orders of magnitude.

"the shape of the mountains is developed by the pinning of DWs at several strong pinning sites", which "suggests that the DW responds differently to pinning sites depending on what the driving force is." Let us now discuss these issues.

From the values of the effective energy barrier heights k_BT_d, we can extract statistical information of the pinning disorder. Indeed, k_BT_d reflects an average of the barriers over all the pinning sites covered by the DW during it's motion. As it can be observed in Table 6.1, the values of k_BT_d are pretty similar for magnetic field and current density DW motion. This suggests that the same statistical disorder controls both current and field driven DW motion. In other words, no difference is observed in the response of DW due to pinning disorder for the DWs aligned perpendicular to the direction of current.

For the formation of facets, figure 6.1 suggests that the "strong pinning centers" play an important role. Here, we show that the formation of facets may occur without any contribution of "strong" pinning centers. Let us consider the experiment summarized in Fig. 6.9.

We start from straight DWs with a normal direction $\vec{n}$ submitted to a current density $\vec{J}$ (see Fig. 6.9 (E)). The tilting angle θ is defined by $cos\theta = \vec{n} \cdot \vec{J}/J$. The depinning

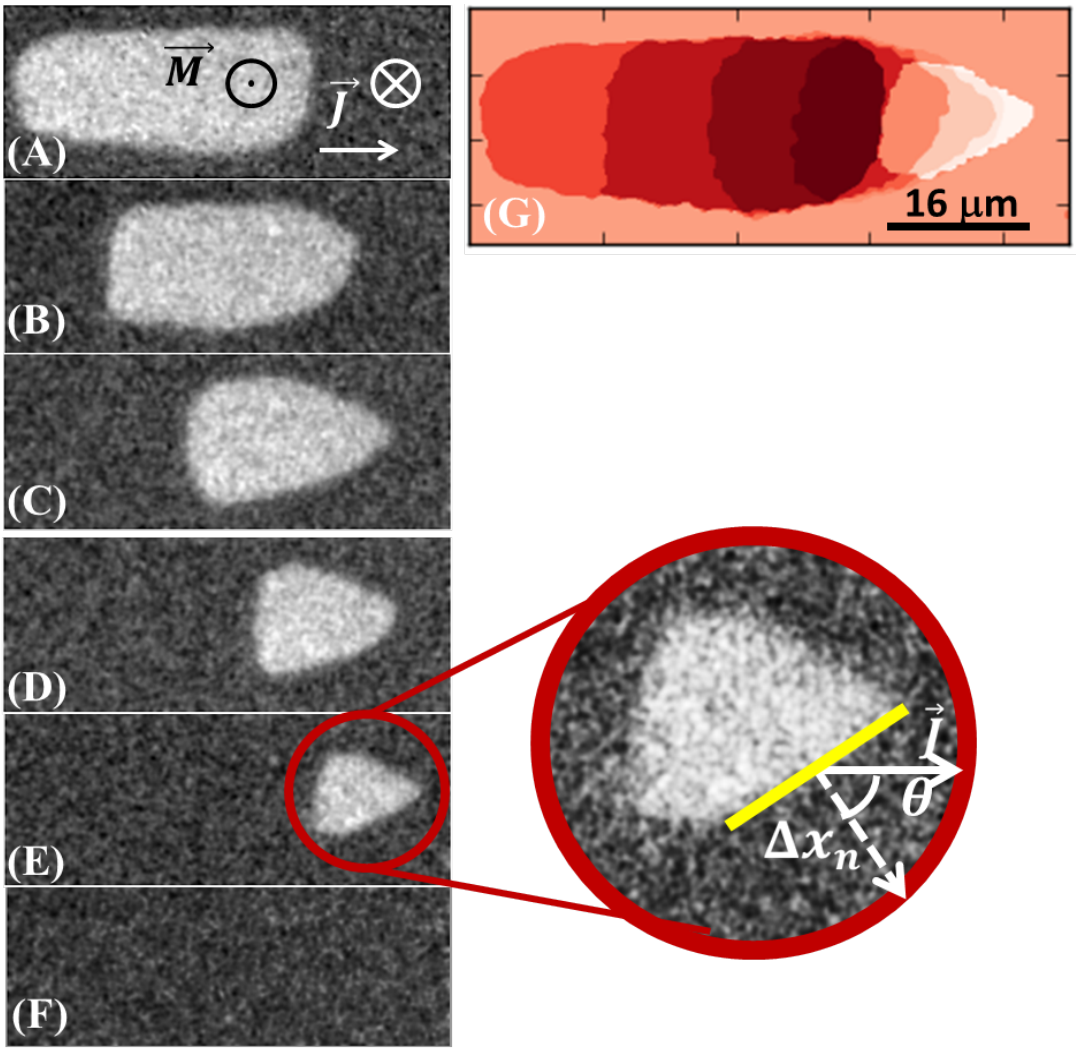

Figure 6.9: **Facet formation and critical angle.** Time evolution of an initialy almost rectangular domain (A) driven by pulses of current density of amplitude $J = 11.2GA/m^2$ and duration $\Delta t = 6\mu s$ in the direction shown by the arrow. Figs. (B-E) show the successive domain shapes after 1, 2, 3, and 4 pulses, respectively. Figs. (F-G) show the superposition of all the DW shapes. The DW on the left, whose normal direction remains close to the direction of the current, presents similar displacements after each current pulse (see shades of blue in F). For the front of the rectangle, the tilting of DW increases (see shades of red in G) without any contribution of a "strong" pinning site. At a maximum tilting angle $\approx 50°$ (see the indications in Fig. E), the DW is stopped. The difference between the velocities of the back and the front DWs causes the collapse of the domain (not shown). This experiment was done at $T = 45K$, the effective depinning current is $J_C = 8.4 \pm 0.6GA/m^2$

condition for the DW can be deduced from a balance between a pinning force $\overrightarrow{f}_d$ and a driving force $\overrightarrow{f}_j$. The pinning force $\overrightarrow{f}_d$ acts in the direction opposite to DW displacement and is proportional to the effective depinning current density J_C: $\overrightarrow{f}_d \sim -J_C \overrightarrow{n}$. The

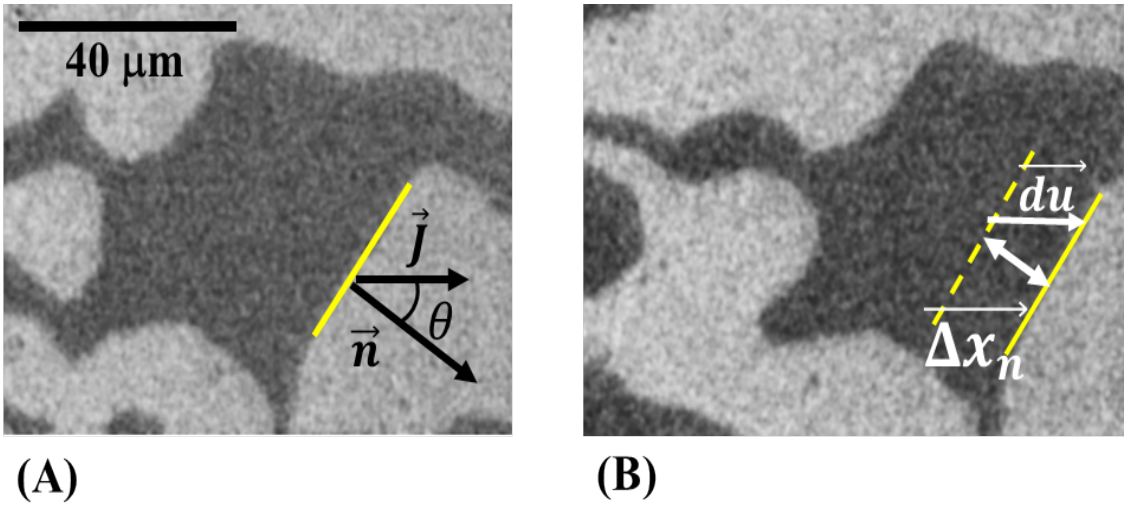

Figure 6.10: **DW displacement along the current direction.** Two successive images of domains driven by an homogenous DC current ($J = 11.1GA/m^2$). We show in (A) the DW normal in comparison with the direction of the current and the angle θ between the two. (B) The successive image after applying a $J = 11.1GA/m^2$ current pulse of duration $\Delta t = 1\mu m$. We show the displacement along the direction of the current.

contribution of the electrical current is proportional to the torque exerted by STT [103], $\vec{f}_j \sim \vec{J}$.

In this simple model, the variation of STT efficiency is neglected with the tilting angle [102]. In the direction $\vec{n}$, the tilting of the DW reduces the driving force ($\sim Jcos\theta$). As a small tilting is sufficient to reduce the DW velocity, therefore the DW orientation such that it's normal is parallel to the current ($\vec{n} \parallel \vec{J}$) is unstable, i.e., no strong pinning center is required to trigger the instability. Moreover, for a fixed bias current density J, there is a critical angle θ_C defined by $cos\theta_C = J_C/J$ above which the driving current is not sufficient to overcome the pinning so that DW cannot move. This scenario is in qualitative agreement with the experimental observations reported in Fig. 6.9.

In order to discuss the issues presented above in quantitative terms, we measure the DW displacements (Δx_n) in the direction $\vec{n}$ as a function of the tilting angle θ for a set of images as it is shown in figure 6.10. The displacements along the direction parallel to the current $\vec{J}$ and to the DW normal $\vec{n}$ are shown in figure 6.11 (A). We observe that the displacement u in the direction of the current does not fluctuate from the main value more than $\sim 2\mu m$. In contrast, when we plot the displacement Δx_n along the DW normal, we observe a behavior that resembles a linear decrease with the tilting angle.

In figure 6.11 (B) we show the displacement (Δx_n) in the direction of $\vec{n}$ varying with the difference between the cosine of the tilting angle θ and the cosine of the limit angle θ_C. We observe that we can fit a straight line for the experimental curve. This result supports the hypothesis that the force excreted over the DW behaves like the dot product

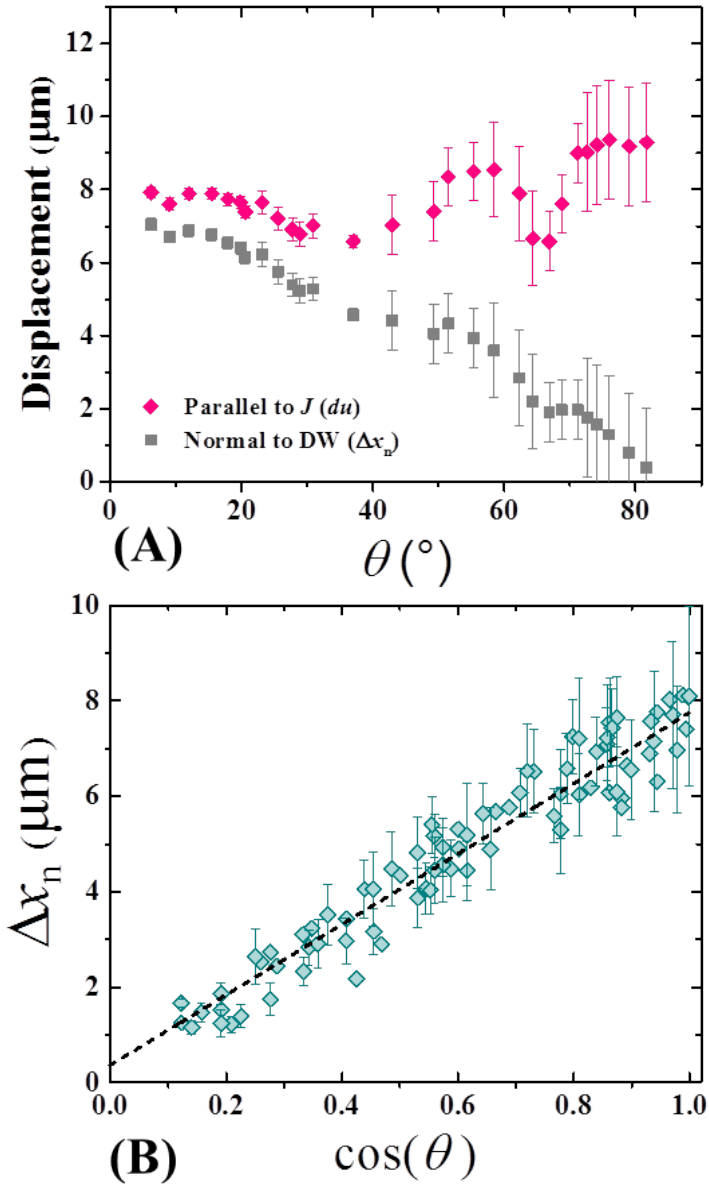

Figure 6.11: **DW displacement along the current and the DW normal direction.** (A) For the experiment shown in figure 6.10, we plot the DW's displacement parallel to the current density's direction $\overrightarrow{du}$ (pink diamonds) and normal to the DW $\overrightarrow{\Delta x_n}$ (gray squares) *vs* the local tilting angle θ between the current density $\overrightarrow{J}$ and the normal to the DW $\overrightarrow{n}$. (B) Displacement of tilted DWs Δx_n *vs* local tilting angle cosine $cos(\theta)$. The dotted line is a linear fit of the experimental points.

of the current and the DWs normal ($f \sim \overrightarrow{J} \cdot \overrightarrow{n}$). The driving force can be written as $f = F_{ext}(J)cos\theta$.

Moreover, for small tilting angles, we can write $tg\theta \simeq \theta \simeq \frac{du}{dx}$ and $cos\theta \simeq 1 - \theta^2/2$, and thus $f \simeq F_{ext}(1 - \frac{1}{2}\left(\frac{\partial u}{\partial x}\right)^2)$. At the zero order in tilting angle θ, the force is simply $f = F_{ext}$ and the current driven DW motion can be described by the q-EW equation. At second order, i.e. $f \simeq F_{ext}(1 - \frac{1}{2}\left(\frac{\partial u}{\partial x}\right)^2)$ the equation of motion can be written as:

$$\eta\frac{\partial u}{\partial t} = c\frac{\partial^2 u}{\partial^2 x} + F_{pin} + \chi + F_{ext} - \frac{F_{ext}}{2}\left(\frac{\partial u}{\partial x}\right)^2, \tag{6.4}$$

which corresponds to negative q-KPZ model with $\lambda = \frac{F_{ext}}{2}$. For higher tilting angles the motion equation should take into account the full cosine variation of the force. Neither q-EW nor negative q-KPZ model may describe accurately current induced DW motion for large tilting angle.

6.4 Chapter summary

We made an exhaustive study of two critical exponents: the roughness ζ and creep exponent μ on the same sample for both magnetic field and current induced DW motion. In both cases we obtained very close values for the two driving forces, as it is shown in table 6.2.

Driving force	**Roughness exponent ζ**	**Creep exponent μ**
H	0.60 ± 0.04	0.247 ± 0.011
J	0.61 ± 0.10	0.259 ± 0.004

Table 6.2: **Critical exponents.** Average roughness exponents ζ_H and ζ_J over a wide range of temperatures and creep exponents μ_H and μ_J obtained from fitting the creep law.

The obtained critical exponents for magnetic field DW motion $\mu_H = 0.247 \pm 00.011$ and $\zeta_H = 0.60 \pm 0.04$ are in very good agreement with the theoretical predictions for the quenched Edward-Wilkinson universality class with anharmonic corrections on the elasticity, and with previous experimental results reported in [76, 31].

On the other hand, the critical exponents obtained for current induced DW motion are in good agreement with the theoretical predictions for the Edward-Wilkinson universality class. However they strongly disagree with previous experimental results. The current driven roughness exponent obtained by Moon et al. in ref [76] (ζ_J(Moon)$= 0.99 \pm 0.01$) agrees with the roughness exponent obtained by simulations for negative KPZ universality class($\zeta_{negqKPZ} \sim 1$) [75]. We measured a smaller roughness exponent ($\zeta_J = 0.61 \pm 0.10$). This is in better agreement with the one measured by Moon et al. in the direction of the DW normal ($\zeta_{J\perp} = 0.69 \pm 0.04$). The main difference between our experiment and theirs is that the limit faceting angle in our sample is much smaller ($45° \pm 7°$) in comparison with the one measured in Pt/Co/Pt ($> 80°$) caused mainly by the interaction between the DW elasticity and the directionality of the applied current density.

The obtained current driven creep exponent ($\mu_J = 0.259 \pm 0.004$) disagrees with the one measured by DuttaGupta *et al.* (μ_J(DuttaGupta)$= 0.39 \pm 0.06$) [31]. We covered a wider range of orders of magnitude for the current induced DW velocity and we were able to observe the end of the creep regime in the v *vs* J curves, which is not observable in the experiment performed in reference [31]. We also determined empirically the temperature rise due to the current flow in our device. In every case (for the current densities and pulse durations used throughout the entire v *vs* J curves) we determined that ΔT is negligible for the velocity *vs* driving force x measurements.

As a conclusion of this section, we observe that for small faceting angles in the case of current driven DW motion we recover the Edward-Wilkinson universality class with short range elasticity and pinning disorder, as in the well known case of magnetic driven DW motion.

CHAPTER 7

Conclusions and perspectives

"Everything has to come to an end, sometime."

L. Frank Baum, The Marvelous Land of Oz.

This thesis explores the universal behaviors of magnetic domain wall (DW) dynamics in thin ferromagnetic films with perpendicular anisotropy. In this section we summarize the main conclusions of the explored subjects.

7.1 Depinning transition.

We have studied the universal behaviors of the depinning transition. The DW velocity in a Pt/Co/Pt film was measured in the range of almost two magnitude orders in temperature, and over a magnetic field range covering the creep, depinning, and precessional flow regimes. Our results were compared to data taken from the literature for Au/Co/Au and CoFeB films. The DW dynamics was shown to be compatible with the predicted power law variations for the velocity and predicted universal exponents ($\psi = 0.15$, and $\beta = 0.25$).

In order to go beyond the usual critical exponent analysis, we have constructed a self-consistent model describing both the creep and depinning regimes. This model allows distinguishing, accurately, universal from non-universal behaviors. In particular, we were

able to extract the universal function of the depinning transition, catching both thermal and drive effects on the domain wall velocity.

Moreover, the whole glassy dynamics (including both regimes) was shown to rely only on three material and temperature dependent pinning parameters (H_d, v_T and T_d), and on two universal functions.

Therefore, the universal behavior of domain wall dynamics covers the creep and depinning regimes, i.e., from zero drive up to an upper boundary, which was found to be non-universal. Over this magnetic field range, the dynamics can be described by the competition between disorder, thermal activation, and elasticity and, therefore, it belongs to the quenched Edwards-Wilkinson universality class.

Perspectives

The clear discrimination between universal and non-universal behaviors opens new perspectives for a better understanding of pinning effects on the glassy dynamics. Indeed, our work suggests that variations of the material pinning properties should only manifest through the variations of effective pinning parameters (H_d, v_T, and T_d).

More precisely, it would be particularly interesting to explore the correlations between the effective pinning parameters, the micromagnetic parameters (the saturation magnetization, domain wall surface energy and thickness parameter and the Gilbert damping factor), and the microscopic pinning parameters characterizing the weak pinning disorder (the pinning strength and correlation length of the disorder). For example, obtaining an estimation of the microscopic pinning parameters, which are not directly accessible experimentally, would be particularly valuable for the understanding of the He^+ and Ga^+ ion irradiation effects on domain wall pinning.

Moreover, a recent topic is the contribution of the Dzyaloshinskii-Moriya interaction and of chirality of domain walls on their dynamics. Results published in the literature suggest that the universal behavior of the creep motion is conserved [50, 54], or used [59, 65], to accurately describe the data. In particular, the creep exponent μ remains equal to 1/4, which means that there is no change of universality class due to chirality. Therefore, our analysis, which is based on this universal behavior can be used to analyze the motion of chiral domain walls. In particular, it would be interesting to study the variation of effective pinning parameters with an in-plane magnetic field, which modifies the magnetic structure of domain walls, typically neglected in the $1d$ elastic line model.

7.2 Dimensional crossover

We have analyzed finite size effects on domain wall motion for (Ga,Mn)As and (Ga,Mn)(As,P) magnetic films of different thicknesses ranging between 12 and 80 nm. The DW dynamics and the roughness exponent were measured as a function of the applied magnetic field, for different temperatures. Velocity and roughness measurement are observed to present discontinuities for the same magnetic field thresholds. Below threshold, the motion is compatible with the exponents ($\mu = 1/4$, $\zeta_{eq} = 2/3$ and $\zeta_{dep}(anh) = 0.63$) predicted for the motion of an elastic line moving in a two dimensional medium. Above threshold the results are compatible with the exponents ($\mu = 1/2$, $\zeta_{eq} = 2/5$ and $\zeta_{dep}(anh) = 0.45$) corresponding to the motion of a surface in three dimensional medium.

This change of criticality is expected since the effective domain wall dimensionality depends on the respective values of the film thickness and optimal length-scale (L_{opt}), which decreases with increasing magnetic field. Below (Above) a magnetic field threshold, the optimal length-scale is larger (smaller) than the film thickness and the domain wall to behave as an elastic line (surface) in a two (three) dimensional medium.

We therefore evidenced a creep motion in three dimensions and a dimensional crossover of the domain wall dynamics.

Perspectives

As a perspective, it would be interesting to study the depinning transition of thick films. At zero temperature, the typical length-scale of the avalanches is predicted to diverge [95] and then to decrease as the applied magnetic field is increased. This could lead to a dimensional crossover of the depinning transition [95].

7.3 Current driven domain wall motion

We have addressed the controversy on criticality of current driven domain wall motion. We performed a compared analysis of current and magnetic field driven domain wall motion in (Ga,Mn)(As,P) films. We showed that the essential difference between the two drives is the directionality of the driving force. A magnetic field acts as an isotropic pressure. In contrast, when we apply an electric current, we show that the driven force is proportional to the scalar product between the current density and the vectors normal to domain wall. This directionality results in the formation of faceted DWs.

For a non-zero tilting angle, we showed that the equation of motion can be written as Kardar-Parisi-Zhang minimal model. For a zero tilting angle, the critical exponents are

similar to those obtained for magnetic field induced domain wall motion. Therefore, this indicates that the current driven dynamics can be described by the quenched Edwards-Wilkinson equation of motion.

Perspectives

This work shows that the directionality of force associated to the spin transfer torque plays an important role in a universal behaviors. It would be interesting to extend the those results to other torques, such as the spin Hall torque [104]. Another interesting topic is the simultaneous bias with magnetic field and current. The control of domain wall motion would allow comparing the magnitude of the force associated to a current, and to magnetic field.

Last, we show evidences of the transient creep regime. The transient creep is also observed in other experiments (see Yamanouchi *et al.* [112], for example). The transient creep has important implications for potential application based on the controlled motion of domain walls. However, the physics of transient creep is largely ignored.

List of publications

- **R. Díaz Pardo**, W. Savero Torres, A. B. Kolton, S. Bustingorry, and V. Jeudy. *Universal depinning transition of domain walls in ultrathin ferromagnets.* Physical Review B, 95(18):184434, 2017.
- Nirvana B. Caballero, Iván Fernández Aguirre, Lucas J. Albornoz, Alejandro B. Kolton, Juan Carlos Rojas-Sánchez, Sophie Collin, Jean Marie George, **Rebeca Díaz Pardo**, Vincent Jeudy, Sebastián Bustingorry, Javier Curiale. *Excess velocity of magnetic domain walls close to the depinning field.* Physical Review B, 96 (22): 224422, 2017.
- Vincent Jeudy, **Rebeca Díaz Pardo**, Williams Savero Torres, Sebastian Bustingorry, Alejandro Kolton. *Pinning of Domain Walls in thin Ferromagnetic Films.* Physical Review B, 98 (5): 2054406, 2017.

List of Figures

List of Tables

Index

Bibliography

[1] H. E. Stanley A.- L. Barabási. *Fractal concepts in surface growth*. Cambridge University Press, Cambridge, 1995.

[2] R. Schäfer A. Hubert. *Magnetic Domains. The analysis of magnetic nanostructures*. Springer Verlag, 2009.

[3] J. P. Adam. *Du renversement sous champ de l'aimantation d'un nano-plot au déplacement sous courant d'une paroi de domaines dans une nano-piste par microscopie Kerr polaire*. PhD thesis, Université Paris-Sud, 2008.

[4] J. P. Adam, N. Vernier, J. Ferré, A. Thiaville, V. Jeudy, A. Lemaître, L. Thevenard, and G. Faini. Nonadiabatic spin-transfer torque in (Ga,Mn)As with perpendicular anisotropy. *Physical Review B - Condensed Matter and Materials Physics*, 80(19):2–5, 2009.

[5] N. W. Ashcroft and Mermin N. D. *Solid state physics*, volume lll. New York, 1976.

[6] G.S.D. Beach, C. Nistor, C. Knutson, M. Tsoi, and J. L. Erskine. Dynamics of field-driven domain-wall propagation in ferromagnetic nanowires. *Nature Materials*, 4(10):741–744, 2005.

[7] G. Blatter, M. V. Feigel'Man, V. B. Geshkenbein, A. I. Larkin, and V. M. Vinokur. Vortices in high-temperature superconductors. *Reviews of Modern Physics*, 66(4):1125–1388, 1994.

[8] F. Bohn, G. Durin, M. A. Correa, N. Machado, R. Della Pace, C. Chesman, and R. L. Sommer. Playing with universality classes of Barkhausen avalanches. *arXiv:1801.09948v2*, pages 1–16, 2018.

[9] C. Burrowes, N. Vernier, J. P. Adam, L. Herrera Diez, K. Garcia, I. Barisic, G. Agnus, S. Eimer, J. V. Kim, T. Devolder, A. Lamperti, R. Mantovan, B. Ockert, E. E. Fullerton, and D. Ravelosona. Low depinning fields in Ta-CoFeB-MgO ultrathin films with perpendicular magnetic anisotropy. *Applied Physics Letters*, 103(18), 2013.

[10] S. Bustingorry, A. B. Kolton, and T. Giamarchi. Thermal rounding of the depinning transition. *European Physics Letters*, 81(16):260005, 2008.

[11] S. Bustingorry, A. B. Kolton, and T. Giamarchi. Thermal rounding exponent of the depinning transition of an elastic string in a random medium. *Physical Review E - Statistical, Nonlinear, and Soft Matter Physics*, 85(2):1–9, 2012.

[12] S. Bustingorry, A. B. Kolton, and T. Giamarchi. Thermal rounding of the depinning transition in ultrathin Pt/Co/Pt films. *Physical Review B - Condensed Matter and Materials Physics*, 85(21):1–7, 2012.

[13] J. Cardy. *Scaling and Renormalization in Statistical Physics*. Cambridge University Press, Cambridge, 1996.

[14] P. Chauve, T. Giamarchi, and P. Le Doussal. Creep and depinning in disordered media. *Physical Review B - Condensed Matter and Materials Physics*, 62(10):6241–6267, 2000.

[15] D. Chiba, Y. Sato, T. Kita, F. Matsukura, and H. Ohno. Current-Driven Magnetization Reversal in a Ferromagnetic Semiconductor (Ga,Mn)As/GaAs/(Ga,Mn)As Tunnel Junction. *Physical Review Letters*, 93(21):216602, 2004.

[16] P. Cizeau, S. Zapperi, G. Durin, and E. H. Stanley. Dynamics of a ferromagnetic domain wall and the barkhausen effect. *Physical Review B - Condensed Matter and Materials Physics*, 58(10):6353–6366, 1998.

[17] G. Coupier, C. Guthmann, Y. Noat, and M. S. Jean. Local symmetries and order-disorder transitions in small macroscopic Wigner islands. *Physical Review E - Statistical, Nonlinear, and Soft Matter Physics*, 71(4):1–12, 2005.

[18] B. D. Cullity and C. D. Graham. *Introduction to magnetic materials*. Wiley, IEEE Press, New Jersey, 2nd edition, 2009.

[19] J. Curiale, A. Lemaître, G. Faini, and V. Jeudy. Track heating study for current-induced domain wall motion experiments. *Applied Physics Letters*, 97(24):1–3, 2010.

[20] J. Curiale, A. Lemaître, C. Ulysse, G. Faini, and V. Jeudy. Spin drift velocity, polarization, and current-driven domain-wall motion in (Ga,Mn)(As,P). *Physical Review Letters*, 108(7):1–5, 2012.

[21] E. D. Daniel, C. Denis Mee, and M. H. Clark. *Magnetic Recording: the first 100 years*. Wiley-IEEE Press, 1998.

[22] R. Díaz Pardo, W. Savero Torres, A. B. Kolton, S. Bustingorry, and V. Jeudy. Universal depinning transition of domain walls in ultrathin ferromagnets. *Physical Review B*, 95(18):184434, 2017.

[23] T. Dietl and H. Ohno. Dilute ferromagnetic semiconductors: Physics and spintronic structures. *Reviews of Modern Physics*, 86(1):187–251, 2014.

[24] T. Dietl, H. Ohno, and F. Matsukura. Hole-mediated ferromagnetism in tetrahedrally coordinated semiconductors. *Physical Review B - Condensed Matter and Materials Physics*, 63(19), 2001.

[25] A. Dourlat. *Propriétés magnétiques statiques et dynamiques de couches minces de GaMnAs à anisotropie perpendiculaire*. PhD thesis, Université Pierre et Marie Curie-Paris 6, 2008.

[26] A. Dourlat, V. Jeudy, A. Lemaître, and C. Gourdon. Field-driven domain-wall dynamics in (Ga,Mn)As films with perpendicular anisotropy. *Physical Review B - Condensed Matter and Materials Physics*, 78(16):2–5, 2008.

[27] A. Dourlat, V. Jeudy, A. Lemaître, and C. Gourdon. Field-driven domain-wall dynamics in (Ga,Mn)As films with perpendicular anisotropy. *Physical Review B - Condensed Matter and Materials Physics*, 78(16):2–5, 2008.

[28] A. Dourlat, V. Jeudy, C. Testelin, F. Bernardot, K. Khazen, C. Gourdon, L. Thevenard, L. Largeau, O. Mauguin, and A. Lemaître. Domain structure and magnetic anisotropy fluctuations in (Ga,Mn)As: Effect of annealing. *Journal of Applied Physics*, 102(2), 2007.

[29] R. A. Duine and C. Morais Smith. Creep of current-driven domain-wall lines: Effects of intrinsic versus extrinsic pinning. *Physical Review B - Condensed Matter and Materials Physics*, 77(9):1–6, 2008.

[30] G. Durin and S. Zapperi. Scaling exponents for barkhausen avalanches in polycrystalline and amorphous ferromagnets. *Physical Review Letters*, 84(20):4705–4708, 2000.

[31] S. DuttaGupta, S. Fukami, C. Zhang, H. Sato, M. Yamanouchi, F. Matsukura, and H. Ohno. Adiabatic spin-transfer-torque-induced domain wall creep in a magnetic metal. *Nature Physics*, 12(4):333–336, 2015.

[32] K. Edmonds, G. Van Der Laan, and G. Panaccione. Electronic structure of (Ga,Mn)As as seen by synchrotron radiation. *Semiconductor Science and Technology*, 30(4), 2015.

[33] F. Family and T. Vicsek. Scaling of the active zone in the Eden process on percolation networks and the ballistic deposition model. *Journal of Physics A: Mathematical and General*, 18(2):L75–L81, 1985.

[34] M. Farle. Ferromagnetic resonance of ultrathin metallic layers. *Reports on Progress in Physics*, 61:755–826, 1998.

[35] E. E. Ferrero, S. Bustingorry, and A. B. Kolton. Nonsteady relaxation and critical exponents at the depinning transition. *Physical Review E - Statistical, Nonlinear, and Soft Matter Physics*, 87(3):1–14, 2013.

[36] E. E. Ferrero, S. Bustingorry, A. B. Kolton, and A. Rosso. Numerical approaches on driven elastic interfaces in random media. *Comptes Rendus Physique*, 14(8):641–650, 2013.

[37] E. E. Ferrero, L. Foini, T. Giamarchi, A.B. Kolton, and A. Rosso. Spatiotemporal Patterns in Ultraslow Domain Wall Creep Dynamics. *Physical Review Letters*, 118(14), 2017.

[38] A. Fert, V. Cros, and J. Sampaio. Skyrmions on the track. *Nature Nanotechnology*, 8(3):152–156, 2013.

[39] D. S. Fisher. Sliding charge-density waves as a dynamical critical phenomenon. *Phys. Rev. B*, 31(3):1396–1427, 1985.

[40] T Giamarchi, A B Kolton, and A Rosso. Dynamics of disordered elastic systems. In M. C. Miguel Rubi and J. M., editors, *Jamming, Yielding and Irreversible deformation in condensed matter*, pages 91–107. Springer Berlin Heidelberg, 2005.

[41] T. L. Gilbert. Classics in Magnetics A Phenomenological Theory of Damping in Ferromagnetic Materials. *IEEE Transactions on Magnetics*, 40(6):3443–3449, 2004.

[42] R. B. Goldfarb and F. R. Fickett. Units for magnetic properties, 1999.

[43] J. Gorchon. *Current and field induced magnetization reversal in Pt/Co/Pt and (Ga,Mn)(As,P) ferromagnetic films.* PhD thesis, Université Paris-Sud, 2014.

[44] J. Gorchon, S. Bustingorry, J. Ferré, V. Jeudy, A. B. Kolton, and T. Giamarchi. Pinning-dependent field-driven domain wall dynamics and thermal scaling in an ultrathin Pt/Co/Pt magnetic film. *Physical Review Letters*, 113(2):1–5, 2014.

[45] J. Guyonnet, E. Agoritsas, S. Bustingorry, T. Giamarchi, and P. Paruch. Multiscaling analysis of ferroelectric domain wall roughness. *Physical Review Letters*, 109(14):1–5, 2012.

[46] W. Heisenberg. Zur Theorie des Ferromagnetismus. *Zeitschrift fur Physik*, 49(9-10):619–636, 1928.

[47] L. Herrera Diez, V. Jeudy, G. Durin, A. Casiraghi, Y. T. Liu, M. Voto, G. Agnus, D. Bouville, L. Villa, J. Langer, B. Ocker, L. Lopez-Diaz, and D. Ravelosona. Wire edge dependent magnetic domain wall creep. *Submitted to Physical Review B - Condensed Matter and Materials Physics*, 2018.

[48] A. Hrabec, J. Sampaio, M. Belmeguenai, I. Gross, R. Weil, S. M. Chérif, A. Stashkevich, V. Jacques, A. Thiaville, and S. Rohart. Current-induced skyrmion generation and dynamics in symmetric bilayers. *Nature Communications*, 8:1–6, 2017.

[49] T. Ishii, T. Kawazoe, Y. Hashimoto, H. Terada, I. Muneta, M. Ohtsu, M. Tanaka, and S. Ohya. Electronic structure near the Fermi level in the ferromagnetic semiconductor GaMnAs studied by ultrafast time-resolved light-induced reflectivity measurements. *Physical Review B*, 93(24):2413031–4, 2016.

[50] S. G. Je, D. H. Kim, S. C. Yoo, B. C. Min, K. Ji. Lee, and S. B. Choe. Asymmetric magnetic domain-wall motion by the Dzyaloshinskii-Moriya interaction. *Physical Review B - Condensed Matter and Materials Physics*, 88(21):1–5, 2013.

[51] V. Jeudy, A. Mougin, S. Bustingorry, W. Savero Torres, J. Gorchon, A. B. Kolton, A. Lemaître, and J. P. Jamet. Universal Pinning Energy Barrier for Driven Domain Walls in Thin Ferromagnetic Films. *Physical Review Letters*, 117(5):1–5, 2016.

[52] Vincent Jeudy, Rebeca Díaz Pardo, Williams Savero Torres, Sebastian Bustingorry, and Alejandro Kolton. Pinning of Domain Walls in thin Ferromagnetic Films. *Physical Review B - Condensed Matter and Materials Physics*, 054406:1–11, 2018.

[53] J. Y. Jo, S. M. Yang, T. H. Kim, H. N. Lee, J. G. Yoon, S. Park, Y. Jo, M. H. Jung, and T. W. Noh. Nonlinear dynamics of domain-wall propagation in epitaxial ferroelectric thin films. *Physical Review Letters*, 102(4), 2009.

[54] E. Jué, C. K. Safeer, M. Drouard, A. Lopez, P. Balint, L. Buda-Prejbeanu, O. Boulle, S. Auffret, A. Schuhl, A. Manchon, I.M. Miron, and G. Gaudin. Chiral damping of magnetic domain walls. *Nature Materials*, 15(3):272–277, 2016.

[55] M. Kardar, G. Parisi, and Y. C. Zhang. Dynamic scaling of growing interface. *Physical Review Letters*, 56(1):1–4, 1986.

[56] D. R. Kardar, M., Nelson. Commensurate-incommensurate transitions with quenched random impurities. *Physical Review Letters*, 55(11):1157–1160, 1985.

[57] J. Kerr. On Rotation of the Plane of Polarization by reflectlon from the Pole of a Magnet. *Philosophical Magazine and Journal of Science*, 3(19):321–343, 1877.

[58] K. J. Kim, J. C. Lee, S. M. Ahn, K. S. Lee, C. W. Lee, Y. J. Cho, S. Seo, K. H. Shin, S. B. Choe, and H. W. Lee. Interdimensional universality of dynamic interfaces. *Nature*, 458(7239):740–742, 2009.

[59] K. W. Kim, H. W. Lee, K. Ji. Lee, K. Everschor-Sitte, O. Gomonay, and J. Sinova. Roles of chiral renormalization on magnetization dynamics in chiral magnets. *Physical Review B*, 97(10):1–6, 2018.

[60] A. Kirilyuk, J. Ferré, V. Grolier, J. P. Jamet, and D. Renard. Magnetization reversal in ultrathin ferromagnetic films with perpendicular anisotropy. *Journal of Magnetism and Magnetic Materials*, 171(1-2):45–63, 1997.

[61] C. Kittel. *Introduction to Solid State Physics*. John Wiley & Sons, Inc, United States of America, 8th edition, 1957.

[62] M. Kläui, C. A. F. Vaz, J. A. C. Bland, W. Wernsdorfer, G. Faini, E. Cambril, and L. J. Heyderman. Domain wall motion induced by spin polarized currents in ferromagnetic ring structures. *Applied Physics Letters*, 83(1):105–107, 2003.

[63] A. B. Kolton, A. Rosso, T. Giamarchi, and W. Krauth. Creep dynamics of elastic manifolds via exact transition pathways. *Physical Review B - Condensed Matter and Materials Physics*, 79(18):1–13, 2009.

[64] L. D. Landau and E. M. Lifshitz. *Theory of Elasticity*. Pergamon Press, New York, 2nd edition, 1975.

[65] R. Lavrijsen, D. M F Hartmann, A. Van Den Brink, Y. Yin, B. Barcones, R. A. Duine, M. A. Verheijen, H. J M Swagten, and B. Koopmans. Asymmetric magnetic bubble expansion under in-plane field in Pt/Co/Pt: Effect of interface engineering. *Physical Review B - Condensed Matter and Materials Physics*, 91(10):1–16, 2015.

[66] V. Lecomte, S. E. Barnes, J. P. Eckmann, and T. Giamarchi. Depinning of domain walls with an internal degree of freedom. *Physical Review B - Condensed Matter and Materials Physics*, 80(5):1–5, 2009.

[67] J. C. Lee, K.-J. Kim, J. Ryu, K.-W. Moon, S.-J. Yun, G. H. Gim, K.-So. Lee, K.H. Shin, H.W. Lee, and S. B. Choe. Universality Classes of Magnetic Domain Wall Motion. *Physical Review Letters*, 107(6):067201, 2011.

[68] A. Lemaître, A. Miard, L. Travers, O. Mauguin, L. Largeau, C. Gourdon, V. Jeudy, M. Tran, and J. M. George. Strain control of the magnetic anisotropy in (Ga,Mn) (As,P) ferromagnetic semiconductor layers. *Applied Physics Letters*, 93(2):0211231–3, 2008.

[69] S. Lemerle. *Etude de la dynamique de renversement de l'aimantation dans les couches ultra-minces à anisotropie perpendiculaire: rôle de la nanostructure*. PhD thesis, Université Paris Sud, 1998.

[70] S. Lemerle, J. Ferré, C. Chappert, V. Mathet, T. Giamarchi, and P. Le Doussal. Domain Wall Creep in an Ising Ultrathin Magnetic Film. *Physical Review Letters*, 80(4):849–852, 1998.

[71] J. M. López and J. Schmittbuhl. Anomalous scaling of fracture surfaces. *Physical Review E - Statistical Physics, Plasmas, Fluids, and Related Interdisciplinary Topics*, 57(6):6405–6408, 1998.

[72] A. P. Malozemoff and J. C. Slonczewski. *Magnetic Domain Walls in Bubble Materials*. Academic Press, New York, 1979.

[73] P. J. Metaxas, J. P. Jamet, A. Mougin, M. Cormier, J. Ferré, V. Baltz, B. Rodmacq, B. Dieny, and R. L. Stamps. Creep and flow regimes of magnetic domain-wall motion in ultrathin Pt/Co/Pt films with perpendicular anisotropy. *Physical Review Letters*, 99(21):1–4, 2007.

[74] A. Middleton. Thermal rounding of the charge-density-wave depinning transition. *Physical Review B - Condensed Matter and Materials Physics*, 45(16):9465–68, 1992.

[75] B. Moglia, E. Albano, P. Villegas, and M. Muñoz. Interfacial depinning transitions in disordered media: revisiting an old puzzle. *Journal of Statistical Mechanics: Theory and Experiment*, 2014(10):P10024, 2014.

[76] K. W. Moon, D. H. Kim, S. C. Yoo, C. G. Cho, Hwang S., B. Kahng, Min B. C., Shin K. H., and Choe S. Distinct universality classes of domain wall roughness in two-dimensional Pt/Co/Pt films. *Physical Review Letters*, 110(10):1–5, 2013.

[77] A. Mougin, M. Cormier, J. P. Adam, P. J. Metaxas, and J. Ferré. Domain wall mobility, stability and Walker breakdown in magnetic nanowires. *European Physics Letters*, 78(57007):1–6, 2007.

[78] S. Moulinet, A. Rosso, W. Krauth, and E. Rolley. Width distribution of contact lines on a disordered substrate. *Physical Review E - Statistical, Nonlinear, and Soft Matter Physics*, 69(3 2):1–4, 2004.

[79] M. Myllys, J. Maunuksela, M. J. Alava, T. Ala-Nissila, and J. Timonen. Scaling and Noise in Slow Combustion of Paper. *Physical Review Letters*, 84(9):1946–1949, 2000.

[80] T. Nattermann. Interface Roughening in Systems with Quenched Random Impurities. *Europhysics Letters*, 4(11):1241–1243, 1987.

[81] T. Nattermann, Y. Shapir, and I. Vilfan. Interface pinning and dynamics in random systems. *Physical Review B*, 42(13):8577–8586, 1990.

[82] T. Niazi, M. Cormier, D. Lucot, L. Largeau, V. Jeudy, J. Cibert, and A. Lemaître. Electric-field control of the magnetic anisotropy in an ultrathin (Ga,Mn)As/(Ga,Mn)(As,P) bilayer. *Applied Physics Letters*, 102(12), 2013.

[83] J. Okabayashi, A. Kimura, O. Rader, T. Mizokawa, A. Fujimori, T. Hayashi, and M. Tanaka. Core-level photoemission study of GaMnAs. *Physical Review B - Condensed Matter and Materials Physics*, 58(8):4211–4214, 1998.

[84] F. Schutz P. Kopietz, L. Bartosch. *Introduction to functional renormalization group theory*. Springer, Berlin Heidelberg, 2010.

[85] P. Paruch, A. B. Kolton, X. Hong, C. H. Ahn, and T. Giamarchi. Thermal quench effects on ferroelectric domain walls. *Physical Review B - Condensed Matter and Materials Physics*, 85(21):1–7, 2012.

[86] R. K. Pathria and P. D. Beale. *Statistical Mechanics*. Butterworth-Heinemann, United States of America, 3rd edition, 2011.

[87] L. Ponson. Depinning Transition in the Failure of Inhomogeneous Brittle Materials. *Physical Review Letters*, 103(5):1–4, 2009.

[88] V. Privman, P. C. Hohenberg, and A. Aharony. *Phase Transitions and Critical Phenomena*. Academic Press, London–San Diego, 1991.

[89] D. C. Ralph and M. D. Stiles. Spin transfer torques. *Journal of Magnetism and Magnetic Materials*, 320(7):1190–1216, 2008.

[90] J. Ramasco, J. M. López, and M. A. Rodríguez. Generic dynamic scaling in kinetic roughening. *Physical Review Letters*, 84(10):2199–2202, 2000.

[91] A. Rosso, A. Hartmann, and W. Krauth. Depinning of elastic manifolds. *Physical Review E*, 67(2):021602, 2003.

[92] A. Rosso and W. Krauth. Origin of the Roughness Exponent in Elastic Strings at the Depinning Threshold. *Physical Review Letters*, 87(18):187002, 2001.

[93] L. Roters, A. Hucht, S. Lübeck, U. Nowak, and K. D. Usadel. Depinning transition and thermal fluctuations in the random-field Ising model. *Physical review. E, Statistical physics, plasmas, fluids, and related interdisciplinary topics*, 60(5 Pt A):5202–7, 1999.

[94] L. Roters, S. Lübeck, and K. D. Usadel. Corrected Article: Depinning transition of a driven interface in the random-field Ising model around the upper critical dimension. *Physical Review E - Statistical Physics, Plasmas, Fluids, and Related Interdisciplinary Topics*, 66(6):7, 2002.

[95] L. Roters and K. D. Usadel. Dimensional crossover and driven interfaces in disordered ferromagnets. *Physical Review E*, 65(2):027101, 2002.

[96] J. Ryu, S. B. Choe, and H. W. Lee. Magnetic domain-wall motion in a nanowire: Depinning and creep. *Physical Review B - Condensed Matter and Materials Physics*, 84(7):1–12, 2011.

[97] D. Sander, S. O. Valenzuela, D. Makarov, C. H. Marrows, E. E. Fullerton, P. Fischer, J. McCord, P. Vavassori, S. Mangin, P. Pirro, B. Hillebrands, A. D. Kent, T. Jungwirth, O. Gutfleisch, C .G. Kim, and A. Berger. The 2017 Magnetism Roadmap. *Journal of Physics D: Applied Physics*, 50(36):363001–33, 2017.

[98] N. L. Schryer and L. R. Walker. The motion of 180 domain walls in uniform dc magnetic fields. *Journal of Applied Physics*, 45(12):5406–5421, 1974.

[99] J. C. Slonczewski. Current-driven excitation of magnetic multilayers. *Journal of Magnetism and Magnetic Materials*, 159(1-2):L1–L7, 1996.

[100] E. H. Stanley. *Introduction to Phase Transitions and Critical Phenomena*. Oxford University Press, Oxford, 1971.

[101] E. C. Stoner. Collective Electron Ferromagnetism. II. Energy and Specific Heat. *Proceedings of the Royal Society A: Mathematical, Physical and Engineering Sciences*, 169(938):339–371, 1939.

[102] M. Sturma, C. Bellegarde, J. C. Toussaint, and D. Gusakova. Simultaneous resolution of the micromagnetic and spin transport equations applied to current-induced domain wall dynamics. *Physical Review B*, 94(10):1–9, 2016.

[103] A. Thiaville, Y. Nakatani, J. Miltat, and Y Suzuki. Micromagnetic understanding of current-driven domain wall motion in patterned nanowires. *Europhysics Letters*, 69(March):990–996, 2005.

[104] J. Torrejon and M. Hayashi. Spin Hall torque–driven chiral domain walls in magnetic heterostructures. In M. Vazquez, editor, *Magnetic Nano- and Microwires*, pages 313–331. Elsevier., 2015.

[105] M. Toyoda, H. Akai, K. Sato, and H. Katayama-Yoshida. Curie temperature of GaMnN and GaMnAs from LDA-SIC electronic structure calculations. *Physica Status Solidi (C) Current Topics in Solid State Physics*, 3(12):4155–4159, 2006.

[106] M. Tsoi, R. E. Fontana, and S. S P Parkin. Magnetic domain wall motion triggered by an electric current. *Applied Physics Letters*, 83(13):2617–2619, 2003.

[107] T. Tybell, P. Paruch, T. Giamarchi, and J.-M. Triscone. Domain Wall Creep in Epitaxial Ferroelectric Pb(Zr0.2Ti0.8)O3 Thin Films. *Physical Review Letters*, 89(9):097601, 2002.

[108] J.H. Van Vleck. Note on the Interactions between the Spins of Magnetic Ions or Nuclei in Metals. *Reviews of Modern Physics*, 34(4):681–686, 1951.

[109] M. Vanatka, J. C. Rojas-Sánchez, J. Vogel, M. Bonfim, M. Belmeguenai, Y. Roussigné, A. Stashkevich, A. Thiaville, and S. Pizzini. Velocity asymmetry of Dzyaloshinskii domain walls in the creep and flow regimes. *Journal of Physics Condensed Matter*, 27(32), 2015.

[110] M. Wang, R. P. Campion, A. W. Rushforth, K. W. Edmonds, C. T. Foxon, and B. L. Gallagher. Achieving high Curie temperature in (Ga,Mn)As. *Applied Physics Letters*, 93(13):11–14, 2008.

[111] P. Weiss. L ' hypothèse du champ moléculaire et la propriété ferromagnétique. *Journal de Physique Théorique*, 6(1):661–690, 1907.

[112] M Yamanouchi, J. Leda, F. Matsukura, S. E. Barnes, S. Maekawa, and H. Ohno. Universality Classes for Domain Wall. *Science*, 317:1726–1729, 2007.

[113] K. Yosida. Magnetic Properties of Cu-Mn Alloys. *Physical Review*, 106(5):893–898, 1957.

[114] C. Zener. Interaction Between the d Shells in the Transition Metals. *Physical Review*, 81(4):440–444, 1951.

[115] S. Zhang and Z. Li. Roles of nonequilibrium conduction electrons on the magnetization dynamics of ferromagnets. *Physical Review Letters*, 93(12):1–4, 2004.

université PARIS-SACLAY | ÉCOLE DOCTORALE Ondes et Matière (EDOM)

Titre : Comportements universels des parois de domaines magnétiques dans les ferromagnétiques minces.

Mots clés : Dynamique des parois magnétiques, régime de reptation, spintronique

Résumé : Comprendre la dynamique des parois magnétiques est essentiel pour le développement de technologies comme les mémoires magnétiques à haut densité. D'un point de vue fondamental, les parois de domaines peuvent être décrites comme des interfaces élastiques qui se déplacent dans un faible désordre d'ancrage. Leur dynamique, dite de reptation, présente des comportements universels qui sont caractérisés par des exposants critiques dépendant notamment de la dimensionnalité. Plus généralement, les comportements universels sont observés dans différents phénomènes aussi diverses que la propagation des fractures en solides, des fronts de combustion, des parois de domaines ferroélectriques...

La première partie de la thèse propose une analyse des comportements universels de la transition de dépiegage de parois de domaines sous champ magnétique. La dynamique de paroi a été étudiée sur une large gamme de températures, dans une couche ferromagnétique ultramince de Pt/Co/Pt. Nous avons comparé nos résultats avec ceux obtenus pour d'autres matériaux. Nous avons pu mettre en évidence la fonction universelle de la transition de dépiégeage qui rend compte des effets de champ magnétiques et des effets thermiques.

La deuxième partie présente une étude des effets de taille finie sur les régimes de reptation. Nous avons mesuré les exposants critiques pour des couches de (Ga,Mn)(As,P) de différentes épaisseurs. Nous avons pu observer une discontinuité des exposants dits de rugosité et de reptation. Cette discontinuité est la signature d'un changement criticité de la dynamique qui est associé à une transition de dimensionnalité. Au-dessous d'un champ critique dépendant de l'épaisseur de la couche et de la température, une paroi se comporte comme une ligne élastique (d = 1) se déplaçant dans un milieu 2D. Au-dessus du champ critique, le mouvement de paroi correspond à celui d'une surface (d = 2) dans un milieu 3D.

Dans la dernière partie, nous analysons la criticité du mouvement de paroi déplacé par courant électrique dans une couche mince de (Ga,Mn)(As,P). Nous étudions comment varie la dynamique de paroi avec l'angle entre la direction du courant et la normale à la paroi. Pour un courant perpendiculaire à la paroi, les exposants critiques de rugosité et de reptation mesurés sont similaires à ceux obtenus sous champ magnétique. Cela indique une compatibilité avec la classe d'universalité dite quenched Edward-Wilkinson. Pour un angle non-nul, la croissance de facettes révèle une compatibilité avec la classe d'universalité quenched Kardar-Parisi-Zhang négative.

Title : Universal behaviors of magnetic domain walls in thin ferromagnets.

Keywords : Magnetic domian wall dynamics, creep regime, spintronics

Abstract : Understanding magnetic domain walls dynamics (DW) is crucial in order to develop technological applications like high density memories in ferromagnets. From the fundamental point of view domain walls are described as interfaces moving in a weak pinning potential. Below the depinning threshold, DWs move in what it is known as the creep regime, which exhibit universal behaviors characterized by critical exponents who depend, among other things on the dimensionality and geometry of the interface. More generally, these universal behaviors are shared by different physical systems as diverse as propagation of fractures in solids, combustion fronts, ferroelectric domain walls...

In the first part of the thesis, we address the universal behavior of the depinning transition in domain walls driven by magnetic field. For this purpose we measure the DW velocity as a function of magnetic field in an ultrathin Pt/Co/Pt film and then compare our results with other materials. We reveal a universal scaling function and obtain a consistent description for both the depinning transition and the thermally activated creep regime.

In the second part of the manuscript, we study the sample size effects on the critical exponents within the creep regime. We use ferromagnetic (Ga, Mn)(As,P) films of different thicknesses. We observe a discontinuity in the roughness ζ and the creep μ exponents. This discontinuity evidences a dimensional crossover and a change in criticality in the quenched Edward-Wilkinson model. Below a certain critical field H_c, the DW behaves as an elastic line ($d = 1$) moving in a $2D$ medium. Above H_c the DW motion corresponds to an elastic interface ($d = 2$) moving in a $3D$ medium.

In the last part, we compare the thermally activated creep dynamics in domain walls driven by magnetic field and by electric current separately in a (Ga,Mn)(As,P) thin film. We study the DW dynamical response with the angle between the current and the normal to the DW. When the angle between the current and the normal to the DW is sufficiently small, the critical exponents measured for current induced DW motion are very similar than for field induced DW motion. This result indicates agreement with the quenched Edward-Wilkinson universality class. When the angle between the DW and the current is not negligible, the DW faceting reveals compatibility with the quenched negative Kardar-Parisi-Zhang universality class.

Université Paris-Saclay
Espace Technologique / Immeuble Discovery
Route de l'Orme aux Merisiers RD 128 / 91190 Saint-Aubin, France